Maria João Marques de Carvalho

Structural and biochemical characterization of the interaction of calmodulin with the EAG1 potassium channel cytoplasmic regions

Tese de Candidatura ao grau de Doutor em Ciências Biomédicas submetida ao Instituto de Ciências Biomédicas Abel Salazar da Universidade do Porto

Orientador – Doutor João Morais Cabral

Categoria – Investigador Principal

Afiliação – Instituto de Biologia Molecular e Celular

Co-orientador – Professor Doutor Pedro Moradas Ferreira

Categoria – Professor Catedrático

Afiliação – Instituto de Ciências Biomédicas Abel Salazar da Universidade do Porto

Para a avó Zé.

Fazes-me falta.

The present work was financially supported by Fundação para a Ciência e Tecnologia and co-financed by the European Social Fund through the research grant PTDC/BBB-BQB/1418/2012.

ACKNOWLEDGEMENTS

First and foremost I need to thank my supervisor João Morais Cabral. I am thankful for his guidance and trust, and for providing me all kinds of support throughout these years. From financial support through tuitions and half a dozen of grants; emotional support through the ups and downs of the project; physical support by giving me a hand when my back was numb from all the crystallization trials and for all the training he provided, both himself and by allowing me to attend workshops and international meetings, I am in debt. I also want to thank my co-supervisor Prof. Pedro Moradas Ferreira for agreeing to take this position.

Carol was instrumental for my training from the beginning. I really enjoyed our chats, scientific or otherwise. I am grateful to her for keeping the lab on track and for all the freebies. I will leave the Cabral lab with very fond memoriesof the past six years.

I am grateful for my girfriends Fátima, Rita and Andreia for all the leisure moments and for being such good lab partners. Rita's motivation and commitment to work and her friends are an inspiration. I admire Fátima for her strong character and ability to calm me down when necessary. I really treasure the time we spend together outside the lab. I thank Andreia for the friendship and for help with the project.

Thank you Pires, for useful (as well as silly) discussions, for collaborating in my project, for Photoshop and building sturdy shelves. I thank Andras for great scientific input and for time-saving Excel spreadsheets. I really appreciated JP's willingness for leisure activities as I am also always eager for a good time. I thank Artur and Celso for providing a fun working environment and lending a hand when needed.

I am grateful to my friends for the much needed nights out and vacations. I need to acknowledge my dear friend Adaixo, who had a big role on my interest in structural biology and coming to the Cabral lab. You have influenced me more than you imagine and I am grateful for having had the chance to work and learn from you.

I cannot leave out our collaborators that have enriched this project with their results and scientific input: Roland Schonherr, Nirakar Sahoo, Guillaume Gabant, Martine Cadene, Frederick Muskett and Eva Muñoz.

The unconditional love and encouragement from my family were fundamental in this process. I need to thank my mom and dad, who put so much effort in making sure I was as informed as possible in all things, but mostly in what concerned my education and career. Also my sister, Vitor and Fernanda for back support. Thank you for putting up with

the crazy schedules and the occasional bad mood. To my grandmother, to whom I dedicate this thesis, I wish you were here to witness your oldest granddaughter's graduation.

Sérgio, my better-half, thank you for providing me love and laughs galore. But most importantly, for being so rational, so different from me, for helping me relativize things at times of despair. You incentivize me to be a better person and I feel so lucky to have had you in my life for the past 8 years.

ABSTRACT

The KCNH potassium channel family includes EAG, ERG and ELK channels. These channels are voltage-gated and are involved in important physiological roles such as cardiac repolarization, neuronal excitability, tumor proliferation and hormone secretion. KCNH channels have large N- and C-terminal cytoplasmic domains that include a PAS domain at the N-terminus and a cyclic nucleotide binding-homology domain (CNB-homology domain) at the C-terminus. It has been well established that the PAS domain interacts with CNB-homology domain and that this interaction is important for the channel's gating properties.

Calcium inhibits EAG1 currents, an effect that is mediated by calmodulin binding to the channel. Three calmodulin binding sequences have been identified: BDN, after the PAS domain; BDC1 and BDC2, after the CNB-homology domain. Channels with disrupting mutations at BDN, BDC1 and BDC2 are nearly insensitive to Ca^{2+}-calmodulin, supporting the functional importance of all three sequences for Ca^{2+}-calmodulin regulation. However, the physiological relevance of the BDC1 has been questioned by several studies. In accordance, our structure of the isolated CNB-homology domain and another lab's structure of the PAS/CNB-homology domain complex reveal that BDC1 is partially occluded due to the self-liganded conformation of the domain. Through mutations as well as through the use of the ligand calmodulin we have provided evidence that an unliganded state exists.

Using calorimetry and X-ray crystallography we have dissected the calmodulin binding properties of all three calmodulin binding sites which revealed very distinct binding modes. We propose that BDC1 is not directly involved in CaM binding but might have a role through the interaction with the PAS domain. Also, based on structural, biochemical and functional data we have redefined the limits of the CaM BDC2 as being extended towards the N terminus.

SUMÁRIO

A família de canais de potássio KCNH inclui os canais EAG, ERG e ELK. Estes canais são regulados por voltagem e estão envolvidos em importantes processos fisiológicos como a repolarização cardíaca, excitabilidade neuronal, proliferação tumoral e secreção de hormonas. Os canais da família KCNH têm zonas citoplasmáticas extensas que incluem um domínio PAS no N-terminal e um homólogo a domínios que ligam nucleotideos cíclicos (CNBhD) no C-terminal. É sabido que o domínio PAS interage com o CNBhD e que esta interacção é importante para as propriedades de activação do canal.

O cálcio inibe as correntes dos canais EAG1, um efeito mediado pela ligação da calmodulina ao canal. Foram identificadas três sequencias de ligação à calmodulina: BDN, depois do domínio PAS; BDC1 e BDC2 depois do CNBhD. Canais com mutações em qualquer uma destas sequências são praticamente insensíveis a Ca^{2+}-calmodulina, indicando que as três sequências são importantes para a regulação por Ca^{2+}-calmodulin. No entanto, a relevância fisiológica do BDC1 foi questionada por vários estudos. De acordo, a nossa estrutura de um CNBhD e a estrutura do complexo entre o domínio PAS e CNBhD resolvida por outro laboratório revelaram que o BDC1 está parcialmente obstruído devido à conformação “auto-ligada” do domínio. Através de mutações e do uso do ligando calmodulin mostramos evidencias da existência de um estado não ligado do CNBhD.

Utilizando calorimetria e cristalografia de raios-X, dissecamos as propriedades de ligação à calmodulina dos três locais de ligação que revelam modos de ligação à calmodulina distintos. Propomos que o BDC1 não está directamente envolvido na ligação à calmodulin mas poderá ter um papel regulatório através da interacção com o domínio PAS. Redefinimos os limites da sequencia de ligação à calmodulina BDC2, que se extende para o N-terminall, baseado em dados estruturais, bioquímicos e funcionais.

LIST OF PUBLICATIONS

The results described on Chapter III of this thesis are based on the publication:

Marques-Carvalho, M.J.; Sahoo, N.; Muskett, F.W.; Vieira-Pires, R.S.; Gabant, G; Cadene, M.; Schönherr, R.; Morais-Cabral, J.H.,. “Structural, biochemical, and functional characterization of the cyclic nucleotide binding homology domain from the mouse EAG1 potassium channel.” *Journal of Molecular Biology*, 423(1), pp.34–46, 2012.

A manuscript with the results presented on Chapter IV is currently being drafted to be submitted for publication.

CONTENTS

ABBREVIATIONS

BDC1 – C terminus calmodulin binding domain 1

BDC2 – C terminus calmodulin binding domain 2

BDN – N terminus calmodulin binding domain 2

CaM - calmodulin

cAMP – cyclic adenosine monophosphate

Ca_v – voltage-gated calcium channel

CCP4 - Collaborative Computational Project 4

CNB(-homology) domain – cyclic nucleotide binding(-homology) domain

CNG - cyclic nucleotide gated channel

Dansyl-Cl - 5-(dimethylamino) naphthalene-1-sulfonyl chloride

ΔH – enthalpy change

ΔS – entropy change

DTT - dithiothreitol

EAG – ether-a-go-go

EDTA - Ethylenediaminetetraacetic acid

EGTA - ethylene glycol bis(β-aminoethyl ether) N,N′-tetraacetic acid

ELK – EAG-like potassium channel

ERG - EAG-related gene

FRET – Förster Resonance Energy Transfer

FT – flow-through

HCN – Hyperpolarization-activated Cyclic Nucleotide-gated channel

HEPES - 4-(2-Hydroxyethyl)piperazine-1-ethanesulfonic acid

IMAC - immobilized metal affinity chromatography

IPTG - Isopropyl β-D-1-thiogalactopyranoside

ITC – isothermal titration calorimetry

KcsA - potassium crystallographically-sited activation channel

K_A – association constant

K_D – dissociation constant

K_v – voltage-gated potassium channel

LQTS – long QT syndrome

MAL-PEG – methoxypolyethylene glycol maleimide

MBP – maltose-binding protein

NMR – nuclear magnetic resonance

OD – optical density

PAS domain – Per-Arnt-Sim domain

PDB – Protein Data Bank

PEG - Polyethylene glycol

PMSF - phenylmethylsulfonyl fluoride

SDS-PAGE – sodium-dodecyl-sulphate polyacrylamide gel electrophoresis

TCEP - tris(2-carboxyethyl)phosphine

TEV – Tobbaco Etch Virus

TM – transmembrane helix

Tris-HCl - tris(hydroxymethyl)aminomethane hydrochloride

WT – wild-type

I. INTRODUCTION

Potassium channel architecture

In the 1950's, Hodgkin and Keynes performed the first studies on ion permeation across squid giant axon membranes (Hodgkin & Keynes 1955). They observed that K^+ flowed down its electrochemical gradient, that their movement was affected by other ions and that they interacted with each other when crossing the membrane. They suggested that ions should move in a single file and that there would be several ions passing through the membrane at the same time.

In the following decades, Armstrong and Hille demonstrated that K^+ and Na^+ cross cell membranes through protein pores - K^+ and Na^+ channels (MacKinnon 2004).

Advances in molecular biology allowed for the cloning and study of the Shaker K^+ channel from Drosophila melanogaster. Before high resolution structures of K^+ channel became available, many aspects of K^+ channel architecture had been inferred through the use of pore blockers and mutagenesis, including mapping of the pore, selectivity filter region and an activation gate (Aggarwal & MacKinnon 1996; Ranganathan et al. 1996; Hidalgo & MacKinnon 1995; Liu et al. 1997; Holmgren et al. 1997).

The typical potassium channel is an assembly of four subunits surrounding a central pore through which potassium ions flow down their electrochemical gradient. Each subunit can have two or six transmembrane helices as well as cytoplasmic domains with regulatory roles (MacKinnon 2003; MacKinnon 2004).

Potassium channels contain a highly conserved signature sequence (TTVGYG or TTVGFG) in the selectivity filter, a region that forms the coordinating shell for potassium ions in the channel. Potassium ions flow through the pore at rates of 10^7-10^8 per second, which is close to the rate of unrestricted diffusion of ions in water. The selectivity filter is responsible for the high selectivity of K^+ ion over the Na^+ ion by a factor of over 1000 (Doyle et al. 1998) and mutation of these residues disrupts the channel's ability to discriminate between K^+ and Na^+ ions (MacKinnon 2004; MacKinnon 2003; Kim et al. 2015).

The first high resolution structure of a potassium channel belonged to the *Streptomyces lividans* KcsA (Doyle et al. 1998). The structure confirmed many of the predictions that had been made and shed further light into the molecular basis of K^+ conduction and

permeation. KcsA is tetrameric, with 4-fold symmetry and has two transmembrane helices and one tilted pore helix (P-helix) per subunit, Figure 1. In the center of the membrane the ion conduction pathway is 10 Å wide, forming a water-filled cavity that harbors a hydrated K^+, Figure 1b (Doyle et al. 1998; Zhou et al. 2001). This ion is stabilized by keeping its hydration shell and by the dipole at the C terminus of the P-helix.

At the selectivity filter region, the narrowest part of the pore, there are four sites for K^+ binding, S1 to S4; each K^+ is coordinated by eight oxygen atoms, four above and four below, in a cage-like structure that mimics the water coordination of the ion in the central cavity, Figure 1. Importantly, it has been shown that K^+ adopts two alternating configurations, each with two ions (S1-S3 or S2-S4) in this filter, separated by a water molecule (Morais-Cabral et al. 2001); the crystal structure represents an average of these two configurations (Figure 1b).

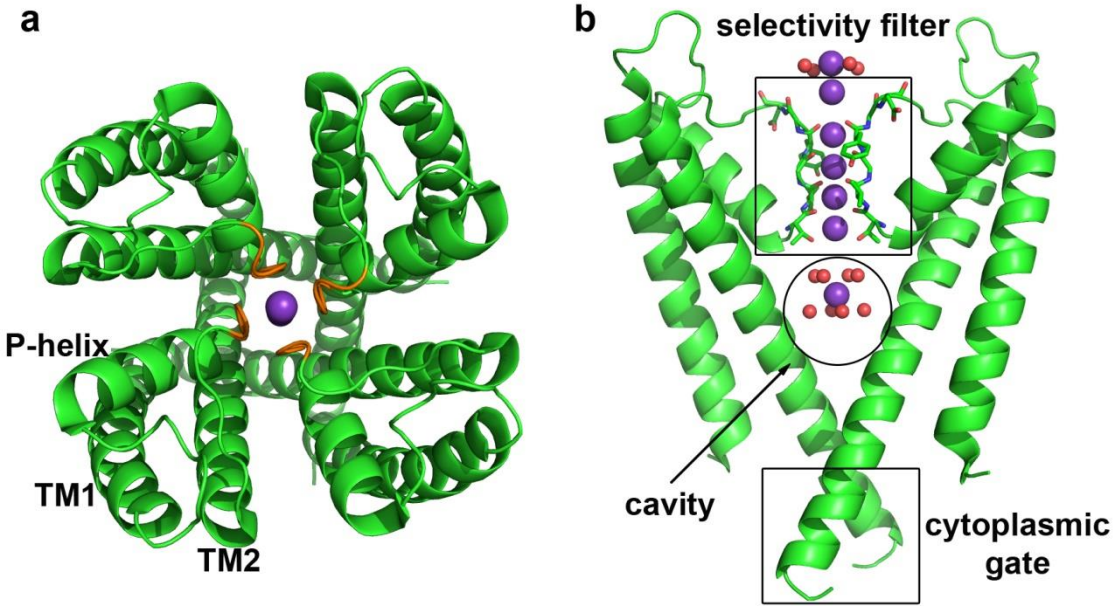

Figure 1 – Structure of the KcsA potassium channel (PDB code: 1K4C) (Zhou et al. 2001). a) Top view of the tetramer in cartoon representation, K^+ ions are depicted as purple spheres and selectivity filter in orange. b) Side view of two subunits of KcsA. K^+ ions are purple spheres, water molecules are red spheres and the selectivity filter is in stick representation.

Ion channels can contain several gates that constitute a barrier to the passage of ions, the most common of which is the cytoplasmic gate (Figure 1b). Gating is the process that allows channels to go from a non-active (closed) to an active (open) state in response to an external signal. This signal can be a ligand (ligand-gated channels), changes in the

transmembrane potential (voltage-gated channels), pressure (mechanosensitive channels) or temperature (temperature-gated channels).

Classification of potassium channels

Potassium channels can be grouped into four classes, taking into account the stimulus that they respond to, the conductance properties and their structural organization (Pardo & Stühmer 2014). Voltage-gated potassium channels (K_v1-12, in mammals) respond to changes in voltage and are tetrameric; they contain six transmembrane helices (TM), the first four of which compose the voltage-sensor domain and the last two the pore domain. Calcium-activated potassium channels (K_{Ca}) are also tetrameric with six transmembrane segments but are activated by calcium. There are also the inward-rectifier potassium channels (K_{ir}1-7) that contain two transmembrane helices corresponding to the pore forming domain and are regulated by multiple factors such as G-proteins, phospholipids, pH or ATP. Finally, the two-pore domain potassium channels (K2P1-18), also known as "leak" channels, are dimeric and composed of two pore-forming domains in tandem, resulting in a channel subunit with four transmembrane segments.

Voltage-gated channels

Structures of voltage-gated potassium channels show a pore region surrounded by four voltage sensor domains (Long et al. 2005), Figure 2. One particularity is that the fourth helix (TM4) adopts a long 3_{10} helical conformation; these helices are rare and less stable due to being packed more tightly (Vieira-Pires & Morais-Cabral 2010). TM4 contains 4-8 arginines, spaced by two residues and these arginines are called the "gating charges". Upon a change in membrane voltage, these gating charges move across the membrane through the translation and rotation of the TM4 helix (Tombola et al. 2006; Li et al. 2014). During this process, the arginines change electrostatic partners with countercharges from TM1 and TM3 (Li et al. 2014). The conformational change is coupled to the cytoplasmic gate of the channel which is present on the cytoplasmic end of the pore domain (Figure 1b), shifting the equilibrium from closed to open channels (Tombola et al. 2006).

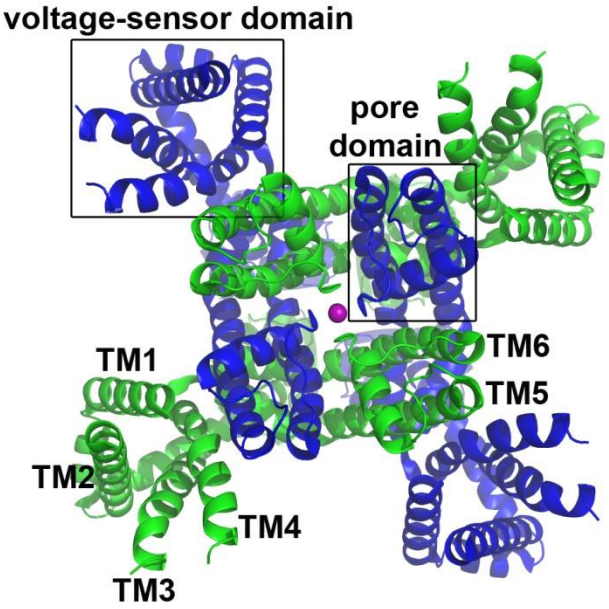

Figure 2 - Structure of the mammalian voltage-gated potassium channel Kv1.2 (PDB code: 2A79). Top view of the tetramer in cartoon representation, channel subunits are depicted in alternate colors for clarity purposes. K^+ ions are depicted as purple spheres.

KCNH potassium channel family

The KCNH K^+ channel family (or EAG K^+ channel family) includes EAG (ether-a-go-go), ERG (eag-related gene) and ELK (eag-like) K^+ channels (Warmke & Ganetzky 1994). The eag gene was first identified through a mutant *Drosophila melanogaster* that displayed a leg shaking phenotype when under ether anesthesia, hence the name (Warmke et al. 1991). Using homology screens of cDNA libraries, three related gene subfamilies have been found - eag, elk and eag – and eight genes have been identified in mammals that belong to the KCNH family – eag1-2, elk1-3 and erg1-3 (Bauer & Schwarz 2001). Sequence alignments show that members of the EAG family are closely related to cyclic nucleotide-gated cation channels as well as voltage-gated K^+ channels (Warmke & Ganetzky 1994).

KCNH channels are voltage-gated potassium channels that are involved in important physiological processes such as cardiac repolarization (Tristani-Firouzi & Sanguinetti 2006), neuronal excitability (Becchetti et al. 2002) and cellular proliferation (Pardo & Sühmer 2008). They are composed of four subunits of six transmembrane helices surrounding a central pore as well as characteristic large cytoplasmic regions (Figure 3) that have a role in channel regulation, serving as interfaces for external cues such as phosphorylation (Wang et al. 2002), interaction with kinases (Sun et al. 2004), integrins (Cherubini et al. 2005) and calmodulin (Schönherr et al. 2000).

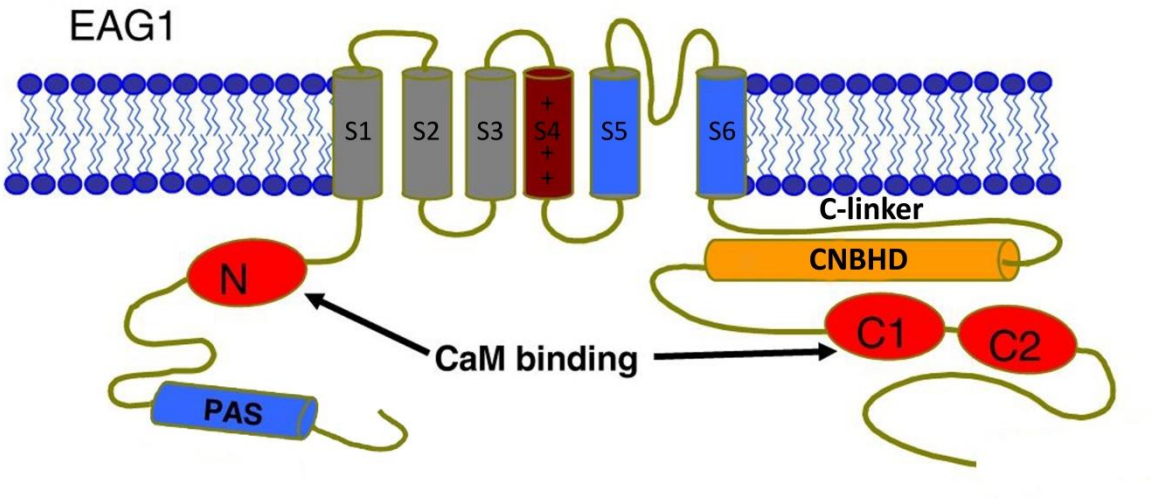

Figure 3 - Schematic representation of an EAG1 channel subunit. From the N to C terminus it is composed by a PAS domain, calmodulin binding site BDN, transmembrane helices S1-S6, C-linker helices that connect S6 to the CNB-homology domain, followed by calmodulin binding sites BDC1 and BDC2. Adapted from S.H.Heinemann.

KCNH channels have been associated with several pathologies: epilepsy, schizophrenia, cancer and long QT syndrome (LQTS). The human ERG1 (hERG) channel has been extensively studied; it is expressed in the heart and is responsible for the last phase of the repolarization ventricular action potential (Tristani-Firouzi & Sanguinetti 2006). This channel is linked to LQTS, a condition characterized by arrhythmia, seizures and sudden death which results from disruptions of normal channel function due to either inheritable hERG channel mutations or block of the channel by pharmaceutical drugs (Tristani-Firouzi & Sanguinetti 2006). The severity of LQTS is the reason behind the routine testing of pharmaceutical compounds on hERG channel activity early in the drug-development process. In contrast, human EAG1 (hEAG1) channel expression occurs exclusively in the central nervous system, more specifically in the presynaptic terminals. hEAG1 channels have been suggested to regulate action potentials during high-frequency stimulus, modulating synaptic strength by acting as an intermediate between fast high-voltage activated channels and slow low-voltage activated channels (Mortensen et al. 2015). Whereas hEAG1 expression in healthy individuals is mostly confined to the brain, it is overexpressed in more than 70% of cancers (Urrego et al. 2014) which makes it a good tumour biomarker and a potential target for cancer treatments. Overexpression of hERG1 has also been associated with several types of cancer (Crociani et al. 2003; Urrego et al. 2014).

KCNH cytoplasmic domains

KCNH channel cytoplasmic regions include two globular domains, a PAS domain at the N terminus and a domain with homology to cyclic nucleotide binding domains (CNB-homology domain) on the C terminus (Figure 3), although these channels do not respond to cyclic nucleotides.

EAG1 channels, in particular, also include several calmodulin binding sites, located after the PAS domain and the CNB-homology domain (Figure 3) and are inhibited by calmodulin (Schönherr et al. 2000; Ziechner et al. 2006).

PAS domain

PAS (*Per-Arnt-Sim*) domains can be found in all kingdoms of life. Although their primary sequences vary, the PAS domain fold is conserved. It usually functions as a regulatory domain, either by binding small molecules such as FAD or heme, or mediating protein-protein interactions (Henry & Crosson 2011).

KCNH channels have a PAS domain on the N terminus which is considered an orphan receptor, given that so far no ligand has been identified. The first solved structure of an eukaryotic PAS domain belonged to the hERG channel (Morais Cabral et al. 1998). It is composed of a β-sheet with five strands (βA-βE) tightly packed against a set of helices - a highly flexible N-terminal CAP region, αA-αC and a short 3_{10} helix (Figure 4a). Structures of PAS domains from the other KCNH subfamilies (EAG and ELK) have also been solved by X-ray crystallography and are very similar to each other (Adaixo et al. 2013). They share a conserved hydrophobic patch in the β-sheet and small cavities where other PAS domains bind small molecules (Adaixo et al. 2013). Solution structures of hERG PAS domains have revealed that the CAP region has high structural variability (Figure 4b) (Ng et al. 2011; Li et al. 2010; Muskett et al. 2011).

It is known that the KCNH PAS domains have a role in channel function through the interaction with other parts of the channel. Truncation of hERG1 PAS domain, for example, speeds up the channel's characteristic slow deactivation. These changes can be reversed if purified soluble PAS domain is added to the cell expressing the truncated channel (Morais Cabral et al. 1998). Furthermore, in EAG channels, gating changes caused by deletion of the N-terminal CAP could be reverted by mutations on the S4-S5 linker (Terlau et al. 1997), suggesting that there is an interaction of the CAP region with the gating machinery in KCNH channels.

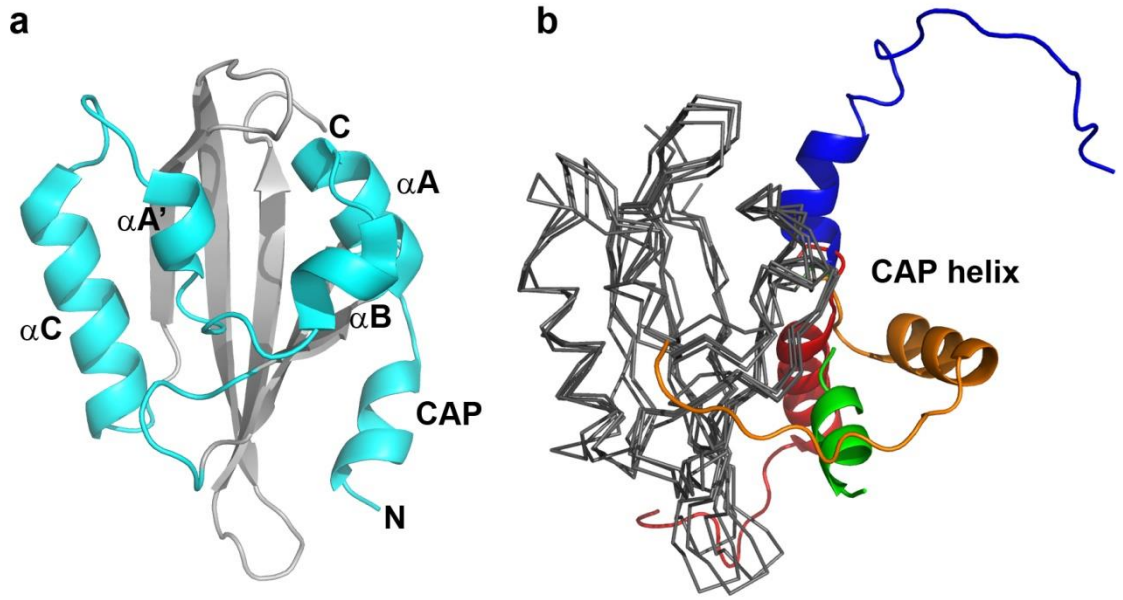

Figure 4 – KCNH PAS domains. a) Structure of the mEAG1 PAS domain in cartoon representation. b) Structural variability of the PAS CAP region (cartoon). Superposition of four NMR and X-ray PAS domain structures (in grey ribbon) from the hERG1 channel: PDB codes 4HP9 (green), 2L1M (red), 2L0W (orange), 2L4R (blue).

Cyclic nucleotide binding(-homology) domain

Cyclic nucleotide binding domains (CNB domains, Figure 5) are involved in signaling pathways, both in eukaryotes and prokaryotes. Cyclic nucleotide binding induces a conformational change that is propagated to the effector domain - a nucleotide exchange factor, a transcription factor, a kinase or an ion channel. CNB domain structure is composed by an antiparallel β-roll preceded by α-helix αA and followed by helices αB and αC (Figure 5). An additional short α-helix, P-helix that is located between β-strands 6 and 7 is part of the “phosphate binding cassette” that coordinates the cyclic phosphate (Rehmann et al. 2007). In cyclic-nucleotide regulated channels extra helices (C-linker) connect the channel pore to the CNB domain and are responsible for the transmission of the conformational change to the pore. The main difference between bound and unbound states is the overall rearrangement of the helices (Figure 5). Upon binding of the ligand, the phosphate binding cassette and helix αC collapse around the ligand. In the unbound state helix αC can occupy multiple positions (Clayton et al. 2004; Altieri et al. 2008; Rehmann et al. 2007). Particularly important for ion channels is the repositioning of the C-linker that is thought to lead to changes in the gate (Craven & Zagotta 2006).

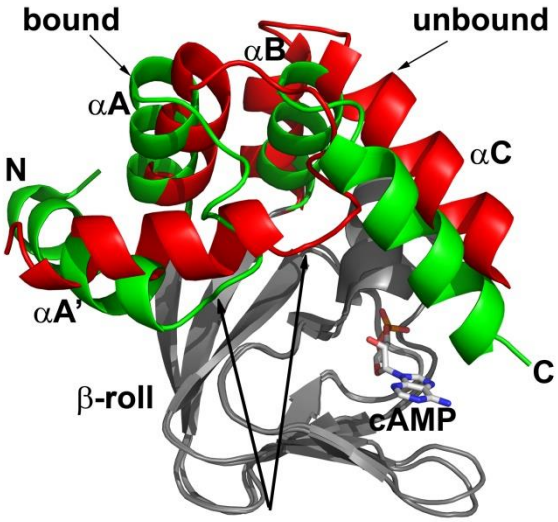

Figure 5 - Superposition through β-roll of bound and unbound CNB domains from MlotiK1 channel. In green is the bound structure (PDB code 1VP6) with cAMP in stick model and in red the unbound structure (PDB code 1U12). β-roll is in grey. Large arrows point to two positions of loop between αA'-αA.

The CNB-homology domain in KCNH channels has strong homology to CNB domains of Cyclic Nucleotide Gated (CNG) channels and Hyperpolarization-activated Cyclic Nucleotide-gated (HCN) channels. KCNH channels also show homology to CNG and HCN channels in the C-linker region that connects the CNB-homology domain to the pore (Warmke & Ganetzky 1994). However, it has been shown that the *in vitro* affinity of CNB-homology domain for cyclic nucleotides is very low ($K_D \geq 50$ μM) and that the function of KCNH channels is not altered upon exposure to cyclic nucleotides (Brelidze et al. 2009).

We have determined the structure of the CNB-homology domain from the mouse EAG1 (mEAG1) channel at 2.2 Å (PDB code 4F8A) (Marques-Carvalho & Morais-Cabral 2012); it shows the typical fold of a CNB domain, with 3 helices (αA, αB and αC) lying on the surface of a β-roll (Figure 6) (Marques-Carvalho et al. 2012). Residues immediately after the αC helix (residues 696 to 707), which we designate as the C-terminal tail of the domain, adopt an extended conformation and snake over the surface of the structure. The structure also includes part of the C-linker (helices αD´, αE´ and αF´) that connects the domain to the last transmembrane helix of the channel.

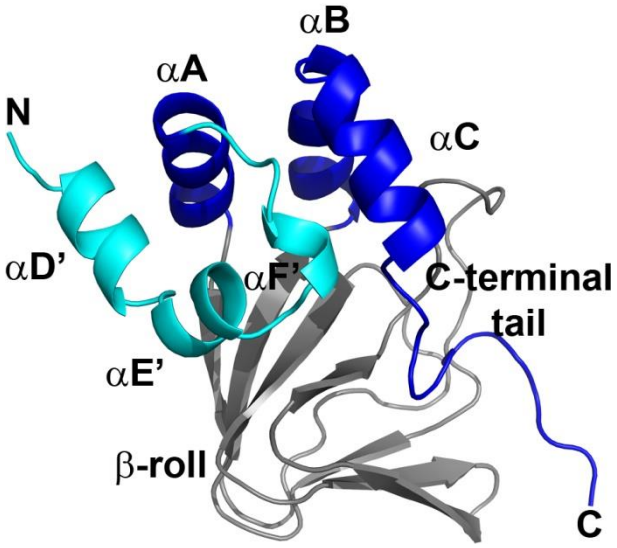

Figure 6 - Structure of the CNB-homology domain from mouse EAG1 channel. Cartoon representation with the C-linker stretch depicted in cyan, CNB-homology domain helices in dark blue and β-roll in grey.

Structures for CNB-homology domains of all three KCNH subfamilies (mouse EAG1 (mEAG1) PDB code 4F8A, zebrafish ELK (zELK) PDB code 3UKN and mosquito ERG (agERG) PDB code 4L11) have been solved and share many similarities. Superposition through the β-roll shows that the CNB-homology domain helices are differently positioned on the surface of the β-roll but maintain the same relative disposition (Figure 7a) (Marques-Carvalho et al. 2012; Brelidze et al. 2012; Brelidze et al. 2013). In contrast, the C-linker region in these structures displays a large structural variability (Figure 7b) and it is not clear if any of the observed conformations are functionally meaningful.

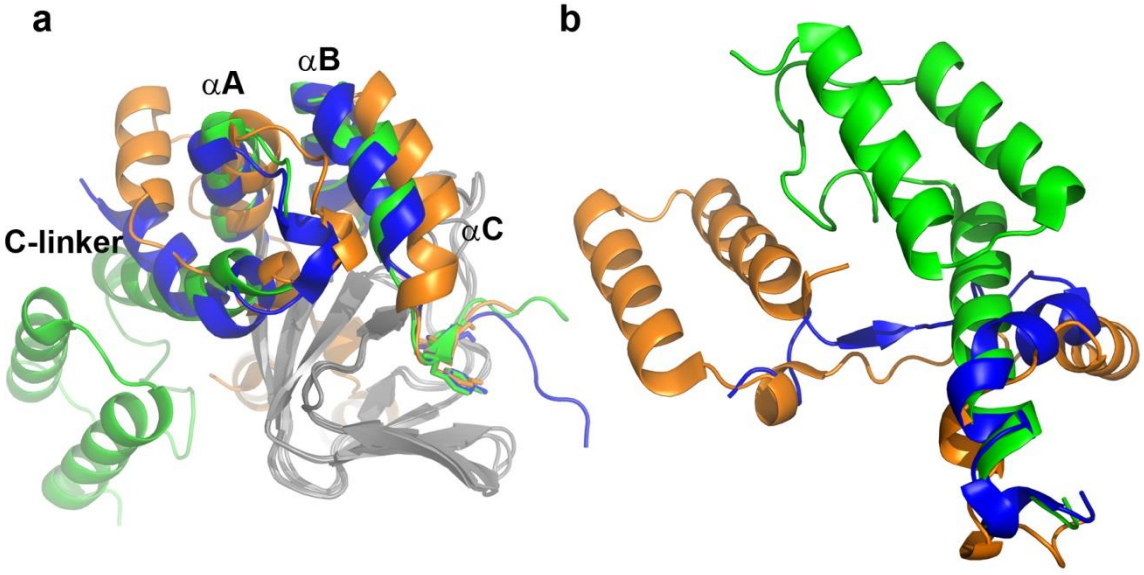

Figure 7 – a) Superpositions of CNB-homology domains from mEAG1 (blue, PDB code 4F8A), zELK CNB-homology domain (orange, PDB code 3UKN) and agERG (green, PDB code 4L11) through the β-roll. b) Different dispositions of the C-linker region, coloring scheme is maintained.

To better understand the structural underpinnings of the low affinity of cyclic nucleotides for the CNB-homology domain we compared the structures of CNB-homology domain and CNB domains. Like in CNB domains, there is a shallow “binding pocket” in CNB-homology domains (Figure 8a, 8b). This pocket is more open than the CNB domain binding pockets. There is also an interesting aspect in the conservation of residues of the pocket. Many of the residues that surround the base of the nucleotide in the MlotiK1 CNB domain (Figure 8b), and which are fairly conserved across CNB domains, are basically unchanged in the CNB-homology domain (Figure 8a). In contrast, the key arginine that interacts with the phosphate group in CNB domains and determines much of the affinity for the ligand (Altieri et al. 2008) is not present in the homology domains.

Overall, the differences in the structure and amino acid composition of the pocket of CNB-homology domains relative to CNB domains explain the very low affinity of the homology domains for cyclic nucleotides.

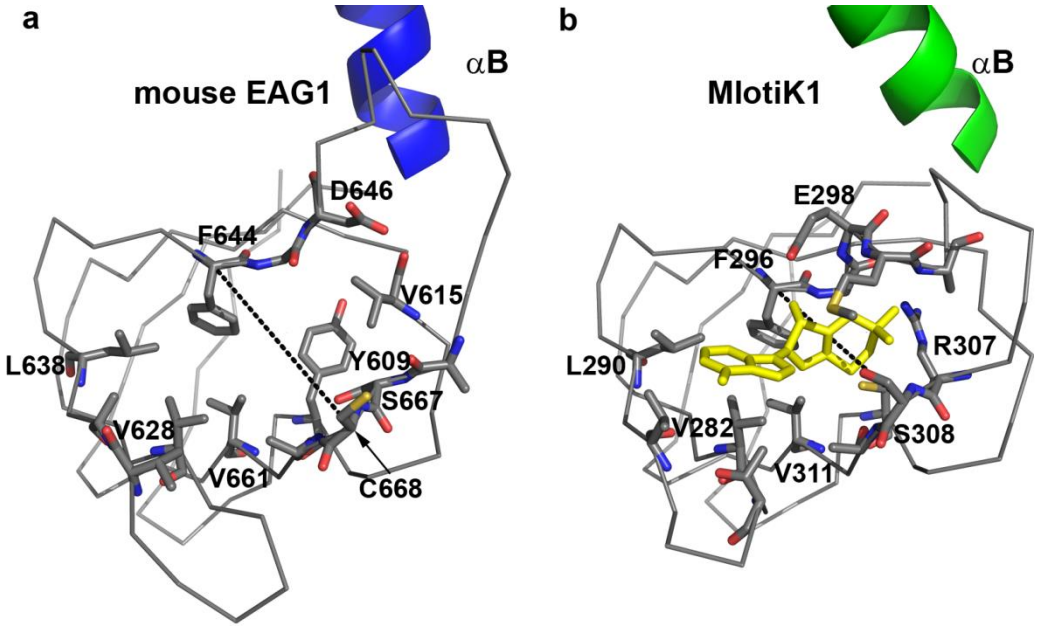

Figure 8 - Comparing binding pockets. a) Close up view of binding pocket in CNB-homology domain. b) Close up view of cAMP binding pocket in CNB domain from MlotiK1; cAMP in yellow stick. PDB code: 1VP6. Some of the residues that line the cAMP binding pocket in MlotiK1, and corresponding residues in CNB-homology domain, are shown in stick and are labeled. Dotted lines indicate distances measured across the pockets, between equivalent residues: 10.6 Å for MlotiK1 domain and 12.5 Å for mEAG1 domain.

Importantly, the pocket is not empty in the CNB-homology domain structures. All the structures adopt the same “self-liganded” conformation: two residues in the C-terminal tail which are conserved across KCNH channels (Y699 and L701 in the mEAG1 channel; Y740 and L742 in zELK and Y727 and M729 in agERG) occupy the volume taken up by cAMP in the CNB domains of the HCN and MlotiK1 channels (Figure 9a and 9b). These residues are therefore known as the “instrinsic ligand”. The intrinsic ligand residues establish an extensive network of interactions with residues in the pocket (Figures 9b) and some of these interactions are similar to the ones established by cyclic nucleotides in CNB domains. In mEAG1, the aromatic ring of the tyrosine is roughly at the same position as the aromatic base of the cyclic nucleotide and interacts with some of the residues conserved across CNB domains and CNB-homology domain; the leucine side-chain overlaps with the cyclic phosphate group and interacts with Y609 and V615 that take up the position of the arginine conserved in CNB domains (Figure 8a). In occupy the volume of the nucleotide base and cyclic phosphate, respectively (Brelidze et al. 2012; Brelidze et al. 2013).

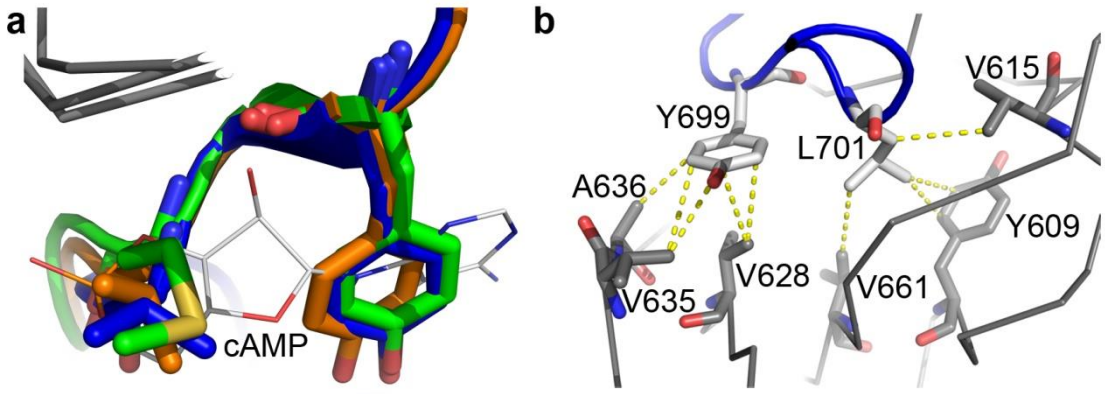

Figure 9 – a) Close up view (viewed from binding pocket) of intrinsic-ligand residues in CNB-homology domain from mEAG1 (blue), zELK (orange) and agERG (green) superimposed with cAMP molecule (in lines) from MlotiK1 CNB DOMAIN (PDB code: 1VP6). Superposition of structures was done through residues in β-roll. b) Residues of CNB-homology domain binding pocket interacting with Y699 and L701 (in white). Residues were selected with a 4 Å radius. View is rotated 180° relative to c).

The presence of the same self-liganded conformation in the three different crystal structures, determined from domain constructs with very different limits (the mEAG1 domain includes only part of the C-linker while the domain from zELK and agERG have

the whole linker) and originating from different KCNH channel sub-families (with just ~40% identity over the domain sequence), supports the proposal that this conformation is a significant feature of KCNH channels. However, mutations in the intrinsic ligand residues have very different effects on the channel's gating properties, depending on the subfamily (Brelidze et al. 2012; Marques-Carvalho et al. 2012; Brelidze et al. 2013).

PAS/CNB-homology domain complex

Several studies have shown that PAS and CNB-homology domains interact with each other. An in-cell fluorescence study in hERG1 channels showed that the PAS domain only alters gating in channels that contain a CNB-homology domain. Moreover, PAS only interacts with a truncated channel if the CNB-homology domain is present. The study also showed that the PAS/CNB-homology domain interactions occur across different channel subunits (Gianulis et al. 2013). In addition, it was shown that PAS domain and CNB-homology domain from mEAG1 interact with a K_D of 13 μM (Haitin et al. 2013a). The structure of this complex (Figure 9) reveals an extensive binding interface that includes interactions between: the CNB-homology domain intrinsic ligand and helix αB from the PAS domain; PAS domain strands βA and βB and the post-CNB-homology domain region (that comprises the calmodulin binding sequence BDC1); and the PAS-CAP helix with the β-roll from the CNB-homology domain (Figure 10). Many mutations associated with diseases (LQTS or cancer) lie on this interface, suggesting that perturbation of the interaction between PAS domain and CNB-homology domain is related to the pathophysiology of KCNH-related diseases (Haitin et al. 2013b).

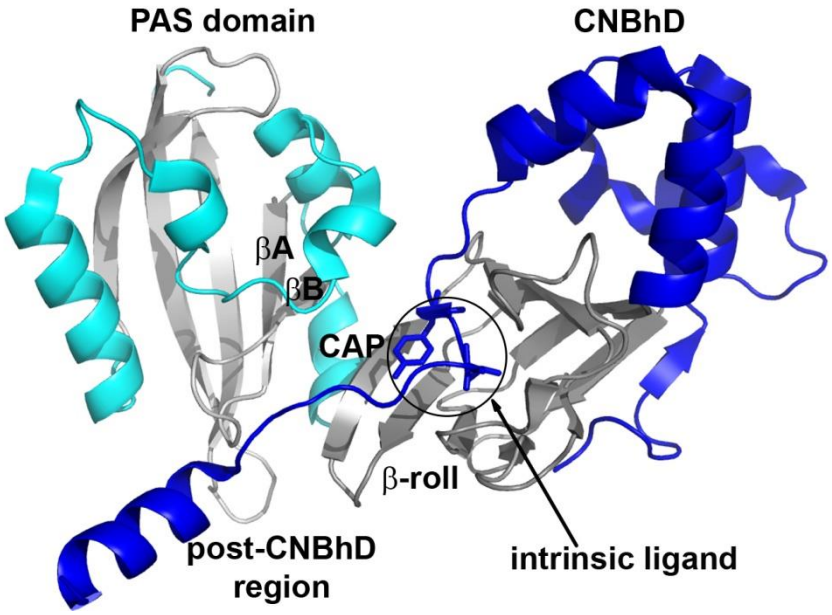

Figure 10 – Structure of the mEAG1 PAS/CNB-homology domain complex. PAS in cyan and CNB-homology domain (CNBhD) in dark blue. Intrinsic ligand is in stick representation. There are no structural changes relative to the isolated domains.

EAG1 calmodulin binding sites

It has been well established that, besides being regulated by voltage, the EAG1 channel activity is inhibited by Ca^{2+} (Stansfeld et al. 1996), an effect that is mediated through calmodulin (CaM) binding to the channel (Schönherr et al. 2000). With a half maximal inhibitory concentration (IC_{50}) of ~100 nM for Ca^{2+} (Schönherr et al. 2000) and 6 nM for calmodulin (Sahoo et al. 2010), EAG1 channels undergo inhibition just above basal cytosolic Ca^{2+} concentrations.

Three calmodulin binding sequences have been identified using a peptide array screen that spanned the entire human EAG1 cytoplasmic regions. BDN is found in the N-terminal cytoplasmic region, between the PAS domain and transmembrane helix TM1, BDC1 and BDC2 (Ziechner et al. 2006) are in the C terminus, immediately after the CNB-homology domain (Figure 3 and 11a). The *in vitro* affinity for Ca^{2+}-calmodulin was determined for the three sites using fluorescence correlation spectroscopy: 100-200 nM for BDN and BDC2, whereas for BDC1 the affinity varied between ~300 nM and more than 5 µM, depending on the fluorophore used. Deletion of the entire N-terminus renders the channel insensitive to CaM and affects the channel's gating properties (Ziechner et al. 2006; Carlson et al. 2013). Furthermore, it has also been shown that mutations that reduce calmodulin affinity at each of the three sites drastically reduce channel inhibition by Ca^{2+}-calmodulin (Figure

11a), supporting the functional importance of all three sites for Ca^{2+}-calmodulin regulation (Ziechner et al. 2006).

An in-cell fluorescence study has raised the possibility that a resident calmodulin is bound to BDN in the absence of Ca^{2+}, since FRET (Förster resonance energy transfer) could be observed between calmodulin and hEAG1 with mutated BDC2 (Gonçalves & Stühmer 2010); contradicts previous results that did not detect binding of apo-CaM to BDN or BDC2 peptides. The same fluorescence study demonstrated that, in the presence of Ca^{2+}, channels with disrupting mutations on BDN or BDC2 are still able to interact with calmodulin, although channels with mutated BDN, BDC2 and intact BDC1 no longer bind calmodulin (Gonçalves & Stühmer 2010). These results have raised the hypothesis that the lower affinity site BDC1 might not be physiologically relevant. More recently, the structure of mEAG1 CNB-homology domain, alone and in complex with the PAS domain, revealed BDC1 in a partially occluded conformation (Haitin et al. 2013b), supporting the idea that this site may not be relevant for CaM binding. Nevertheless, (Schönherr et al. 2000; Ziechner et al. 2006) have shown that all sites (BDN, BDC1 and BDC2) need to be intact and present in order for CaM to exert its inhibitory function.

The importance of the Ca^{2+} binding sites in CaM for the inhibition of EAG1 was also explored. Mutations on CaM's EF-hand motifs were introduced to disrupt Ca^{2+} binding (Ziechner et al. 2006). CaM N-lobe mutants showed a drop in affinity for BDN and BDC2 between 7 and 9-fold whereas C-lobe mutations abolished binding to the same peptides. The functional impact of these mutant calmodulins on EAG1 currents was compared to wild-type CaM; while the CaM N-lobe mutants showed big effects on inhibition, the C-lobe mutants failed to affect the channel currents (Figure 11b). This implies that CaM with just Ca^{2+} bound to the C-lobe is still able to inhibit EAG1 currents, although with less potency than wild-type CaM.

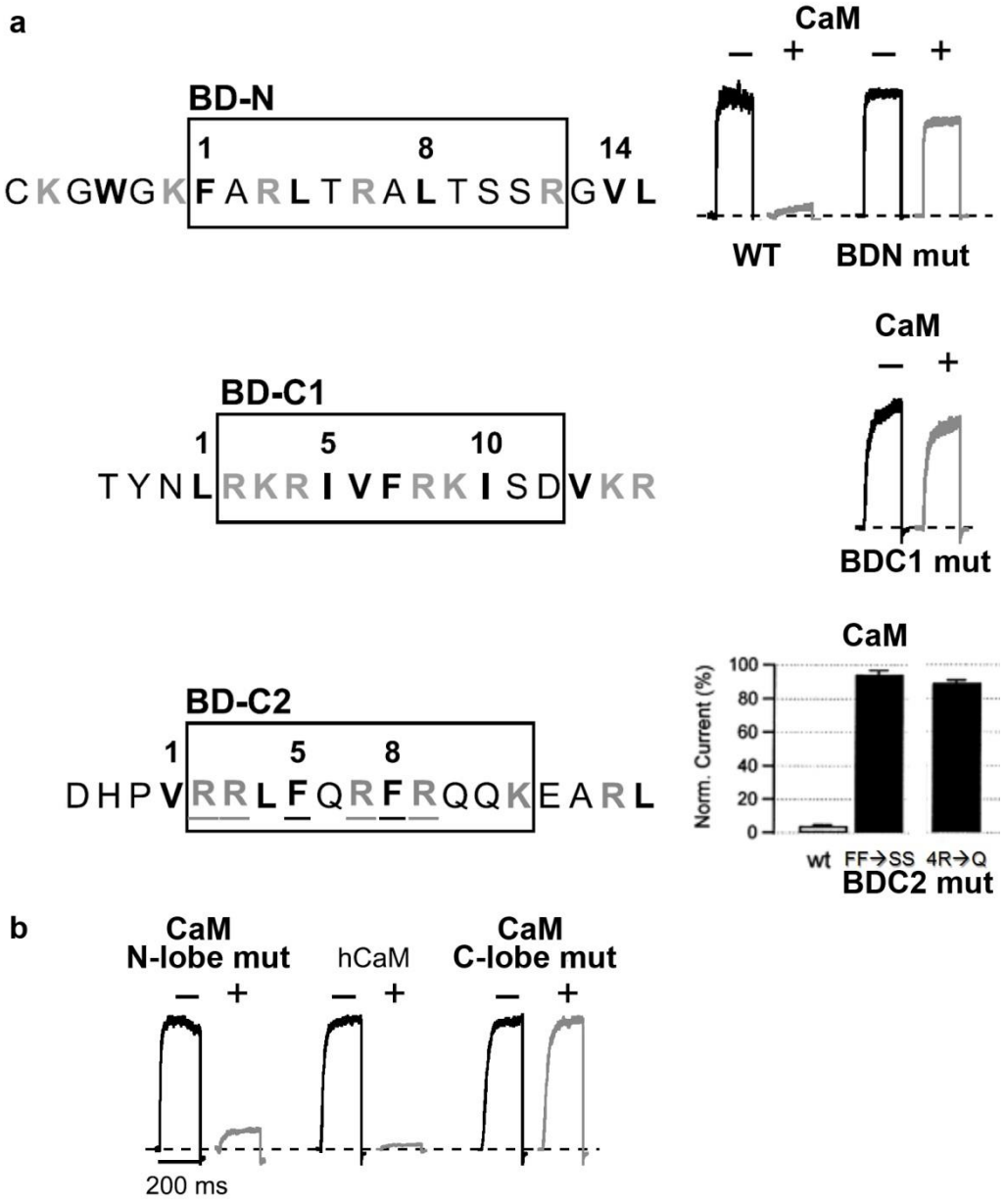

Figure 11 - a) EAG1 channel sequences corresponding to the peptides with the highest binding of fluorescently-labeled CaM - CaM binding sites BDN, BDC1 and BDC2. On the right, the funtional impact of mutations on BDN, BDC1 or BDC2 is depicted (mutant hEAG1 channels currents, in the absence and presence of Ca^{2+}-CaM). b) Functional impact on mutations in CaM's EF-hands (N-lobe and C-lobe) on wild-type hEAG1 channel currents.

Calmodulin

Calmodulin structure and plasticity

Calmodulin (CaM) is a highly conserved acidic protein, ubiquitous in eukaryotes, and it is composed by two globular domains – the N- and C-lobe – connected by a flexible linker (Figure 12a and b). In eukaryotic cells CaM is the main Ca^{2+} signaling protein, reaching concentrations between 10-100 µM; deletion of the CaM gene is lethal because of its involvement in numerous cellular processes (Yamniuk & Vogel 2004). CaM has been reported to interact with over 300 proteins, making calmodulin a limiting factor in calcium signaling in the cell since its total concentration is significantly lower than that of its targets (Persechini & Stemmer 2002).

Each CaM lobe contains two EF-hand motifs (named EF 1-4), helix-loop-helix motifs that can bind one Ca^{2+} each, up to a maximum of four Ca^{2+} ions per CaM molecule (Villarroel et al. 2014; Tidow & Nissen 2013). In the absence of target proteins, Ca^{2+} binds cooperatively to the C-lobe's EF-hands first, and then to the N-lobe's, with affinities of about 1 µM and 10 µM, respectively (Yamniuk & Vogel 2004). Ca^{2+} binding to CaM induces a conformational change that expose hydrophobic patches, increasing CaM's affinity to its targets (Yamniuk & Vogel 2004). However, CaM can also bind with high affinity to some targets in the absence of Ca^{2+} (e.g. IQ domains). In addition, binding to a target is reflected in increased affinity of CaM for Ca^{2+} (Villarroel et al. 2014; Yamniuk & Vogel 2004).

CaM contains an unusually high percentage of methionines in its composition; these are very flexible and highly polarizable residues which, together with many other hydrophobic residues, create very adjustable and sticky interaction surfaces. This feature, together with the very flexible interlobe linker that allows CaM to orient the lobes independently of each other, account for its ability to bind protein fragments with low sequence conservation (Yamniuk & Vogel 2004). Despite the lack of a consensus CaM binding sequence, CaM binding targets share some features such as high propensity to form amphipathic helices, net positive charge (basic residues), and a few hydrophobic residues that act as "anchors" (Rhoads & Friedberg 1997).

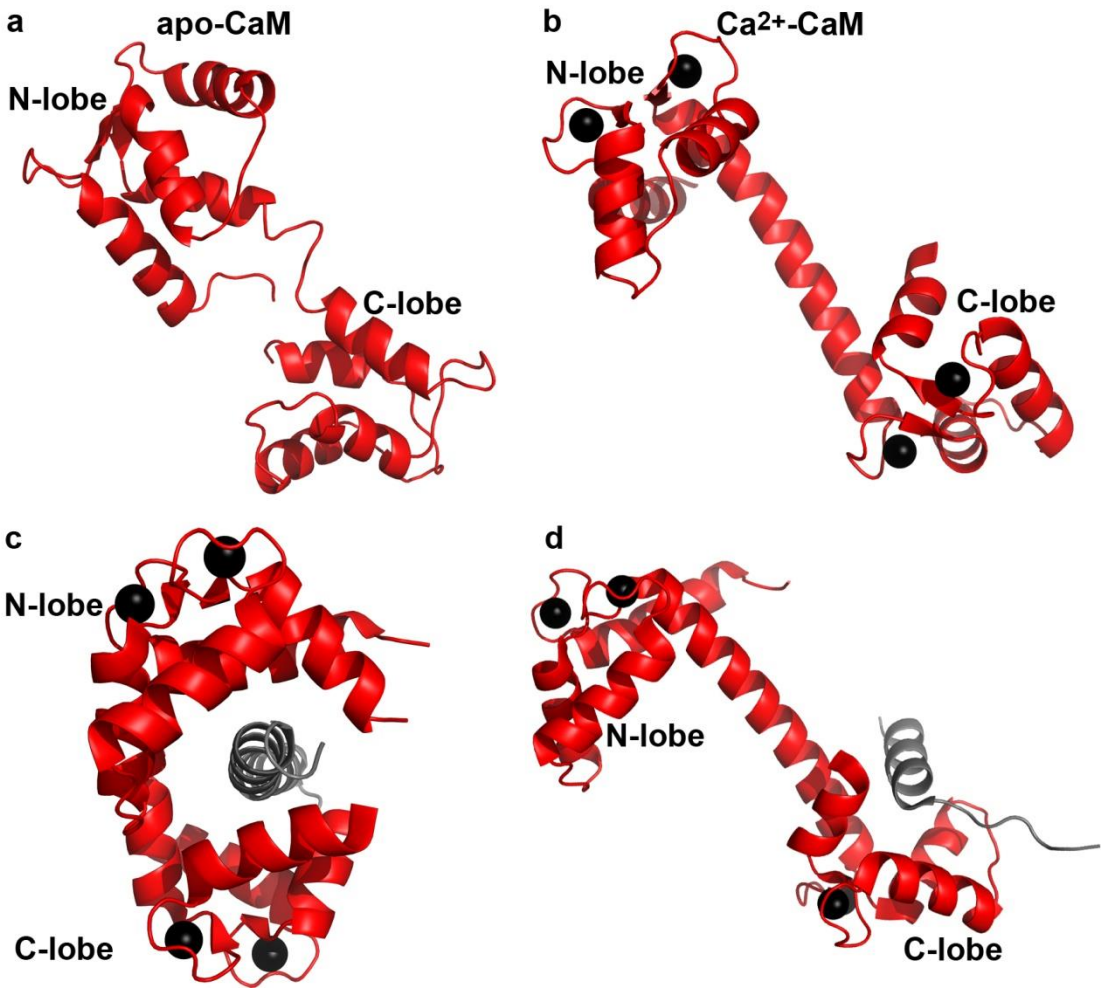

Figure 12 - Structures of calmodulin and CaM in complex with target peptides. CaM and peptides are in cartoon representation (red and grey, respectively) and Ca^{2+} is represented by black spheres. a) apo-CaM (PDB code 1CFD). b) Ca^{2+}-CaM (PDB code 3CLN). c) Ca^{2+}-CaM in complex with Cav IQ domain (PDB code 2BE6). d) Ca^{2+}-CaM in complex with an Orai channel fragment (PDB code 4EHQ).

The interaction of CaM with its targets is very diverse. In the canonical binding modes, the central linker unwinds allowing N- and C-lobe to be in close contact with the CaM binding sequence, adopting a collapsed conformation (Figure 12c). The canonical modes are classified by the spacing between the hydrophobic anchors that dock into CaM's hydrophobic pockets (e.g. the complex on Figure 12b has a 1-10 spacing). The non-canonical binding modes are very diverse in nature and do not involve "wrapping" of CaM around the target. CaM is in an elongated (or extended) conformation with either the N- or C-lobe engaging with the target (Figure 12d) and often the lobe that is not engaged with the target will not have Ca^{2+} bound.

CaM regulation of ion channels (CaM modulation)

Many ion channels are regulated by calmodulin (Saimi & Kung 2002). These include voltage-gated calcium (Ca_v), sodium (Na_v) and potassium channels (K_v), small conductance calcium-activated potassium channels (SK), inwardly rectifying potassium channels (Kir), cyclic nucleotide-gated ion channels (CNG), ryanodine receptors (RyR), transient receptor potential channels (TRP) and calcium release activated channel (Orai).

High resolution structures of CaM in complex with full-length ion channels have not yet been reported. Instead, there is an increasing number of structures of channel fragments in complex with CaM; however, despite extensive functional studies on CaM regulation in different ion channels, the molecular mechanisms of CaM action are not well understood. CaM regulation differs between different isoforms of the same channel family and depends on the cellular context (neuronal vs. cardiac channels, for example). This variation has prevented the formulation of a mechanism of CaM modulation for a particular channel family.

- Voltage-gated Ca^{2+} channels and voltage-gated Na^{+} channels

Voltage-gated calcium channels (Ca_v) are responsible for the transduction of membrane potential changes into transient increases in intracellular Ca^{2+} concentration, initiating many important physiological processes (Catterall 2011). Several sites for CaM binding have been identified in the N and C termini of these channels, although one CaM molecule seems to suffice for CaM modulation (Mori et al. 2004). The IQ domain present in the C-terminal cytoplasmic region is critical for this regulation (Van Petegem et al. 2005; Kim et al. 2010); in low calcium, apo-calmodulin is bound to the IQ domain of Ca^{2+}-channels and increases the channel's open probability (Adams et al. 2014). CaM functions as a resident Ca^{2+} sensor, with the C-lobe sensing local large Ca^{2+} oscillations due to ion influx through the Ca^{2+}-channel, while the N-lobe senses smaller changes in the global intracellular concentration of Ca^{2+} (Tadross et al. 2008). Upon Ca^{2+} entry through the Ca^{2+}-channels, CaM binds Ca^{2+} and the CaM conformational change presumably leads to subtle rearrangements in the C-terminal region of the channel that result in channel inhibition, a phenomenon called Ca^{2+}-dependent inactivation (CDI) (Ben-Johny & Yue 2014).

Several parallels have been drawn between CaM modulation of Ca_v channels voltage-gated sodium channels (Na_v). Still, CaM regulation of Na_v channels is less understood and the literature is inconsistent. Recently, it was reported that the skeletal muscle Na_v isoform exhibits fast CDI and that the CaM N-lobe functions as the Ca^{2+} sensor, similar to what

happens in Ca^{2+}-channels. However, the same report refuted previous studies by showing that the cardiac Na_v isoform is not modulated by Ca^{2+} (Ben-Johny et al. 2014), despite the high sequence similarity in the IQ region.

- KCNQ (Kv7) voltage-gated K^+ channels

CaM affects the function of all channels in the Kv7 voltage-gated potassium channel family. CaM interacts with two regions in the C terminus of this channel – an IQ motif and a 1-5-10 motif, that are 135 residues apart (Alaimo et al. 2014; Xu et al. 2013; Mruk et al. 2012). CaM binding regulates channel assembly, trafficking and function. Apo-CaM is bound constitutively to Kv7 channels through the IQ-domain and Ca^{2+}-CaM regulates these channels by altering their voltage-dependent activation, resulting in an increase or decrease in current, depending on the channel isoform.

- Small conductance Ca^{2+}-activated K^+ (SK) channels

SK channels contain a CaM binding site after the last transmembrane helix. CaM is bound to SK channels, even in the absence of Ca^{2+}; the channel is activated upon Ca^{2+} binding to CaM. SK channels co-expressed with CaM mutated in the N-lobe's EF-hands (not able to bind Ca^{2+} on the N-lobe) showed no activity whereas SK channels co-expressed with CaM mutated in C-lobe's EF-hands were still activated by Ca^{2+} (Adelman 2015).

Structural studies on the interaction between CaM and the SK2 CaM binding site showed that apo-CaM is bound via the C-lobe, leaving the N-lobe free to interact with other binding sites from neighboring subunits (Schumacher et al. 2004). In the presence of Ca^{2+}, solution studies and an X-ray structure showed that there is CaM-induced dimerization of this channel region. CaM is in an elongated form, interacting with three different helices from two different CaM binding sites (Schumacher et al. 2001). The N-lobe has Ca^{2+} and interacts with one CaM binding site while the C-lobe interacts with two helices from the other CaM binding site monomer; the C-lobe has its EF-hands distorted, without Ca^{2+}.

It has been proposed that gating involves Ca^{2+} binding to the N-lobe, inducing this lobe to interact with the distal part of a CaM binding site from another channel subunit. This conformational change is then transmitted to the adjacent TM6 helix in the gate region, resulting in channel opening.

II. AIMS OF THE STUDY

The aim of this work is to gain insights into: 1) the structure and function of the CNB-homology domain; and 2) the interaction of calmodulin with the cytoplasmic regions of the EAG1 channel.

Some of the questions we are asking are:

- Does the CNB-homology domain have an unliganded conformation?
- Does the CNB-homology domain have a role in KCNH channel gating?
- Does calmodulin bind to the EAG1 CaM binding sites in a lobe-specific manner?
- Do the neighboring globular domains PAS and CNB-homology domain alter the affinity of calmodulin for the calmodulin binding sites?

To address these questions I have performed a thorough structural, biochemical and functional characterization of the cytoplasmic regions of EAG channels that surround the CaM binding sites BDN, BDC1 and BDC2. The work has two focal points: the biochemical and thermodynamic characterization of the interaction between calmodulin and different channel regions and the structural characterization of these interactions. This characterization was pursued using biophysical techniques such as isothermal titration calorimetry, x-ray crystallography and fluorescence spectroscopy as well biochemical analysis.

III. CHARACTERIZATION OF THE CYCLIC NUCLEOTIDE BINDING HOMOLOGY-DOMAIN FROM EAG1 CHANNEL

The work described in this section has been published in:

Marques-Carvalho, M.J.; Sahoo, N.; Muskett, F.W.; Vieira-Pires, R.S.; Gabant, G; Cadene, M.; Schönherr, R.; Morais-Cabral, J.H.,. "Structural, biochemical, and functional characterization of the cyclic nucleotide binding homology domain from the mouse EAG1 potassium channel." *Journal of Molecular Biology*, 423(1), pp.34–46, 2012.

INTRODUCTION

The structures of the CNB-homology domains from all KCNH subfamilies revealed a common feature – a short β-strand after the αC helix that includes the "intrinsic ligand", two residues that occupy the cavity where cyclic nucleotides bind in *bona fide* CNB domains. We call this a "self-liganded" conformation since the intrinsic ligand is bound in the β-roll pocket keeping the helix αC and the C-terminal tail tightly packed against the domain.

In this section, we set out to characterize biochemically and functionally this self-liganded conformation. In addition, we explored the possible existence of an unliganded conformation. We tried to destabilize the self-liganded state either by mutating the intrinsic ligand residues or by assessing if CaM binding to BDC1 displaces the C-terminal tail away from the domain.

METHODS

Expression and purification of mEAG1 channel fragments

mEAG1 residues 552–724 and 552–736 were cloned into co-expression vector pRSFDuet-1 (Novagen). A fusion of maltose-binding protein with mEAG1 BDC1 (residues 696–736) was also cloned into pRSFDuet-1. Mutants were created using the QuikChange Site-Directed Mutagenesis Kit (Stratagene).

Escherichia coli BL21 (DE3) competent cells transformed with an expression vector were grown at 37 ºC with agitation in Luria broth medium supplemented with kanamycin (50 mg/L) until the 600 nm optical density (OD600) reached 0.6–0.8. At this point, cultures

were placed on ice for 30 min (to induce cold-shock chaperones). Ethanol was then added dropwise to a final concentration of 2%(v/v) (to induce expression of heat-shock chaperones); IPTG was added to a final concentration of 0.5 mM for overnight induction at 18 ºC (12–16 h). Cultures were harvested by centrifugation at 4785xg for 20 min at 4 ºC and the resulting pellet was resuspended in buffer A (1 L pellet in 20 mL of 50 mM Tris-HCl pH 8, 150 mM NaCl, 5 mM imidazole) supplemented with protease inhibitors: 1 mM PMSF, 1 mg/mL leupeptin, 1 mg/mL pepstatin. Cell lysis was performed in a cooled cell cracker (Emulsiflex-C5, Avestin) and the lysate was centrifuged at 32 800xg for 45 min at 4 ºC to remove cell debris. The supernatant was loaded onto His-select Nickel Affinity Gel (Sigma) pre-equilibrated with buffer A and washed with buffer A until the 280 nm optical density (OD280) stabilized. While monitoring the OD280 of the eluate, the beads were first washed with buffer A + 300 mM NaCl and buffer A containing 20 mM imidazole. Protein was eluted with buffer A containing 150 mM imidazole.

To remove the imidazole, the eluted protein was dialyzed against buffer B containing 50 mM Tris-HCl pH 7.5, 150 mM NaCl and 5 mM DTT and loaded into an S200 size-exclusion chromatography column (GE Healthcare), pre-equilibrated with the same buffer.

Protein for fluorescence binding assays was dialyzed against fluorescence buffer [50 mM Tris–HCl, pH 7.5, 150 mM NaCl, 5 mM $MgCl_2$, 0.1mM ethylene glycol bis(β-aminoethyl ether) N,N′-tetraacetic acid (EGTA), and 2 mM $CaCl_2$ (1.9 mM free Ca^{2+})]

Expression and purification of calmodulin

Escherichia coli BL21(DE3) competent cells were transformed with expression vector (pT7-7 hCaM) and plated on LB agar+ampicillin; the following day resuspended colonies were grown in liquid LB+ampicillin at 37 °C, 160 rpm until they reached an OD600 between 0.6-0.8. 0.5 mM IPTG was added followed by a 3h induction at 37 °C.

Cultures were harvested by centrifugation at 4785xg, 20 min, 4 °C (Beckman rotor JLA 8-1000) and the resulting pellet was either stored at -20 °C or immediately resuspended in lysis buffer (refer to table 1 for buffer composition) supplemented with the protease inhibitors PMSF (1 mM), leupeptin (1 µg/mL) and pepstatin (1 µg/mL). Cells were lysed in a cooled cell cracker (Emulsiflex-C5, AVESTIN). The lysate was centrifuged at 32 800xg (Beckman rotor JA-25.50) for 45 min at 4 °C to remove cell debris. Supernatant was loaded into a Phenyl Sepharose CL-4B (Sigma-Aldrich) column equilibrated in EDTA buffer to retain proteins that bind in a calcium-independent manner. The flow-through that contains CaM was collected and $CaCl_2$ was added to a final concentration of 5 mM. The calcium supplemented flow-through was loaded onto another phenyl sepharose column

equilibrated in calcium buffer. This second step allows CaM to interact with the phenyl sepharose matrix. Washes were made with calcium buffer + NaCl and calcium buffer. Calmodulin was eluted with EDTA buffer. Protein purity was evaluated by SDS-PAGE and concentration was determined by measuring absorbance at 277 nm (calmodulin does not have any tryptophans in the sequence, using the extinction coefficient ε_{277}=3029 M^{-1} cm^{-1} (Strasburg et al. 1988). Calmodulin was dialyzed against storage buffer using a dialysis membrane with 3.5 KDa cutoff and stored at -80 °C.

Table 1 – Composition of the buffers used for calmodulin purification

	Tris HCl pH 7.5 (mM)	NaCl (mM)	EDTA (mM)	DTT (mM)	$CaCl_2$ (mM)	NaN_3 (mM)
Lysis buffer (EDTA buffer + NaCl)	50	100	2	5	0	0
EDTA buffer	50	0	2	5	0	0
Calcium buffer	50	0	0	5	1	0
Calcium buffer + NaCl	50	100	0	5	1	0
Storage buffer	20	150	0	0	0	1

Derivatization of calmodulin with the fluorophore Dansyl-Cl

Wild-type human calmodulin was derivatized with 5-(dimethylamino) naphthalene-1-sulfonyl chloride (Dansyl-Cl, Molecular Probes), a reagent that reacts with primary amines, as previously described (Kincaid et al. 1988; Kincaid et al. 1982).

Briefly, calmodulin was passed through a desalting column equilibrated in in a buffer containing 20 mM sodium bicarbonate pH 10, 100 mM NaCl, 250 µM $CaCl_2$. Desalted CaM was incubated with 1.5-fold molar excess of Dansyl-Cl dissolved in dry acetone for 90 min at room temperature. The reaction was stopped by the addition of 50 mM Tris-HCl pH 8. The derivatized protein was desalted in fluorescence buffer (50 mM Tris HCl pH 7.5, 150 mM NaCl, 5 mM $MgCl_2$, 0.1 mM EGTA and 2 mM $CaCl_2$ (1.9 mM free Ca^{2+})).

Fluorescence assay

Dansylated-calmodulin at 400 nM was incubated with increasing protein concentrations at room temperature, for at least 20 min, in fluorescence buffer (50 mM Tris HCl pH 7.5, 150 mM NaCl, 5 mM $MgCl_2$, 0.1 mM EGTA and 2 mM $CaCl_2$ (1.9 mM free Ca^{2+})). Fluorescent measurements were performed at 26 °C using a Horiba Fluoromax-4 spectrofluorimeter. All emission spectra were recorded with an excitation wavelength of 340 nm and slit widths of 4 or 5 nm [18]. For each titration curve, fluorescence intensity was measured at the wavelength corresponding to the maximum shift in the emission spectra. Data were

normalized using $F_{norm} = (F-F_0)/(F_{max}-F_0)$. Where F is the measured fluorescence value for each protein concentration, F_{max} is the maximum measured fluorescence and F_0 is the measured fluorescence before adding any mEAG1 protein fragment. F_{norm} was plotted as a function of total protein concentration using OriginPro8. Data were fitted to a modified hyperbolic function of the form: $F_{norm} = \alpha/(1+2/(-1-(1/K_D)[\text{dansyl-CaM}]+(1/K_D)[\text{mEAG1}]+\text{sqrt}((1+(1/K_D)[\text{dansyl-CaM}]-(1/K_D)[\text{mEAG1}])^2+4(1/K_D)[\text{mEAG1}])))$,where K_D is the dissociation constant, [dansyl-CaM] is the total concentration of dansylated-calmodulin, [mEAG1] is the total concentration of mouse EAG1 domain and *α* is an adjusting factor.

Competition experiments were performed in the presence of 4 μM of WT calmodulin and data were fitted to the function [35]:

$F_{norm} = \alpha(2\cos(d/3)\text{sqrt}(a^2-3b)-a)/(3(1/K_D\text{dansyl})+(2\cos(d/3)\text{sqrt}(a^2-3b)-a))$.

$a = (1/K_D\text{dansyl})+(1/K_D\text{WT})+[\text{dansyl-CaM}]+[\text{WT-CaM}]+[\text{mEAG1}]$;

$b = (1/K_D\text{WT})([\text{dansyl-CaM}]-[\text{mEAG1}])+(1/K_D\text{dansyl})([\text{WT-CaM}]-[\text{mEAG1}])+(1/K_D\text{dansyl})(1/K_D\text{WT})$;

$c = -(1/K_D\text{dansyl})(1/K_D\text{WT})[\text{mEAG1}]$;

$d = \text{acos}((-2a^3+9ab-27c)/(2\text{sqrt}((a^2-3b)^3)))$.

, where $K_D$dansyl is the dissociation constant for dansylated-calmodulin, K_DWT is the dissociation constant for wild-type calmodulin, [dansyl-CaM] is the total concentration of dansylated-calmodulin, [WT-CaM] is the total concentration of wild-type calmodulin, [mEAG1] is the total concentration of mouse EAG1 domain and *α* is an adjusting factor.

Pegylation assay

Wild type mEAG1 552-724 was diluted to 2 μM in fluorescence buffer with 1mM TCEP, and incubated at room temperature for 1h in the presence and absence of 50 μM calmodulin. Methoxypolyethylene glycol maleimide (MAL-PEG, Fluka/Sigma-Aldrich) was added to the protein mixture at 5 mM and incubated at 4 °C for 5, 10 min. Reactions were stopped by addition of DTT to a final concentration of 200 mM, incubation for 30 minutes and addition of SDS-PAGE loading buffer. Samples were run on a 15% SDS-PAGE and analyzed by Western Blot. Proteins were probed with an anti-His-tag monoclonal antibody (Qiagen).

Mass spectrometry

Proteins were analyzed by MALDI-TOF MS. The matrix solution consisted of saturated 4-hydroxy-α-cyano-cinnamic acid in 66.5% H_2O, 33.3% CH_3CN, 0.1% TFA. Analytes in the micromolar range were prepared by twenty-fold to two hundred-fold dilution into the matrix solution. The analyte-matrix samples were spotted onto a gold-plated sample probe using the ultra-thin layer method as described (Cadene & Chait 2000; Gabant & Cadene 2008) and analyzed in linear positive ion mode. Spots were washed with 0.1% TFA before acquisition. Analyses were performed using an Autoflex I or an Ultraflex I mass spectrometer (Bruker Daltonics, Germany) equipped with a 337 nm nitrogen laser and a gridless delayed extraction ion source. An accelerating voltage of 20kV was used and delay was optimized between 500 and 650 ns to achieve a mass resolution greater than 1000 over the mass range of interest (10000–20000 Da). A deflection of matrix ions up to 600 Da was applied to prevent detector saturation. Spectra were acquired in linear positive ion mode by accumulation of 300-500 laser shots. The instrument was controlled using Bruker FlexControl software. Calibration was performed externally using apomyoglobin and cytochrome c. MALDI-TOF-MS spectra were processed using FlexAnalysis 2.0 software from Bruker Daltonics and cleavage peptides assigned using Paws version 8.5.0.3 (ProteoMetrics, New York, NY).

NMR Spectroscopy

NMR spectra for the backbone assignment of CaM were acquired from 0.35 ml samples of 0.4 mM calmodulin in a 20 mM Tris, 140 mM sodium chloride, 10mM $CaCl_2$, 0.2mM AEBSF and 0.02% (w/v) sodium azide buffer at pH 7.5, containing 5% D_2O/95% H_2O. All NMR experiments were acquired at 298K and were performed on Bruker DRX or AvanceII spectrometers operating at either 600 or 800MHz that were fitted with cryogenically cooled probe-heads. The 2D and 3D spectra recorded to obtain sequence specific assignments for CaM were: $^{15}N/^{1}H$ HSQC; NOESY-HSQC with an NOE mixing time of 100 ms; $^{13}C/^{1}H$ HSQC and $^{15}N/^{13}C/^{1}H$ HNCACB, CBCA(CO)NH, HNCA and HN(CO)CA ((Bax 1994), and references therein). Typical acquisition times in F_1 and F_2 for the 3D experiments were 20 ms for ^{15}N, 6.6-9.6ms for ^{13}C and 18ms for ^{1}H and with an acquisition time of 80 ms in F_3 (^{1}H). The majority of the 3D spectra were collected over approximately 48 hours and $^{15}N/^{1}H$ and $^{13}C/^{1}H$ HSQC spectra over about 1 hour. Typical acquisition times in 2D experiments were either 60 ms (^{15}N), 9 ms (^{13}C) and 80 ms in F_2 (^{1}H). Water suppression was achieved using the gradient based WATERGATE method (Sklenar et al. 1993). The 3D NMR data were processed using NMRPipe (Delaglio et al. 1995) with linear prediction used to extend the effective acquisition times by up to 2 fold in

F_1 and F_2. The resulting spectra analysed using the program Sparky (T.D. Goddard and D.G. Kneller, Sparky 3, University of California, San Francisco).

NMR chemical shift mapping of binding sites

$^{15}N/^{1}H$ TROSY (Pervushin et al. 1997) spectra of calmodulin were acquired in the presence and absence of mEAG1 552-724 to identify the changes in the positions of signals induced by CNB-homology domain binding. In these experiments, amounts of unlabeled mEAG1 552-724 were added to 100 µM ^{15}N-labelled calmodulin to achieve 30% and 90% saturation of calmodulin based on the determined K_D. Experiments were performed in the same buffer as used for calmodulin assignment but with the addition of 2mM DTT. Typical acquisition times for the TROSY experiments were 80 ms in F_2 (^{1}H), and 30 ms in F_1 (^{15}N), with the spectra collected over approximately 3 hours. Perturbation of backbone amide chemical shifts in the presence of mEAG1 552-724 was calculated relative to calmodulin alone using the minimum chemical shift procedure (Williamson et al. 1997; Farmer et al. 1996) and then used to identify the intramolecular interface of mEAG1 552-724 on calmodulin.

Electrophysiological measurements and data analysis

Recording and data analysis were described previously (Schönherr et al. 1999). In brief, stage V *Xenopus* oocytes were injected with 50 nL mRNA and currents were recorded at 20–23 °C, 2 to 4 days after injection. A two-electrode voltage clamp amplifier (Turbo-TEC 10CD, NPI electronic, Tamm, Germany) was controlled by PatchMaster software (HEKA Elektronik, Lambrecht, Germany). A P/n method was used for leak correction. The bath solution contained (in mM): 115 NaCl, 2.5 KCl, 1.8 CaCl2, 10 HEPES; pH 7.2 (NaOH). Data were analyzed with FitMaster software (HEKA Elektronik). Normalized conductances were obtained by fitting the following equation to the current-voltage data:

$$I(V)=GV(1-e^{-((V-Erev)/25mV)})/(1-e^{-(V/25mV)})*1/(1+e^{-((V-V1/2)/k)})$$

G is the maximal conductance and E_{rev} the estimated reversal potential. The second term describes the channel open probability (or relative conductance), characterized by $V_{1/2}$, the voltage of half-maximal activation, and a slope factor, k.

RESULTS

Biochemical analysis of the self-liganded conformation

An underlying implication of the proposal that CNB-homology domain adopts a self-liganded conformation is that an unliganded conformation might exist, however no evidence for this other conformation has been provided. In this context it is interesting to realize that in our structure the C-terminal tail includes a significant amino acid stretch (residues 702 to 707) of the previously identified low affinity BDC1 calmodulin binding site (residues 702 to 712) (Figure 13) (Ziechner et al. 2006). This CaM binding sequence does not exist in the CNB-homology domain of zELK or agERG. The site starts immediately after the two residues (Y699 and L701) bound in the pocket and is partially occluded by steric contacts with residues on the surface of the domain. Considering the molecular volume of calmodulin it becomes clear that the steric occlusion of the BDC1 site will affect binding of calmodulin and that tight interaction between the two proteins will only occur when the site becomes accessible upon displacement of most of the C-terminal tail away from the domain. This new conformation would correspond to an unliganded state. Importantly, in an unliganded conformation the apparent affinity of Ca^{2+}-calmodulin will be higher than in the self-liganded state and therefore mutations that destabilize the self-liganded conformation would increase calmodulin affinity.

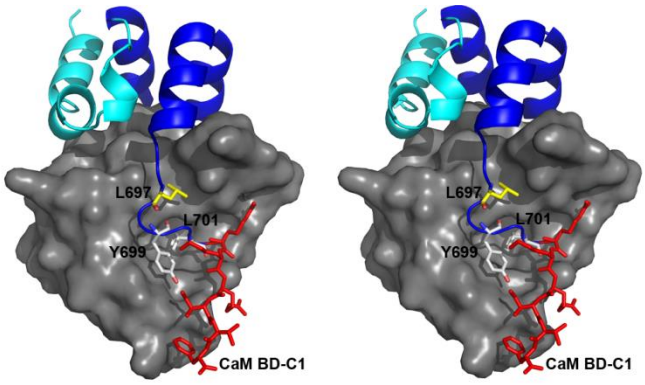

Figure 13 - Stereo view of the CNB-homology domain with the two conserved residues bound in the binding pocket. β-roll is shown as surface representation. Residues from C-terminal tail that reside in the pocket (Y699 and L701) are show in white stick; residue L697 is shown in yellow stick. Section of the calmodulin BDC1 binding site present in the structure is shown in red sticks.

To explore the existence of an unliganded state we performed a series of biochemical experiments using dansylated-calmodulin, a fluorescent form of the protein (Kincaid et al.

1988). Dansylated-calmodulin has previously been reported to have similar properties to native calmodulin and we ensured that the calmodulin used in our experiments had on average just over 1 dansyl group per protein molecule, as evaluated by mass spectrometry. We first determined the affinity of Ca^{2+}/dansyl-calmodulin for BDC1 (K_D 1.0 ± 0.1 µM, Figure 14a) by fusing the peptide sequence (residues 696 to 736 of mEAG1) to maltose-binding protein (MPB-BDC1) through a long linker. A competition experiment with wild-type (WT) calmodulin confirmed that both labeled and unlabeled forms of calmodulin have similar binding properties (K_D 1.2 ± 0.1 µM for Ca^{2+}/WT-calmodulin, Figure 14a) and we made use of the modified calmodulin for the rest of our study. We also verified that calmodulin does not bind to MBP alone and that in the absence of Ca^{2+} binding to BDC1 is not detectable (Figure 15c and d). Taken together, these results confirmed previous reports of weak calmodulin binding at the BDC1 site (Ziechner et al. 2006).

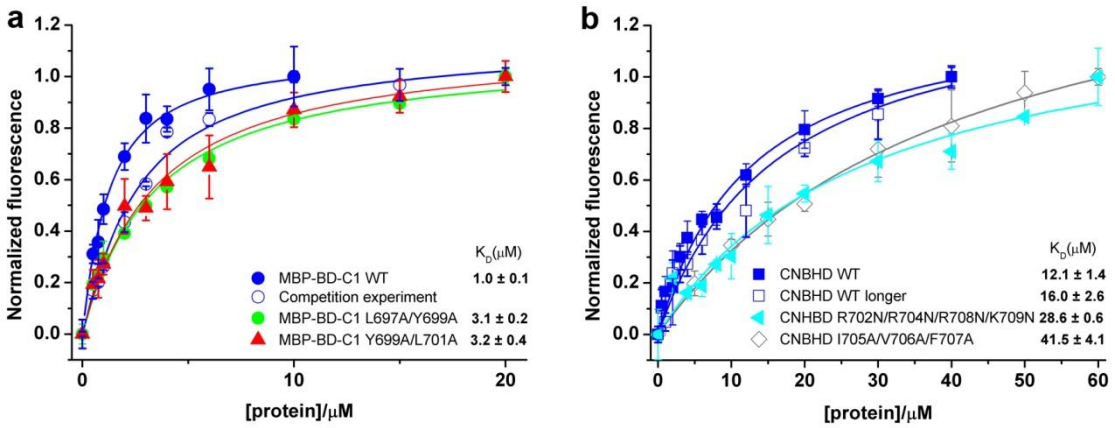

Figure 14 - Fluorescence binding curves with dansylated-calmodulin. **a)** Titration with calmodulin binding site BDC1 fused to MBP (blue ●, N=7). Competition experiment with WT calmodulin (blue ○, N=6). MBP-BDC1 fusion with mutations L697A/Y699A (green ●, N=3) and Y699A/L701A (red ▲, N=3). **b)** Titration with mouse EAG1 protein fragments that span the CNB-homology domain and the calmodulin binding site BDC1. Wild-type mEAG1 spanning residues 552 to 724 (blue ■, N=4) and spanning residues 552-736 (blue □, N=4). mEAG1 552-724 with mutations in the calmodulin binding site: R702N/R704N/R708N/K709N (cyan◀, N=2) and I705A/V706A/F707A (grey ◊, N=3). Error bars represent mean standard deviation.

We then measured the affinity of Ca^{2+}/dansyl-calmodulin for two different constructs spanning the complete CNB-homology domain and the whole BDC1 site (residues 552-724 and 552-736). Calmodulin affinity to these constructs is 10- to 20-fold lower than that

measured for the BDC1 site alone, with K_D values of 12.1 ± 1.4 μM and 16 ± 2.6 μM for the shorter and longer constructs, respectively (Figure 14b). This is consistent with our observation in the structure of partial steric occlusion of BDC1. From this point onward we used the smaller CNB-homology domain-BDC1 construct (residues 552-724).

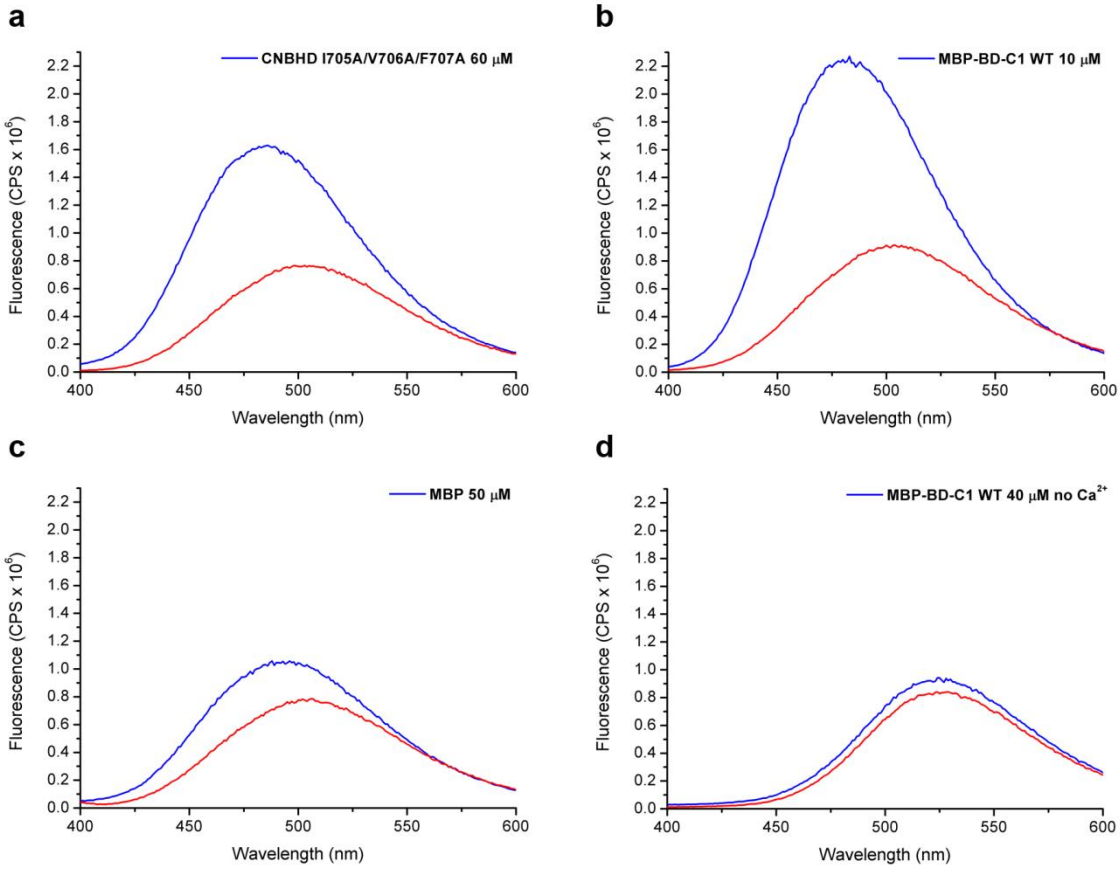

Figure 15 - Emission fluorescence spectra from dansyl-calmodulin titrated with different protein constructs. Red curve is spectra for dansyl-calmodulin alone and blue curve for dansyl-calmodulin titrated with maximum concentration of protein, as indicated on each graph. a) Titration with CNB-homology domain (CNBhD) triple BDC1 site mutant up to 60 μM causes a shift of the emission maximum from 503 nm to 485 nm and an increase in intensity of more than 2-fold. b) Titration with fusion Maltose binding protein-BDC1 site (MBP-BDC1 up to 10 μM) causes a shift of the emission maximum from 504 nm to 482 nm and an increase in intensity of ~2.5-fold. c) Titration with MBP alone (up to 50 μM) causes a minor shift of the emission maximum from 505 nm to 493 nm and an increase in intensity of just ~1.4-fold. The very small blue shift and small increase in fluorescence are an indication of a very weak interaction, much weaker than the interaction measured in a) which has a K_D ~40 μM. d) Titration with MBP-BDC1 in the presence of EGTA (up to 40 μM) does not cause any change in the fluorescence, indicating that calmodulin does not bind to this protein in the absence of Ca^{2+}.

By mutating residues that appear to hold the C-terminal tail in position we should destabilize the self-liganded conformation and thus increase the apparent affinity for calmodulin. In the CNBhD-BDC1 construct we generated the C-terminal tail double-mutants L697A/Y699A and Y699A/L701A. Y699 and L701 are the two residues in the domain structure which interact with the domain pocket (Figure 9b, 13); L697 is not in the pocket but has extensive contacts with residues in the β-roll (Figure 13). As was predicted above, the affinity of calmodulin for these mutant domains is higher than that of the wild-type domain (Figure 16a), K_D 2.6 ± 0.2 µM for L697A/Y699A and 3.8 ± 0.5 µM for Y699A/L701A.

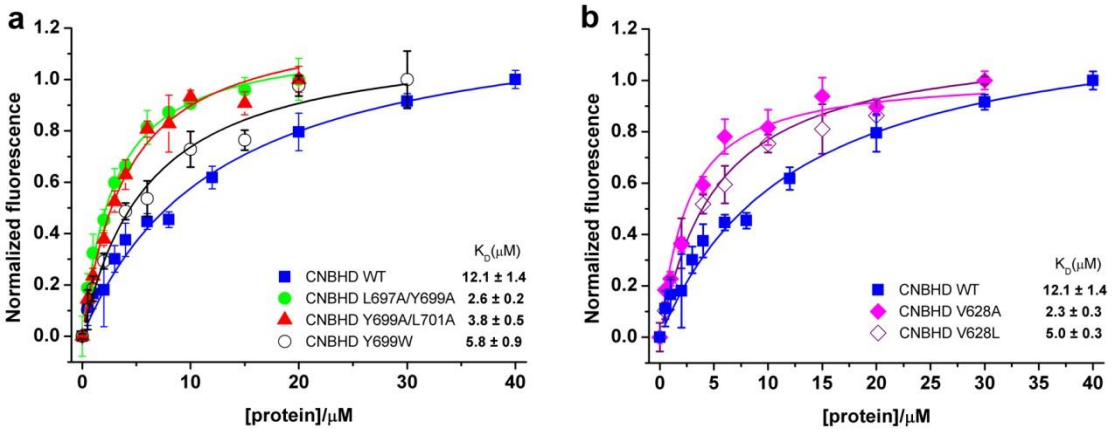

Figure 16 - Fluorescence binding curves with dansylated-calmodulin. **a)** Titration with C-terminal tail mutants of mEAG1 552-724, comparison with WT (blue ■). Mutants L697A/Y699A (green ●, N=3), Y699A/L701A (red ▲, N=3) and Y699W (black ○, N=3). **b)** Titration with binding pocket mutants of mEAG1 552-724, comparison with WT (blue ■). Mutants V628A (magenta, N=3) and V628L (purple ◊, N=3). Error bars are mean standard deviation.

We also analyzed the same double mutants (L697A/Y699A and Y699A/L701A) as MBP-BDC1 fusions using dansyl-CaM. As shown in Figure 14a, the mutants show similar affinities (L697A/Y699A has a K_D of 3.1 ± 0.2 µM, and Y699A/L701A has a K_D of 3.2 ± 0.4 µM) to the ones determined above for the same mutants in the domain. This similarity supports the notion that in these mutant domains the BDC1 site is as accessible as in the MBP fusion and therefore that the C-terminal tail has peeled away from the domain and is exposed. In addition, the small but significant effect of the double mutations in MBP-BDC1 relative to the wild-type MBP fusion (Figure 14a) shows that calmodulin binding to BDC1 extends all the way to these residues.

Other mutations that are expected to destabilize the self-liganded conformation were also analyzed. The single-residue change Y699W, in the C-terminal tail, also increased the apparent calmodulin affinity but had a milder effect, K_D ~ 6 µM (Figure 16a). Importantly, mutations of a residue in the pocket, which in the structure interacts with Y699, also lead to an increase in apparent calmodulin affinity: V628A and V628L have K_D values of 2.3 and 5 µM, respectively (Figure 16b).

To better understand the weak interaction between calmodulin and the CNBhD-BDC1 channel fragment our collaborator Dr. Frederick Muskett at the University of Leicester, UK used NMR and performed a minimal chemical shift mapping with ^{15}N-labeled calmodulin (Farmer et al. 1996; Williamson et al. 1997). In this experiment we looked exclusively at the changes that occur in calmodulin upon interaction with the domain. Plotting of the minimal chemical shift data (*i.e.* the sum of the root-mean-square differences in nitrogen and proton chemical shift between free and bound Ca^{2+}-calmodulin) shows that upon binding, the large changes (mean chemical shift difference ≥ 0.08 ppm) are mainly concentrated in residues of the N-terminal lobe of calmodulin (Figure 17a). We mapped the chemical shift data onto a representative structure of calmodulin bound to a peptide stretch (PDB 3OXQ, chain A) (Kim et al. 2010). Our model shows that the large chemical shifts occur in residues directly involved in the interaction with the peptide (Figure 17b). In contrast, in the C-lobe the major change occurs in T146, which does not interact directly with the bound helix (Figure 17c). These results indicate that binding to BDC1 occurs through the calmodulin N-lobe with little participation of the C-lobe, providing an explanation for the low affinity of Ca^{2+}-calmodulin to the BDC1 site. This type of single lobe interaction has been described in the literature for calmodulin interaction with sites in voltage-gated calcium channels (Kim et al. 2010) and in voltage-gated sodium channels (Sarhan et al. 2012). Importantly, the data strongly supports the idea that, despite being weak, the *in vitro* interaction of the N-lobe of calmodulin with BDC1 has the hallmarks of a canonical interaction between a calmodulin lobe and a protein segment and is extensive since it involves residues across the binding surface of the N-lobe.

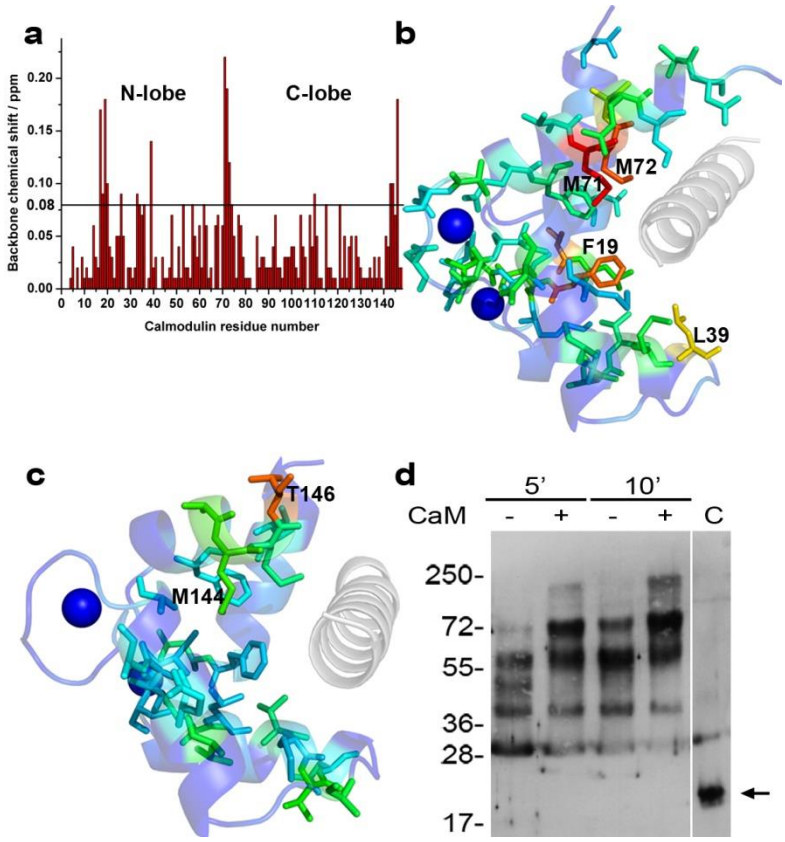

Figure 17 - Structural changes induced by calmodulin binding. a) Plot of backbone residue chemical shift changes that occur upon binding to mEAG1 552-724. Horizontal line marks cutoff of 0.08 ppm used for large changes. b) Mapping of chemical shifts onto the structure of calmodulin N-lobe bound to a helical peptide (from PDB code 3OXQ). Calmodulin residues are rainbow colored (dark-blue to red) according to chemical shift difference (0.0-0.22ppm). c) Structure of calmodulin C-lobe bound to helical peptide (from PDB code 3OXQ) colored as in b). d) Western-blot analysis of aliquots from pegylation reaction. Pegylation of wild-type mEAG1 552-724 was performed in the presence (+) and absence (-) of saturating concentrations of Ca^{2+}-calmodulin and stopped at 5 min and 10 min. Unmodified mEAG1 552-724 (lane C) is indicated by arrow. Western probed with an anti-His-tag monoclonal antibody.

Overall, the data confirms our expectation that the occlusion of BDC1 weakens the interaction between the domain and calmodulin. Moreover, destabilization of the self-liganded conformation can be achieved through mutagenesis of residues that in the structure appear to hold the C-terminal tail in position. Importantly, the data also shows that much of the stability of the self-liganded conformation results from the residues that interact in the pocket of the domain since mutation of these residues caused the largest increase in calmodulin affinity. However, these experiments do not demonstrate that

calmodulin binding to the domain causes destabilization of the self-liganded state. We cannot rule out that the interaction of calmodulin with the CNBhD-BDC1 channel fragment involves only part of the binding site. It could happen that the interaction is occurring just with the C-terminal end of the site. In this position calmodulin is away from the domain and it may not affect its conformation. Binding to the whole BDC1 site would occur only upon destabilization of the self-liganded conformation by mutagenesis which would result in the release of the C-terminal tail and exposure of the site.

To address this issue we performed two different biochemical experiments. First, we showed that the calmodulin interaction with the CNBhD-BDC1 does involve residues that are in the amino acid stretch partially occluded and that immediately follow the two conserved residues in the pocket (residues 702 to 707 - Figure 13). Consistent with that, combined mutations of the large apolar residues (I705A, V706A and F707A) present in the occluded stretch resulted in a lower binding affinity (K_D ~41 μM) (Figure 14b). These values are most likely an underestimation, as in these experiments we could not reach the high protein concentrations necessary for saturation (≥ 60 μM, Figure 15b). Mutations of the positively charged residues in a slightly longer stretch, residues 702 to 709, also showed a contribution to the interaction, although to a lesser extent (K_D ~28 μM for R702N, R704N, R708N and K709N - Figure 14b).

Second, we showed that calmodulin binding to the domain has a direct effect on the domain structure. For this we made use of the 7 cysteines in the CNB-homology domain, while both the C-terminal tail (including the calmodulin binding site BDC1) and calmodulin have none. We monitored changes in cysteine accessibility due to WT-calmodulin binding with maleimide-PEG5000, which reacts with free-thiol groups and adds ≥10 kDa to the apparent mass of a protein for each modified cysteine (Lu & Deutsch 2001). We reasoned that if calmodulin binding alters the structure of the CNB-homology domain we would expect to observe changes in the accessibility of the cysteines and therefore changes in the rate of cysteine reaction with the reagent. Western blot analysis of a reaction time course clearly shows differences in the pattern of bands consistent with changes in cysteine accessibility resulting from calmodulin binding (Figure 17d); in the sample with saturating amounts of calmodulin the larger molecular weight bands show up at earlier time points.

Taken together these two approaches demonstrate that 1) calmodulin binding to the CNB-homology domain occurs very close to the body of the domain, involving residues in the stretch immediately after the two residues that are essential for stabilizing the self-

liganded state (Y699/L701), and 2) calmodulin binding results in conformational and/or dynamical changes in the structure of the domain.

Our biochemical and structural experiments show that *in vitro* destabilization of the self-liganded conformation, through mutations of residues involved in contacts between the C-terminal tail and the rest of the domain, results in an increase on the apparent affinity of calmodulin binding to BDC1. Crucially, they also show that calmodulin binding to the domain is dependent on residues that are on the occluded stretch of the BDC1 site. A simple consideration of the molecular bulk of calmodulin suggests that this most likely involves the release of the C-terminal tail from the CNB-homology domain pocket. Consistent with this we show that binding of calmodulin results in structural changes in the body of the domain. Overall, our biochemical characterization suggests the existence of an unliganded conformation in the CNB-homology domain, a structural counter-part to the self-liganded conformation observed in the domain crystal structure.

Functional analysis

The CNB domains of CNG and HCN channels are involved in regulation of channel activation. It is therefore reasonable to ask if the CNB-homology domain also has a similar role in KCNH channels. Our collaborators Dr. Nirakar Sahoo and Dr. Roland Schönherr at the Jena University Hospital, Jena, Germany performed electrophysiological recordings on the human EAG1 channel expressed in *Xenopus* oocytes to explore the role of the CNB-homology domain and the intrinsic ligand on channel function. The amino acid sequence of the sequence stretch spanning the CNB-homology domain and the two C-terminal calmodulin binding sites is identical in the mouse and the human EAG1 channels however, the human channel has been better functionally characterized (Schönherr et al. 2000; Ziechner et al. 2006).

Strikingly, whole cell two-electrode measurements showed that the destabilization of the self-liganded conformation by mutagenesis is reflected in the gating properties of the channel. Currents elicited at different voltages from wild-type and C-terminal tail mutant channels are shown in Figure 18a. It is immediately apparent that the double mutation Y672A/L674A, equivalent to Y699A/L701A in the mouse EAG1, has effects on channel gating. The rise time to reach 80% current amplitude at +50 mV is longer (251.5 ± 26.8 ms (n=15)) for this double mutants than for the WT channel (31.9 ± 3.9 ms (n=17)). From these currents we also extracted $V_{1/2}$ of activation (Figure 18b and 18c), and the respective slope factor (Figure 18d). While the slope factors of the activation dependence on voltage were unchanged, the $V_{1/2}$ values for activation were different: -16 mV for the WT channel, 0 mV for the single mutant L670A (equivalent to L697A in mEAG1), -24 mV

and -23 mV, respectively for the mutants Y672A and L674A (equivalent to Y699A and L701 in mEAG1). The double mutants revealed drastic differences in their effect; the $V_{1/2}$ value for L670A/Y672A mutant was right shifted to ~2mV, while the Y672A/L674A mutant is left shifted to -34 mV. The results for the double mutants are surprising since our biochemical experiments with the isolated domain showed that both sets display similar biochemical properties, involving the release of the C-terminal tail. However, in the channel the double mutants have opposite effects to each other: L670A/Y672A stabilized the closed state over the open, while Y672A/L674A caused a stabilization of the open state over the closed.

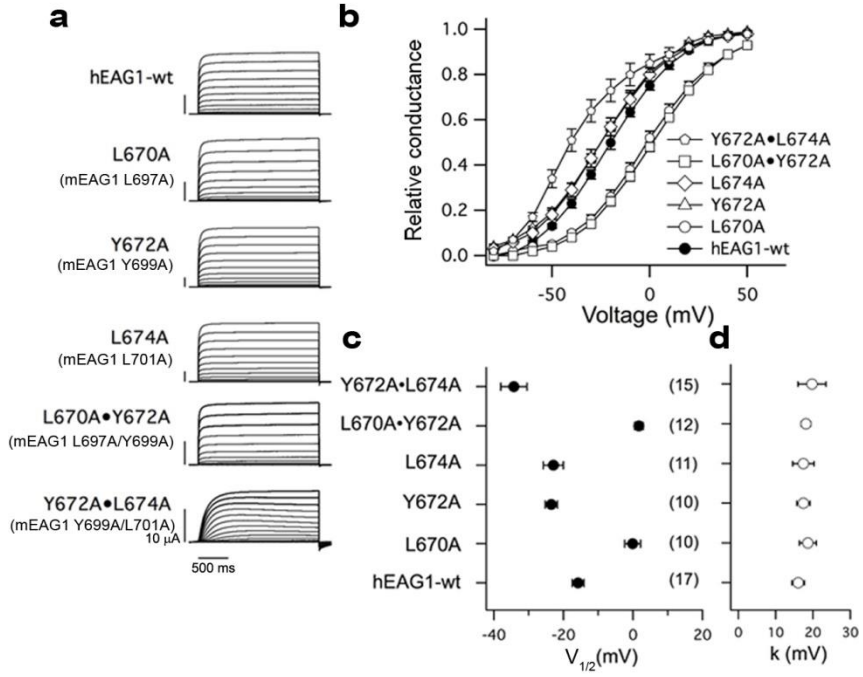

Figure 18 - Functional experiments. a) Two-electrode voltage-clamp current traces of human EAG1 (hEAG1) and indicated mutants expressed in *Xenopus* oocytes. Residue numbering of mutations in human channel and numbering for equivalent residues in the mouse channel (in parenthesis) are indicated. Currents were elicited by 2 s depolarizing pulses from a holding voltage of -90 mV in 10 mV increments between –80 mV and +50 mV. b) Plot of relative conductance as a function of voltage for WT hEAG1 and the indicated mutants c) Plot of $V_{1/2}$ of activation for WT hEAG1 (-15.8 ± 1.7 mV) and mutants (L670A, -0.1 ± 2.3 mV; Y672A, -23.5 ± 1.8 mV; L674A, -22.9 ± 2.9 mV; L670A•Y672A, 1.7 ± 1.3 mV; Y672A•L674A, -34.3 ± 3.8 mV). d) Plot of values for slope factors corresponding to the $V_{1/2}$ data in c) (WT, 16.0 ± 0.4 mV; L670A, 18.6 ± 0.7 mV; Y672A, 17.4 ± 0.7 mV; L674A, 17.4 ± 0.9 mV; L670A•Y672A, 18.1 ± 0.6 mV; Y672A•L674A, 19.7 ± 1.9 mV).

We also evaluated if channel inhibition by calmodulin is altered in the double mutants. Measurements with excised-patches exposed to Ca^{2+}-calmodulin revealed no changes in the sensitivity to Ca^{2+}-calmodulin (Figure 19); inhibition levels as well as on- and off-rates of calmodulin binding were indistinguishable from wild-type channels. The same experiments were not possible with the other double-mutant (Y672A/L674A, equivalent to the mouse Y699A/L701A) due to low expression levels. The lack of effect on inhibition by the mutations that increase *in vitro* calmodulin affinity for BDC1 may be a reflection of the low importance of this site in the inhibition mechanism. Alternatively, it could be that the relatively small increase (10- to 20-fold) in calmodulin apparent affinity, measured by us with the isolated domain, is difficult to detect in an inhibition process that has a half-maximal inhibition concentration (IC_{50}) of 6 nM for calmodulin (Sahoo et al. 2010) and 100 nM for Ca^{2+} (Schönherr et al. 2000).

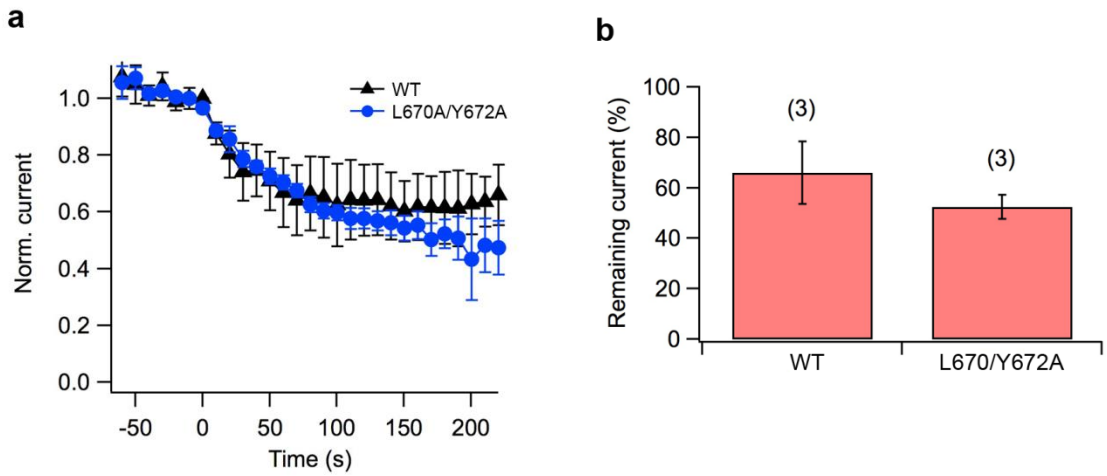

Figure 19 - Ca^{2+}/calmodulin inhibition of human EAG1 channel. a) At time 0 excised patches expressing hEAG1 channel were exposed to a solution containing 500 nM calmodulin and 250 nM Ca^{2+}. Reduction in current elicited from wildtype channel (black triangles) and mutant L670A/Y672A (blue circles). b) Remaining current after exposure, average from 3 experiments.

Crystallization trials of CNB-homology domain/CaM complexes

Incubation of wild type CNB-homology domain containing BDC1 (mEAG1 552-724) with Ca^{2+}-calmodulin in concentrations that should result in ~90% saturation, according to the determined K_D, did not result in a shift in size-exclusion chromatography profile that would suggest complex formation. Additionally, no crystals could be obtained with a 1:1 molar ratio of CNB-homology domain and calmodulin, probably due to the transient nature of this interaction.

In contrast, C-terminal tail double mutant L697A/Y699A CNBhD (that has a slightly higher affinity for calmodulin) mixed with an equimolar amount of calmodulin is eluted in size-exclusion chromatography as a species of higher molecular weight than either CNB-homology domain or calmodulin alone (Figure 20). The peak is not symmetric though, which can be due to the weak binding affinity (K_D ~ 2 µM) of the complex. Fractions 2, 3 and 4 (that contained both proteins on SDS-PAGE analysis, Figure 20) were pooled for crystallization trials, to get as much calmodulin into complex formation as possible, but no crystals were obtained. Shorter CNB-homology domain mutants ending in residue 715 and 718 also showed the same size-exclusion chromatography profile when incubated with calmodulin but once again no crystals were obtained.

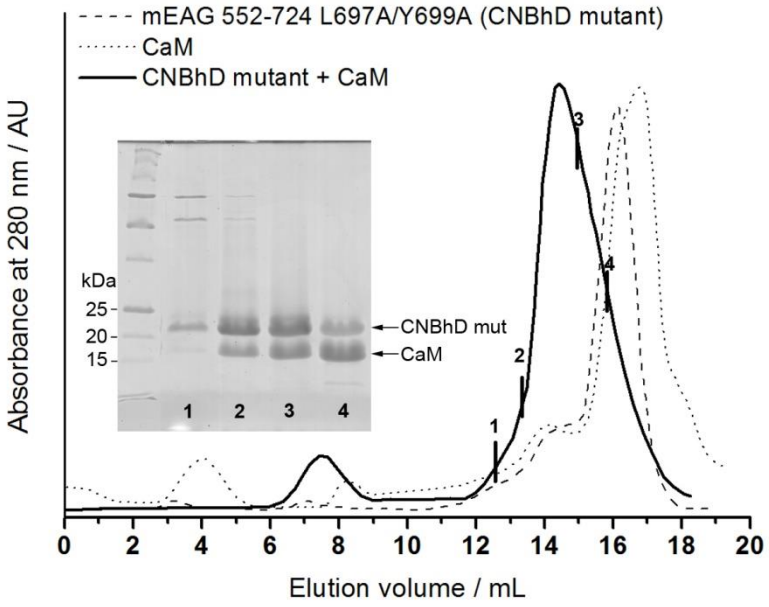

Figure 20 - Superposition of size-exclusion chromatography traces of mEAG 552-724 L697A/Y699A (dashed line), calmodulin (dotted line) and equimolar amounts of mEAG 552-724 L697A/Y699A and calmodulin (continuous line). Inset: 17% SDS-PAGE of fractions labeled 1 to 4 in the size-exclusion chromatography trace. Fractions 2 to 4 were pooled for crystallization trials.

DISCUSSION

The CNB-homology domain from KCNH channels has raised a lot of interest. These domains have high sequence similarity with the CNB domains in CNG and HCN channels, however, KCNH channel function is not affected by cyclic nucleotide exposure (Brelidze et al. 2009). A comparison of the structures of the CNB-homology domain from KCNH

channels with structures of CNB domains clearly shows that these KCNH channel domains share many of the structural features present in CNB domains. The comparison also reveals crucial sequence and structural differences in the pocket of the CNB-homology domain relative to CNB domains which provide an explanation for the very low affinity of CNB-homology domain for cyclic nucleotides.

Importantly, our structure shows that the C-terminal tail of the domain extends over its surface and that two well-conserved residues (Y699 and L701, the “intrinsic ligand”) in the tail occupy the same space that cyclic nucleotides inhabit in CNB domains. This self-liganded conformation is also present in the recently determined structures of the CNB-homology domains of the other two channel subfamilies ELK and ERG (Brelidze et al. 2012; Brelidze et al. 2013), strongly suggesting that it is a conserved feature of these KCNH channel domains. The C-terminal tail of the mEAG1 CNB-homology domain structure also includes a partially occluded stretch of a previously described calmodulin binding site (CaM BDC1) that does not exist in the remaining KCNH channel subfamilies (Ziechner et al. 2006).

By characterizing the CNB-homology domain conformation as self-liganded it becomes implicit that there is also an unliganded state. A central aspect of this work is that we have provided biochemical evidence that supports the existence of an unliganded conformation, where the C-terminal tail peels away from the domain. For this we made use of the affinity of calmodulin to the partially occluded binding site at the end of the C-terminal tail. Indeed we established that CaM BDC1 is a weak binding site for calmodulin and we demonstrated that mutagenesis of the residues that in the domain structure appear to hold the C-terminal tail in position result in an increase in the calmodulin apparent affinity, consistent with a release of the tail and increased exposure of the calmodulin binding site. In addition, we showed that the calmodulin interaction involves mostly the N-lobe and it extends to residues in the occluded stretch of the CaM BDC1 since, mutation of some of these residues decreased calmodulin affinity. These residues are immediately after Y699 and L701 and the molecular volume of calmodulin requires a peeling away of the C-terminal tail so that the interaction can occur. Consistent with this interpretation we showed also that calmodulin binding causes a structural change in the CNB-homology domain as reflected in changes in cysteine accessibility. Interestingly, the sequence and structural parallels between CNB-homology domain and CNB domains lead naturally to a conclusion that the tail movement is reminiscent of the repositioning of the C-helix away from the ligand-binding pocket which occurs in CNB domains upon release of cyclic nucleotide (Rehmann et al. 2007; Clayton et al. 2004; Sharma et al. 2009).

Our functional analysis suggests that the CNB-homology domain has a role in channel gating since mutations that destabilize the self-liganded conformation by releasing the C-terminal tail also affect the voltage dependence of activation. Strikingly, these functional effects are not what would be expected from the parallel between the release of the C-terminal tail in the CNB-homology domain and the movement of the C-helix away from its bound-state position that occurs in CNB domains upon release of cyclic nucleotide. In CNG and HCN channels this CNB domain conformational change favors closure of the channel gate (Craven & Zagotta 2006; Kaupp & Seifert 2002). In the human EAG1 channel the two double-mutants, both of which lead to the release the C-terminal tail, have very different effects, stabilizing either the open or the closed states of the channel. This contrasting result indicates that in the full-length channel the intrinsic ligand residues have as yet unidentified individual roles besides the shared function of holding the C-terminal tail in its position. This outcome reveals that despite the sequence, structural and even biochemical similarities the role of CNB-homology domain in gating of KCNH channels is not identical to the role of CNB domains in HCN and CNG channels.

IV. CHARACTERIZATION OF THE INTERACTION OF CALMODULIN WITH THE EAG1 K^+ CHANNEL CYTOPLASMIC REGIONS

The work described in this chapter is in preparation to be submitted for publication.

INTRODUCTION

The molecular mechanism of EAG1 channel inhibition by Ca^{2+}-CaM is unknown. Three CaM binding sequences (BDN, BDC1 and BDC2) were identified in a peptide array screen spanning the entire EAG1 cytoplasmic regions. All three sites appear to be functionally important for CaM inhibition of these channels, since channels with mutations in any of these sites show severely diminished CaM sensitivity (Schönherr et al. 2000; Ziechner et al. 2006). The affinities of CaM for these sites were determined using fluorescence correlation spectroscopy. However, this technique relies on a large difference between the mass of the isolated labeled protein and of the complex formed. In this case this size ratio is low, raising doubts about the accuracy of the measurements. In particular, variation in the K_Ds determined for CaM BDC1 were observed, that depended on the used fluorophore and on whether CaM or the channel fragment were labeled (Ziechner et al. 2006).

In this chapter, we revisited the binding properties of CaM to BDN, BDC1 and BDC2 using isothermal titration calorimetry (ITC). ITC is a label-free technique which provides thermodynamic parameters and gives insights into the nature of the non-covalent interactions involved in binding. The contribution of the CaM lobes to the interaction with the EAG1 sites was also evaluated by using isolated lobes or full-length CaM with mutations in the EF-hands. We also assessed the impact of the PAS and CNB-homology domains on the binding of CaM to BDN, BDC1 and BDC2. Finally, we used X-ray crystallography to obtain a structure of CaM in complex with BDC2.

METHODS

Expression and purification of the maltose binding protein fusions with mEAG1 CaM BDs

Different versions of the calmodulin binding sequences BDN, BDC1 and BDC2 were cloned into the plasmid vector pRSF Duet1 (Novagen) as C-terminal fusions of maltose binding protein (MBP). These sequences included the amino acid stretches previously identified by (Ziechner et al. 2006), underlined in table 2. MBP contains an N-terminal hexa-histidine tag for purification by Immobilized-metal affinity chromatography (IMAC) and a TEV protease recognition sequence on the C-terminal, before the CaM binding sequences.

Table 2 – Amino acid sequences of the short and long versions of the CaM binding sites BDN, BDC1 and BDC2

Short BDN (mEAG1 145-168)	CKGWGKFARLTRALTSSRGVLQQL
Long BDN (mEAG1 138-174)	*QPIEDDS*CKGWGKFARLTRALTSSRGVLQQL*APSVQK*
Short BDC1 (mEAG1 696-718)	ILTYNLRKRIVFRKISDVKREE
Long BDC1 (mEAG1 690-724)	*SFSRNL*ILTYNLRKRIVFRKISDVKREE*EERMKRK*
Short BDC2 (mEAG1 733-757)	PDHPVRRLFQRFRQQKEARLAAERG
Long BDC2 (mEAG1 727-764)	*APLILP*PDHPVRRLFQRFRQQKEARLAAERG*GRDLDDL*

Escherichia coli BL21 (DE3) competent cells transformed with an expression vector were grown in Luria broth medium supplemented with kanamycin (50 mg/L) at 37 ºC with agitation until the 600 nm optical density reached 0.6–0.8. At this point, IPTG was added to a final concentration of 0.5 mM for overnight induction at 18 ºC (12–16 h). Cultures were harvested by centrifugation at 4785xg for 20 min at 4 ºC and the resulting pellet was resuspended in buffer A (1 L pellet in 20 mL 50 mM HEPES pH 7.5, 250 mM KCl) supplemented with protease inhibitors: 1 mM PMSF, 1 mg/mL leupeptin, 1 mg/mL pepstatin. Cell lysis was performed in a cooled cell cracker (Emulsiflex-C5, Avestin) and the lysate was centrifuged at 32 800xg for 45 min at 4 ºC to remove cell debris. The supernatant was loaded onto His-select Nickel Affinity Gel (Sigma) pre-equilibrated with buffer A and washed with buffer A until the 280 nm optical density (OD280) stabilized. While monitoring the OD280 of the eluate, the beads were washed with buffer A with extra KCl (500 mM). Most of the fusion protein was eluted from the resin with buffer A containing 20 mM imidazole. The remaining His-tagged protein was eluted with buffer A containing 250 mM imidazole.

The protein fraction eluted with 20 mM imidazole was dialyzed against buffer B containing 50 mM HEPES pH 7.5, 150 mM NaCl, 2 mM $CaCl_2$ and 1 mM TCEP and loaded onto an S200 size-exclusion chromatography column (GE Healthcare), pre-equilibrated with the same buffer.

Expression and purification of PAS and CNB-homology domain constructs containing CaM binding sites

Some of the constructs containing CaM binding sites suffer proteolysis during expression in bacteria. To overcome this problem, these constructs were cloned into multiple cloning site (MCS) 1 of co-expression vector pRSFDuet-1 (Novagen) with a N-terminal His_6-tag and CaM was cloned into MCS2 of the same vector without any affinity tag. By co-expressing both proteins, CaM will bind to these CaM binding sequences shielding them from proteases.

Expression and IMAC purification was done as described in (Marques-Carvalho et al. 2012), except that the buffering agent was 50 mM HEPES pH 7.5 instead of Tris-HCl. Despite purifying in calcium-less buffer, CaM still came attached to the eluted protein. The eluted protein was dialyzed against buffer containing 1 mM EDTA to disrupt the complex. Taking advantage of the large difference in isoelectric point (pI) between acidic CaM (pI_{CaM}=4) and the basic PAS and CNB-homology domain constructs (pI~9), a step of anion exchange chromatography was added. The dialysed protein was loaded onto a 5 mL Hitrap Q HP (GE Healthcare) equilibrated with 50 mM HEPES pH 7.5, 150 mM NaCl, 5 mM DTT (buffer A). Monitoring OD280, the mEAG1 enriched flow-through was collected, and a gradient to 100% buffer B (50 mM HEPES pH 7.5, 1 M NaCl) was performed, with CaM being eluted between 35-45% B.

Coupling of calmodulin to HiTrap NHS-Activated HP – "CaMTrap" column

HiTrap NHS-Activated HP 5 mL (GE Healthcare) was derivatized with CaM as described in the manual. Briefly, the column was washed with 1 mM ice-cold HCl immediately before ligand coupling. A solution containing 750 µmol of CaM in 0.2 M $NaHCO_3$ pH 8.5, 0.5 M NaCl (coupling buffer) was injected onto the column and left incubating at room temperature for 1h. The unbound protein was washed with of coupling buffer. Coupling efficiency was estimated to be around 75%, with ~500 µmol of CaM coupled to the 5 mL column ("CaMTrap"). This CaMTrap column was stored at 4ºC in 50 mM HEPES pH 7.5, 150 mM NaCl, 2 mM $CaCl_2$ (calcium binding buffer) supplemented with 0.05%(w/v) of the preservative azide.

Purification of channel fragments with CaMTrap

The CaMtrap column was used as an extra purification step whenever a channel fragment containing a CaM binding site showed proteolysis or other contaminants. A maximum of 500 µmol of partially purified protein was loaded into CaMTrap equilibrated in calcium binding buffer (50 mM HEPES pH 7.5, 150 mM NaCl, 2 mM $CaCl_2$). Monitoring the OD280, the CaMTrap was washed with calcium binding buffer and the CaM binding site-containing protein was eluted with 50 mM HEPES pH 7.5, 150 mM NaCl, 2 mM EDTA, followed by a more stringent elution with 50 mM HEPES pH 7.5, 500 mM NaCl, 2 mM EDTA.

Expression and purification of the MBP fusions with CaM N- and C-lobe

CaM lobes were cloned as His_6-tagged MBP fusions and purified as described for the other MBP fusions. Briefly, cleared bacterial lysate was loaded into a Nickel column. TEV protease was added to the eluted protein to cleave the MBP from the CaM lobes and dialysed overnight against buffer containing 50 mM HEPES pH 7.5, 150 mM NaCl, 2 mM $CaCl_2$, 1 mM TCEP. After cleavage, the protein solution was further purified using another round of IMAC to bind the TEV protease and MBP and the flow-through containing the lobe was kept. This flow-through was then loaded into an affinity column MBPtrap (GE Healthcare) to remove any MBP contaminants. The flow-through containing the CaM lobes was run on a size-exclusion column in 50 mM HEPES pH 7.5, 150 mM NaCl, 5 mM $CaCl_2$.

Isothermal Titration Calorimetry

Purified CaM (or its individual lobes) and channel constructs spanning CaM the binding sequences were dialyzed overnight against 50 mM HEPES pH 7.5, 150 mM NaCl, 1 mM TCEP-HCl containing 5 mM $CaCl_2$ (or 5 mM EDTA). CaM and the channel fragments were extensively dialysed in the same beaker to avoid buffer mismatch. CaM concentration was determined by measuring absorbance at 277 nm and the extinction coefficient ε_{277nm}=3029 M^{-1} cm^{-1} (Strasburg et al. 1988). Channel fragment concentration was determined by measuring absorbance at 280 nm using the calculated extinction coefficients from the ExPASy tool Protparam. In general, the channel fragment was placed in the sample cell and CaM (or lobe) was placed in the syringe at least 10-times more concentrated than the protein in the cell. CaM was degassed for 5 min before the experiment using the Thermovac. Isothermal titration calorimetry (ITC) was carried out using the VP-ITC instrument (MicroCal) at 25 ºC (unless mentioned otherwise), with a first injection of 2 µL, followed by 28x10 µL injections. Data were analyzed using Origin 7 (MicroCal) or

AFFINImeter. For each titration, the first 2-µl injection was ignored and correction for the heat of dilution was made by subtracting the average of the last four injection areas to all injection points. Fitting was done with the appropriate binding model which provided values for stoichiometry (N), association constant (K_A), enthalpy (ΔH) and entropy (ΔS) of binding. The obtained K_A was converted to K_D.

Complex purification

To crystallize the complexes of CaM with peptides, mEAG1 CaM binding sequences were cloned into multiple cloning site (MCS) 1 of co-expression vector pRSFDuet-1 (Novagen) as a His_6-tagged maltose binding protein fusion (cleavable with TEV protease) and CaM was cloned into MCS2 of the same vector without any affinity tag. This approach had the objective of forming the complex of CaM with the peptides before cleaving off the MBP, to ensure that the peptide remained soluble throughout the purification.

In brief, protein expression and IMAC purification was similar to the other MBP-fusions, except it was done in the presence of 5 mM $CaCl_2$, to maintain the CaM-peptide complex. After elution from IMAC, protein was quantified and a 1:10 mass ratio of TEV protease to MBP fusion was added to cleave the MBP overnight while dialyzing out the imidazole. On the following day two extra steps of purification allowed to separate the CaM-peptide complex from the MBP and TEV protease. A first step of IMAC served to bind most MBP and TEV protease, which are both His_6-tagged. The flow-through (FT) that contained the CaM-peptide complex was then loaded onto an affinity column MBPtrap (GE Healthcare) to get rid of any remaining MBP. Once again, the FT was kept and the protein complex was run on a S200 size-exclusion column (GE Healthcare) in buffer with 20 mM HEPES pH 7.5, 150 mM NaCl, 1 mM $CaCl_2$, 1 mM TCEP to make sure that CaM stayed calcified at the high protein concentrations needed to set drops.

Crystallization, data collection and refinement

Crystals were grown at 20 °C using sitting-drop vapour diffusion by mixing a 1:1 (v/v) ratio of protein mixture and a reservoir solution containing 0.2 M di-ammonium citrate pH 5, 20% PEG 3350. A dataset was collected at the Proxima 2A beamline of the Soleil Synchrotron to 2.85 Å resolution. Data was integrated using the program XDS (Kabsch 2010) and scaled using Aimless (Evans & Murshudov 2013), from the CCP4 program suite (Winn et al. 2011). The structure was solved by molecular replacement with Phaser (McCoy et al. 2007) using several ensembles of calmodulin N- and C-lobes as search models (PDB codes: 1CFD, 1CLL, 2BE6, 3DVM, 3OXQ chain A, 3OXQ chain B, 4DJC and 4GOW). Model refinement was done in PHENIX (Adams et al. 2010); TLS refinement

was applied (Painter & Merritt 2006). Model building was performed in Coot (Emsley & CoWTan 2004) and figures were created using PyMOL (DeLano 2002).

Fluorescence anisotropy

PAS domain (mEAG1 1-137) was cloned into a pET15b vector with Ampicillin resistance, and the expression and purified protocol was performed as described in the first chapter. Fluorescein labelling of the endogenous cysteines of the PAS domain (F-PAS) was done as described previously (Taraska et al. 2009).

Briefly, PAS was incubated 1 mM TCEP for 1h at 4 °C to reduce the cysteines. It was passed through a desalting column equilibrated with 20 mM Tris HCl pH 8.0, 150 mM NaCl to remove the TCEP and incubated with fluorescein-5-maleimide (Molecular Probes) at molar ratios 1:5 and 1:10 for 1h at room temperature protected from light. After 1h the reaction was stopped with 5 mM DTT and the free dye was dialysed out with 20 mM Tris HCl pH 8.0, 150 mM NaCl, 5 mM DTT using a 3.5 kDa cutoff dialysis membrane.

F-PAS at 100 nM was incubated with different concentrations of CNB-homology domain in the dialysis buffer described above for at least 20 min. Fluorescence anisotropy measurements done at 25 °C using a Horiba Fluoromax-4 spectrofluorimeter using an excitation wavelength of 492 nm and emission of 514 nm, with slit widths of 1 or 2 nm.

To estimate binding affinity, plots of the anisotropy versus total CNB-homology domain concentration were fit considering a first-order reaction:

$$\text{Anisotropy} = \alpha \left[\frac{(Rt+KD+Lt)-\sqrt{(-Rt-KD-Lt)^2-4\times Rt\times Lt}}{2}\right] + \beta$$

in which R, L and RL are concentrations of the free receptor, free ligand, and receptor–ligand complex, respectively, Rt and Lt are total receptor and total ligand concentrations, respectively, K_D is the ligand-binding affinity, and α and β are a scaling factor and an offset factor, respectively (Haitin et al. 2013b).

RESULTS

Characterization of CaM binding to EAG1 CaM binding domains

CaM BDC1 and CNBhD-BDC1 – importance of BDC1

Mutations in CaM BDC1 severely compromised the effect of CaM in EAG1 currents (Ziechner et al. 2006). However, the importance of CaM BDC1 in EAG1 channel inhibition by CaM is not well established since: 1) this sequence displayed lower affinity for CaM than the remaining CaM binding sites (Ziechner et al. 2006); 2) a FRET study showed that no CaM binding was detected to the EAG1 channel if CaM binding sites BDN and BDC2 were mutated (Gonçalves & Stühmer 2010); 3) BDC1 is partially occluded due to the self-liganded conformation of CNBhD-BDC1 and the K_D for CaM is only 12 µM (Marques-Carvalho et al. 2012), which is rather modest in the context of a process with an IC_{50} of 6 nM (Sahoo et al. 2010).

We set out to dissect the CaM binding properties of BDC1 using isothermal titration calorimetry (ITC). To study the interaction of CaM with this region we generated two different channel fragments: a 35 aminoacid stretch centered on BDC1 fused to MBP and another which includes the whole CNB-homology domain and BDC1 (the same construct used in chapter one), Table 3.

Titration of Ca^{2+}-CaM into BDC1 peptide (mEAG1 690-724) reveals an endothermic process (ΔH = 2.24 ± 0.03 kcal/mol) with a K_D of 143 ± 9 nM (Figure 21a). We also tested the effect of the CNB-homology domain on the CaM interaction with BDC1. Titration of Ca^{2+}-CaM into CNBhD-BDC1 (mEAG1 552-724) is also endothermic (ΔH = 1.74 ± 0.34 kcal/mol) but with lower affinity (K_D of 6.5 ± 0.8 µM) (Figure 21b). This K_D agrees with the 12 µM that had been obtained with fluorescently labelled CaM (Marques-Carvalho et al. 2012). Both interactions are entropically driven with a ΔS ~ 39 cal/mol/deg for BDC1 and ΔS ~ 30 cal/mol/deg for CNBhD-BDC1. This is indicative of water molecules being released from the complex surface or of an increase in the protein conformational freedom upon complex formation. The difference in K_D fits well with the observation that BDC1 is partially occluded in the structures of the CNB-homology domains (Marques Carvalho et al. 2012; Haitin et al. 2013a), resulting in low affinity towards CaM.

Table 3 - Thermodynamic parameters for titration of Ca^{2+}-CaM into protein fragments containing BDC1.

CaM BD	Cell	N	K_D (nM)	ΔH (kcal mol^{-1})	ΔS (cal mol^{-1} deg^{-1})	n
	MBP-BDC1	0.86 ± 0.03	142.8 ± 8.8	2.24 ± 0.03	38.9 ± 0.2	3
	CNBhD-BDC1	0.80 ± 0.03	$6.5x10^3$ ± $0.8x10^3$	1.74 ± 0.34	29.7 ± 1.2	3

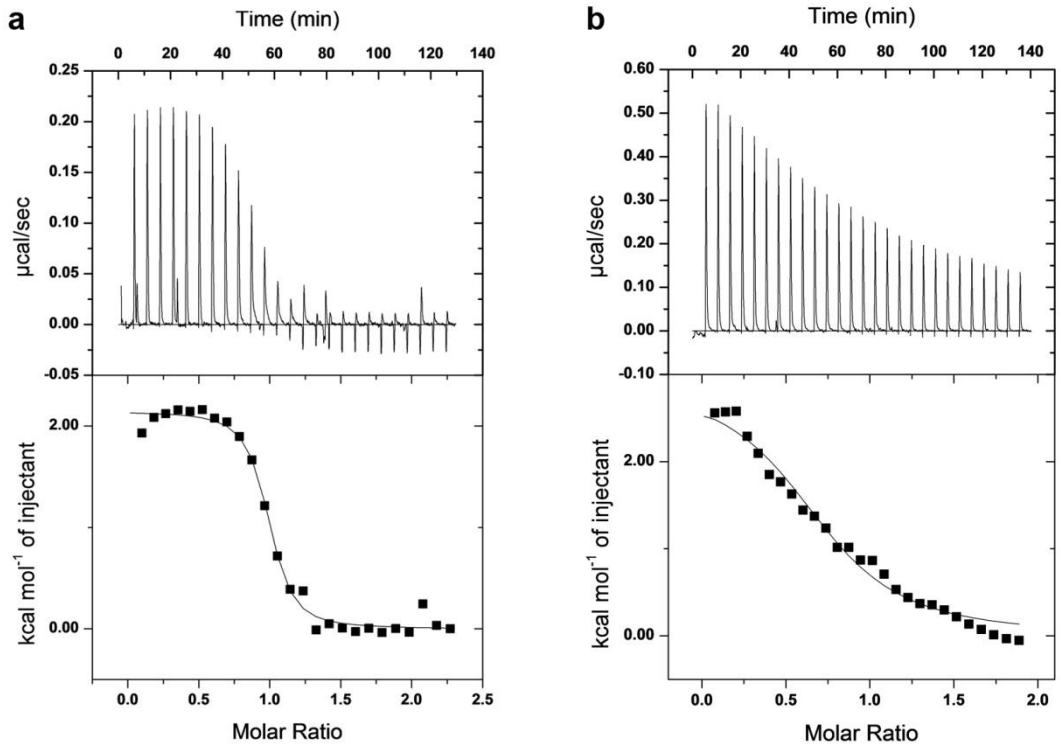

Figure 21 – a) Example of an ITC titration of 250 µM Ca^{2+}-CaM into 25 µM MBP- BDC1. b) Example of an ITC titration of 500 µM Ca^{2+}-CaM into 50 µM CNBhD-BDC1. The top panel shows the raw heat evolved after each injection and the bottom panel shows the integrated heats of injection per mole of injectant.

It has been suggested that the BDC1 site is not physiologically important. However, mutations on the BDC1 sequence that lower the affinity for CaM (Marques-Carvalho et al. 2012), have a dramatic effect on EAG1 channel inhibition by Ca^{2+}-CaM (Ziechner et al. 2006). The recent structure of the complex between PAS domain and CNB-homology domain (Haitin et al. 2013b) shows that the post-CNBhD region that comprises BDC1

interacts with the PAS domain (Figure 22). We wondered if mutations on BDC1 destabilize the PAS/CNB-homology domain complex, leading to changes in channel properties.

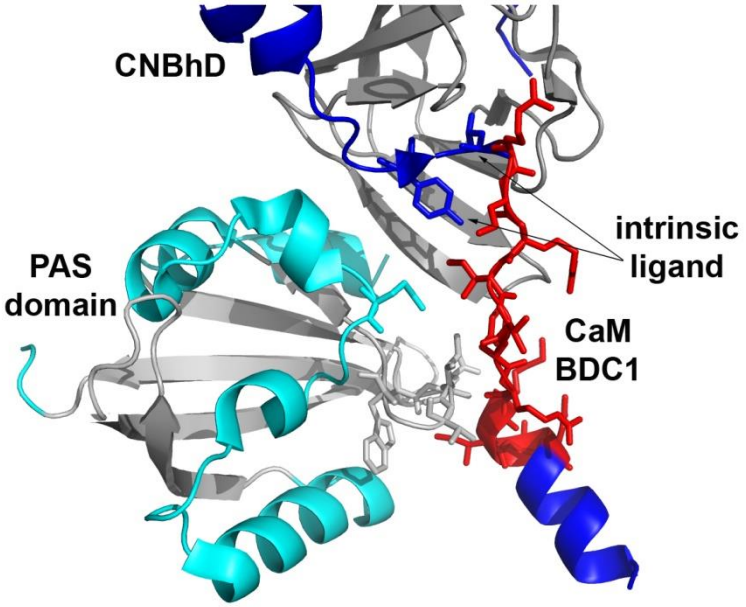

Figure 22 – Interface of the complex between mEAG1 PAS domain (cyan and grey) and CNB-homology domain (CNBhD, blue and grey). The CaM BDC1 region is depicted in red sticks, and PAS domain residues that interact with this protein stretch are also represented in stick model (Haitin et al. 2013b).

We used the fluorescence anisotropy assay described by (Haitin et al. 2013b) to study the effect of BDC1 mutations on the interaction between PAS domain and CNB-homology domain. We obtained a K_D ~ 16 µM, for the interaction of WT CNBhD-BDC1 with PAS domain (Figure 23), similar to the published K_D. Strikingly, the CNBhD-BDC1 mutants R702N/R704N/R708N/K709N and I705A/V706A/F707A do not form a complex with fluorescently-labelled PAS domain, as can be seen by the lack of change in fluorescein-PAS anisotropy on Figure 23. We propose that the functional effect on CaM inhibition of the channels with BDC1 mutations might be caused by a disruption of the gating machinery through the destabilization of the complex between PAS and CNB-homology domain.

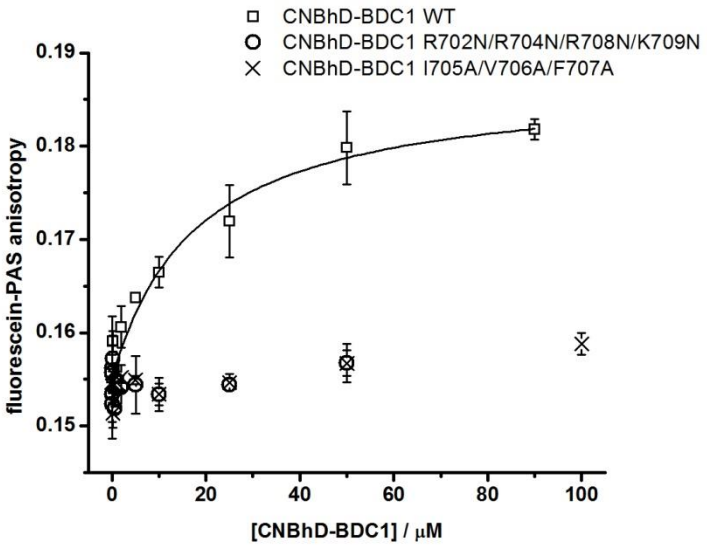

Figure 23 - Fluorescence anisotropy of fluorescein labelled PAS domain titrated with CNBhD-BDC1 WT (squares) and BDC1 mutants R702N/R704N/R708N/K709N (circles) and I705A/V706A/F707A (crosses).

CaM BDN and PAS-BDN

CaM BDN starts less than 20 residues after the PAS domain and previous studies showed a K_D for Ca^{2+}-CaM in the range of 100-200 nM using fluorescence correlation spectroscopy, as well as surface plasmon resonance spectroscopy (Ziechner et al. 2006).

A short version of BDN (mEAG1 145-168) showed several proteolysis products in SDS-PAGE analysis after purification (grey arrows, Figure 24a). This fusion was co-expressed with calmodulin with the intent to form the complex in the bacterial cytoplasm, shielding BDN from proteases. Mass spectrometry analysis confirmed that co-expression decreased C-terminal degradation, although not completely (black arrow on Figure 24a). Thus, we used a CaMtrap column (which has CaM crosslinked to an agarose resin) to separate full-length protein from proteolysis fragments (Figure 24a).

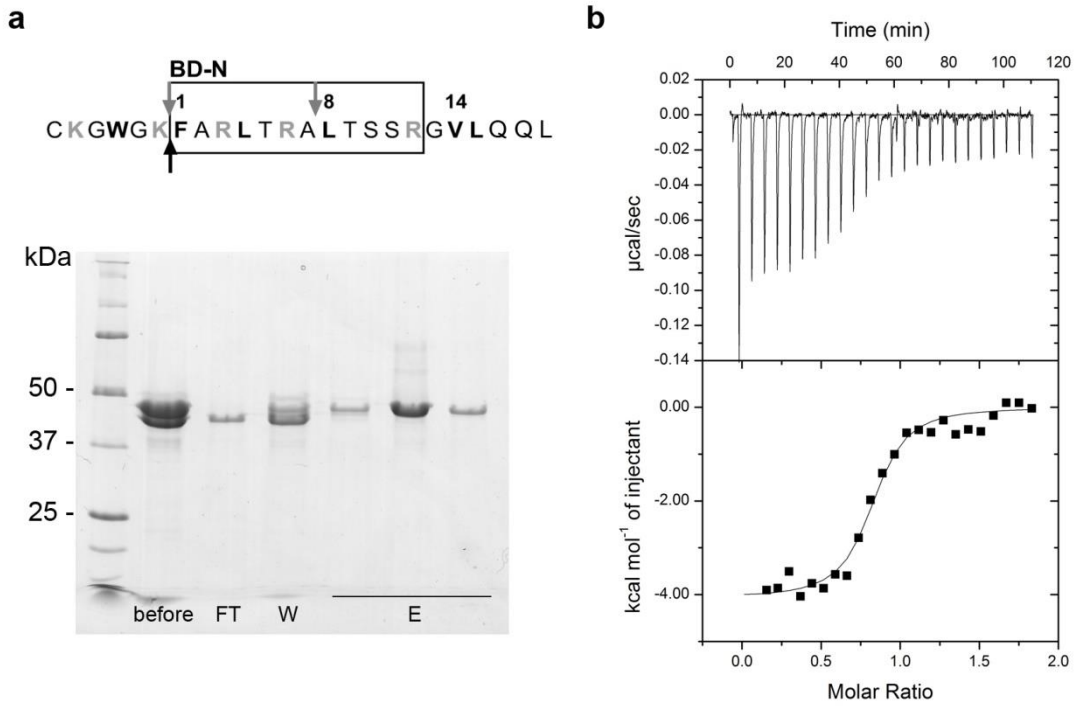

Figure 24 – a) Short BDN sequence with the proteolysis products identified by MALDI-TOF-TOF. Arrows indicate the site of proteolytic cleavage (grey: expression in the absence of CaM; black: co-expressed with CaM) and 15% SDS-PAGE of MBP-short BDN purification with CaM affinity resin (before CaM resin, flow-through (FT), wash (W) and elution (E) with EGTA). b) ITC titration of 60 µM Ca^{2+}-CaM into 6 µM MBP-short BDN.

ITC was used to analyze binding of CaM to this short BDN fragment. It has a K_D of 184 ± 12 nM for Ca^{2+}-CaM (Figure 24b) and an enthalpy of binding of -4.14 ± 0.15 kcal/mol.

A longer version of BDN (mEAG1 138-174) was also created. This channel fragment did not suffer proteolysis and a more detailed characterization was done using this protein. The ITC experiments showed that Ca^{2+}-CaM binds this BDN with an K_D of 18.1 ± 1.1 nM and with a ΔH = -4.92 ± 0.06 kcal/mol (Figure 25a). The ten-fold higher affinity relative to the short BDN is achieved through an increase in the entropy of the system (Table 4). CaM binding to this fragment is Ca^{2+}-dependent, since no binding could be detected with apo-CaM (in the presence of 5 mM EDTA) at 15 or 25 ºC (Figure 25b).

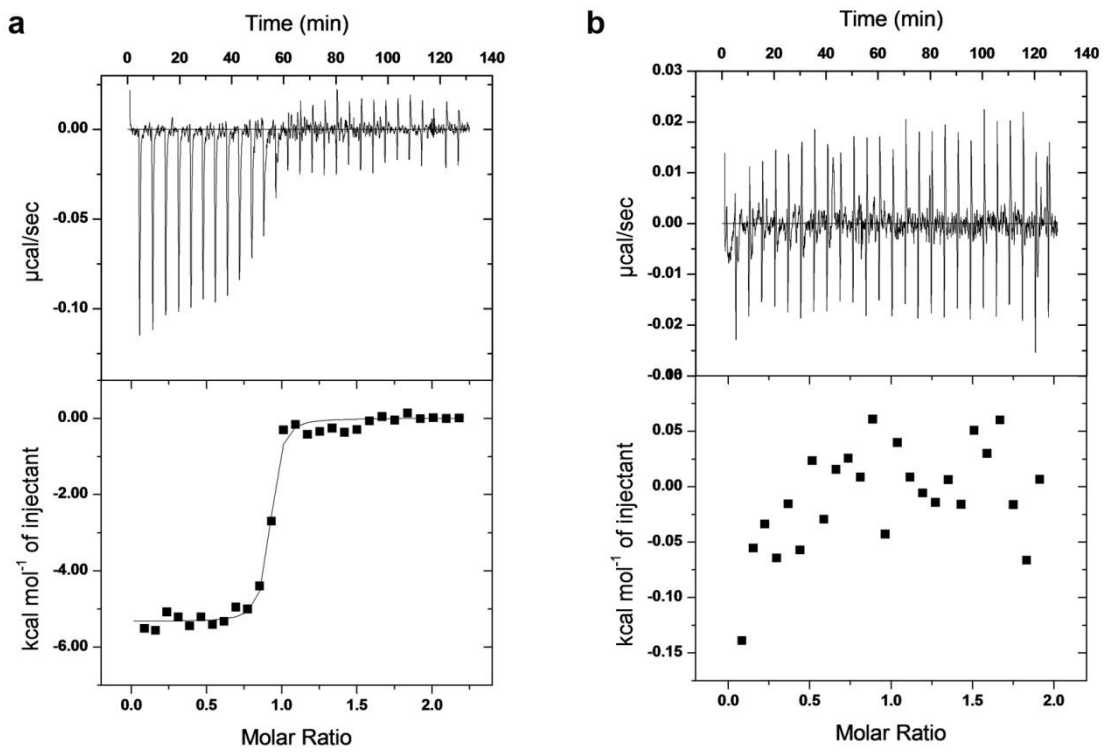

Figure 25 – a) ITC titration of 60 µM Ca^{2+}-CaM into 6 µM MBP-BDN. b) ITC titration of 500 µM apo-CaM into 50 µM MBP-BDN, in the presence of 5 mM EDTA.

In order to get further insights into the CaM binding mode, we investigated the contribution of each lobe of CaM to the interaction with BDN. For this we used CaM's individual lobes lobes and CaM with mutations on the N-lobe EF-hands.

ITC characterization of the binding of the CaM lobes to BDN gave a K_D of 8.9 ± 0.4 µM for Ca^{2+}-N-lobe (ΔH = -9.61 ± 0.76 kcal/mol, Figure 26a) and a K_D of 1.4 ± 0.1 µM for Ca^{2+}-C-lobe (ΔH = -3.34 ± 0.11 kcal/mol, Figure 26b). The 100-fold drop in affinity for the N- and C-lobe suggests that CaM binding to BDN involves both lobes, just like in the canonical binding mode. Titration of full-length CaM with mutations that disrupt binding of calcium to EF-hands 1 and 2 (CaM D21A/D57A = CaM EF12 mut) into BDN gives thermodynamic parameters very similar to C-lobe alone – K_D = 1.4 ± 0.1 µM and ΔH = -2.62 ± 0.03 kcal/mol (Figure 26c), showing that the N-lobe needs to have Ca^{2+} bound in order for CaM to tightly interact with BDN.

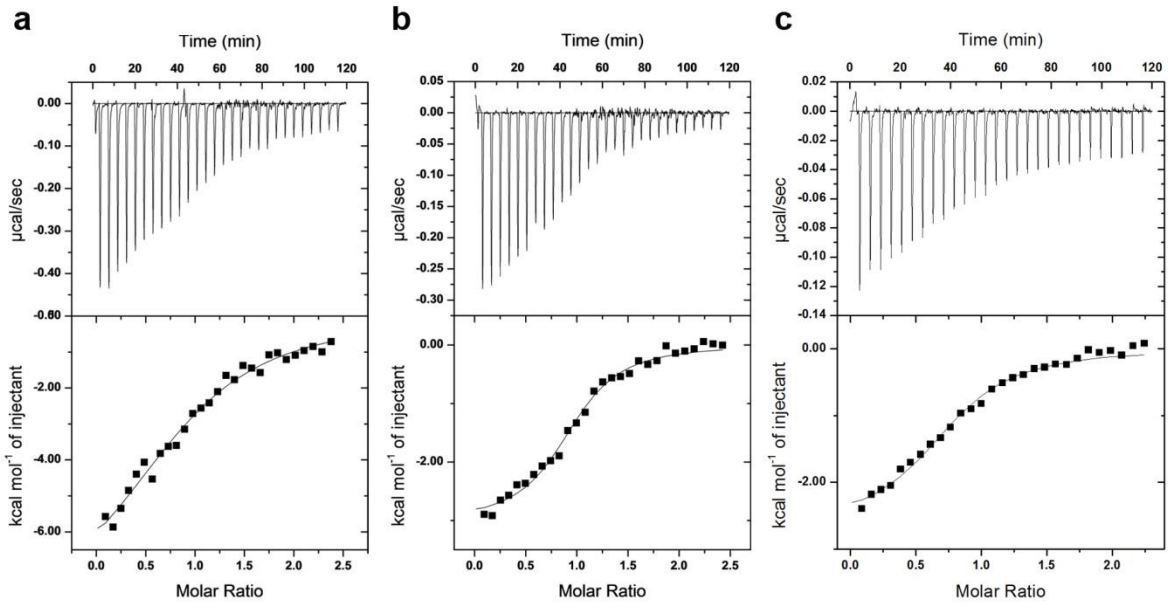

Figure 26 – a) ITC titration of 253 µM Ca^{2+}-N-lobe into 23 µM MBP-long BDN. b) ITC titration of 258 µM Ca^{2+}-C-lobe into 23 µM MBP-long BDN. c) ITC titration of 135 µM Ca^{2+}-CaM EF12 mutant into 13 µM MBP-long BDN.

To determine if the PAS domain influences the binding of CaM to BDN, two protein constructs were designed, encompassing the EAG1 N-terminal regions PAS domain and BDN. The longer construct (CAP-PAS-BDN, mEAG1 6-174) included a stretch of amino acids before the PAS domain that have been shown to have a role in channel function (Terlau et al. 1997) – the PAS CAP. The shorter version (PAS-BDN, mEAG1 28-174) does not include the CAP region.

These constructs suffered C-terminal degradation, even when co-expressed with CaM. For this reason, four purification steps were necessary to obtain full-length protein: IMAC, ion exchange, CaMTrap and size-exclusion chromatography, as described in the methods section.

The interaction of CaM with both PAS domain constructs has similar thermodynamic signatures. CaM binds with a K_D of 162.1 ± 6.5 nM and ΔH = 7.71 ± 0.08 kcal/mol to CAP-PAS-BDN (Figure 27a) and K_D = 105.9 ± 14.9 nM and ΔH = 7.47 ± 0.18 kcal/mol to PAS-BDN (Figure 27b), revealing that the CAP region has no influence on this interaction. The CaM affinities for both PAS-BDN constructs are almost 10-fold lower than for the BDN peptide, indicating that the globular domain affects CaM binding to BDN. The more negative enthalpy is indicative of an increase in the bonding network with the PAS-BDN fragments. However, this is accompanied by an increased order of the system (lower

entropy change) which results in a lower affinity. We speculate that CaM might be establishing interactions with the surface of the PAS domain.

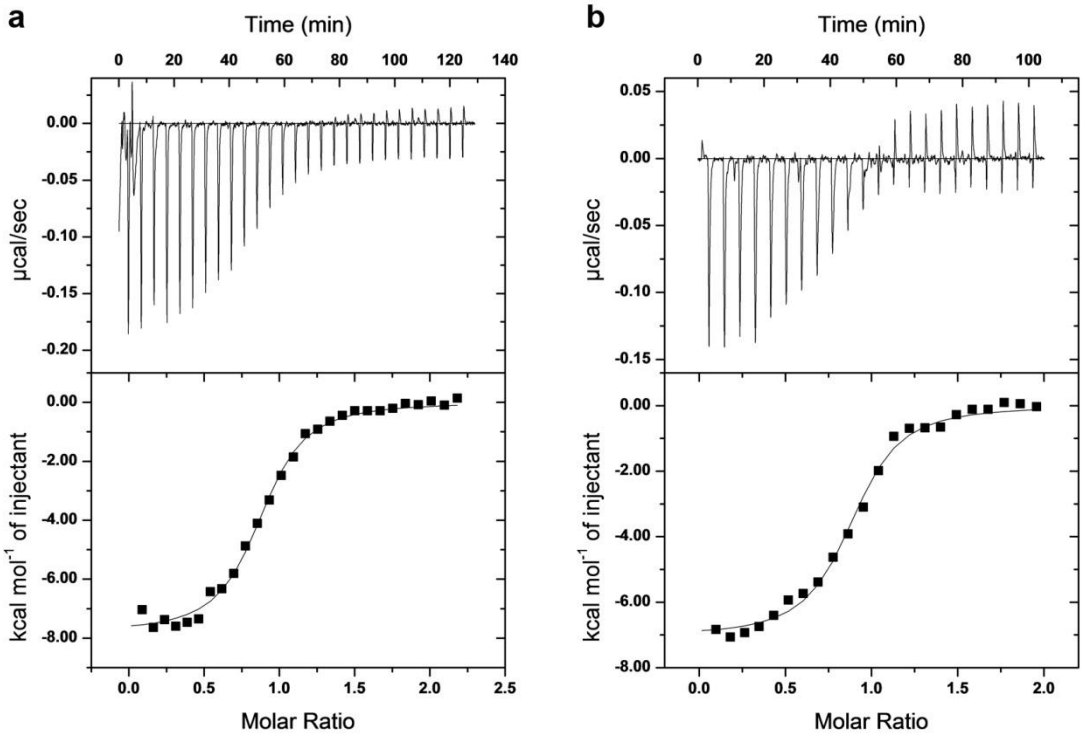

Figure 27 – a) ITC titration of 60 µM Ca^{2+}-CaM into 6 µM CAP-PAS-BDN. b) ITC titration of 60 µM Ca^{2+}-CaM into 6 µM PAS-BDN.

Table 4 – Thermodynamic parameters for CaM interaction with protein fragments containing BDN.

CaM BD	Titrant	Cell	N	K_D (nM)	ΔH (kcal mol^{-1})	ΔS (cal mol^{-1} deg^{-1})	n
BDN	Ca^{2+}-CaM	MBP-short BDN	0.77 ± 0.02	179.6 ± 16.6	-4.14 ± 0.15	17.1 ± 0.6	4
	Ca^{2+}-CaM	MBP-long BDN	0.84 ± 0.01	17.8 ± 1.1	-4.92 ± 0.06	19.4 ± 0.2	11
	Apo-CaM	MBP-long BDN	no detectable binding at 15 °C and 25 °C				2
	Ca^{2+}-N-lobe	MBP-long BDN	0.85 ± 0.07	$4.5x10^3$ ± $1.5x10^3$	-9.61 ± 0.76	-9.1 ± 2.5	2
	Ca^{2+}-C-lobe	MBP-long BDN	0.80 ± 0.06	$1.4x10^3$ ± $0.1x10^3$	-3.34 ± 0.11	15.7 ± 0.2	3
	Ca^{2+}-CaM EF12 mut	MBP-long BDN	0.68 ± 0.07	$1.4x10^3$ ± $0.1x10^3$	-2.62 ± 0.03	18.0 ± 0.2	2
	Ca^{2+}-CaM	CAP-PAS-BDN	0.77 ± 0.02	162.1 ± 6.5	-7.71 ± 0.08	5.1 ± 0.3	5
	Ca^{2+}-CaM	PAS-BDN	0.79 ± 0.02	105.9 ± 14.9	-7.47 ± 0.18	7.0 ± 0.6	3

CaM BDC2

CaM BDC2 was the first EAG1 CaM binding sequence to be identified (Schönherr et al. 2000) and it starts approximately 30 residues downstream of the CNB-homology domain (Schönherr et al. 2000; Ziechner et al. 2006).

Titration of a short BDC2 fragment (mEAG1 733-757) with Ca^{2+}-CaM, using ITC, gave a K_D = 439 ± 25 nM (Figure 28). This is on the same range of K_D that had been previously determined by fluorescence correlation spectroscopy using a peptide spanning residues 734-752 (Ziechner et al. 2006). We noticed that the MBP tag could not be removed by digestion with TEV protease after assembling the complex with CaM. This suggested that the CaM binding sequence could extend beyond the previously defined region. Thus, the BDC2 fragment was extended on both ends for further studies.

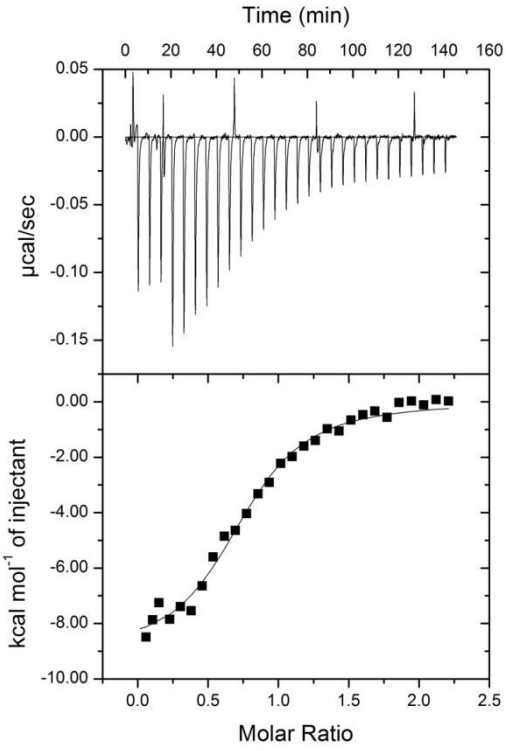

Figure 28 - ITC titration of 60 µM Ca^{2+}-CaM into 6 µM MBP-short BDC2.

A longer version of BDC2 (mEAG1 727-764) had a K_D of 68 ± 3 nM when titrated with Ca^{2+}-CaM (Figure 29a); the reverse titration – BDC2 titrated into Ca^{2+}-CaM – had a similar affinity, 74 ± 14 nM (Figure 29b), as expected for a simple 1:1 binding event. These K_D's are 6-fold lower than for the shorter version of BDC2, and the enthalpy change is more negative (ΔH (long BDC2) = -14.43 ± 0.21 kcal/mol and ΔH (short BDC2) = -8.71 ± 0.19

kcal/mol) confirming that extra residues are interacting with CaM. In the absence of calcium CaM bound to BDC2 with a K_D larger than 30 µM at 15 ºC and 25 ºC (Figure 29c).

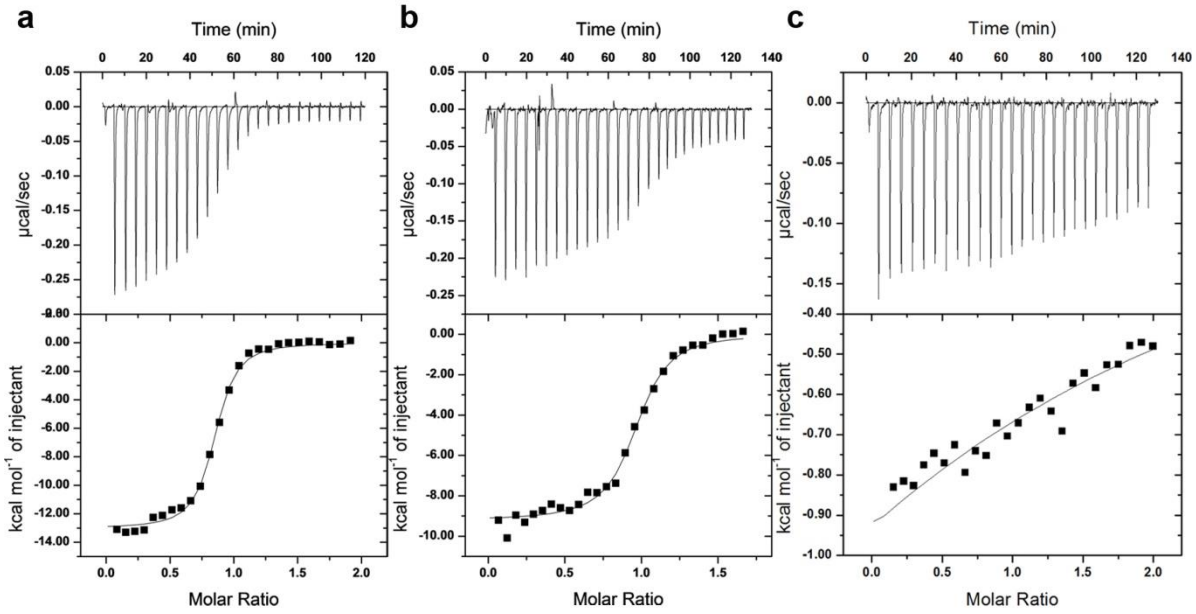

Figure 29 – a) ITC titration of 60 µM Ca^{2+}-CaM into 6 µM MBP-long BDC2. b) ITC titration of 60 µM of MBP-long BDC2 into 6 µM of Ca^{2+}-CaM. c) ITC titration of 500 µM apo-CaM into 50 µM MBP-long BDC2 (in the presence of 5 mM EDTA)

Once again we evaluated the contributions of the CaM lobes to the interaction. Interestingly, CaM N-lobe binds to BDC2 with a K_D of 2.2 ± 0.1 µM and ΔH = -2.74 ± 0.15 kcal/mol (Figure 30a) whereas the C-lobe binds almost as well as full-length CaM, with an affinity of 108 ± 10 nM and ΔH = -9.84 ± 0.30 kcal/mol (Figure 30b). Titration of BDC2 into CaM EF12 mutant is almost undistinguishable from the titration with the C-lobe (K_D = 124 ± 9 nM and ΔH = -8.75 ± 0.52 kcal/mol, Figure 30c). These experiments demonstrated that the interaction of CaM with BDC2 is dominated by the C-lobe, with little contribution from the N-lobe.

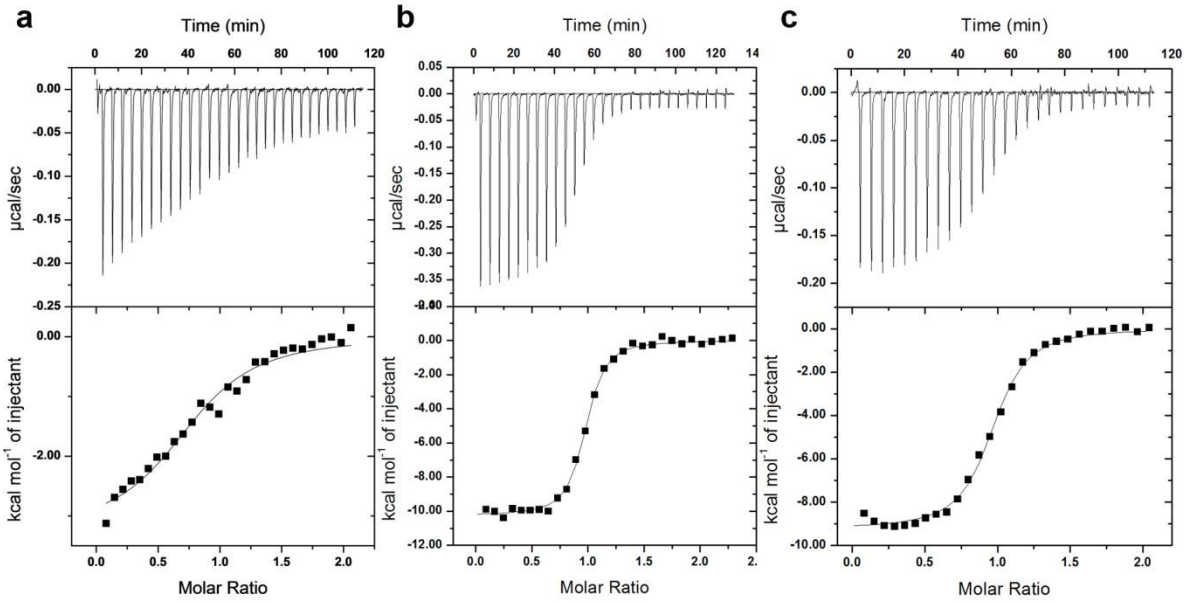

Figure 30 – a) ITC titration of 180 µM Ca^{2+}-N-lobe into 19 µM MBP-long BDC2. b) ITC titration of 100 µM Ca^{2+}-C-lobe into 10 µM MBP-long BDC2. c) ITC titration of 60 µM MBP-long BDC2 into 6 µM Ca^{2+}-CaM EF12 mutant.

Table 5 - Thermodynamic parameters for CaM interaction with protein fragments containing BDC2.

CaM BD	Titrant	Cell	N	K_D (nM)	ΔH (kcal mol^{-1})	ΔS (cal mol^{-1} deg^{-1})	n
BDC2	Ca^{2+}-CaM	MBP-short BDC2	0.76 ± 0.01	438.8 ± 24.9	-8.71 ± 0.19	0.1 ± 0.8	8
	Ca^{2+}-CaM	MBP-long BDC2	0.80 ± 0.01	67.9 ± 3.5	-14.43 ± 0.21	-15.5 ± 0.8	6
	MBP-long BDC2	Ca^{2+}-CaM	1.02 ± 0.03	74.2 ± 14.2	-9.02 ± 0.18	2.5 ± 0.2	2
	apo-CaM	MBP-long BDC2	binding detected but not quantifiable				2
	Ca^{2+}/N-lobe	MBP-long BDC2	0.74 ± 0.02	$2.2x10^3$ ± $0.1x10^3$	-2.74 ±0.15	16.7 ± 0.5	3
	Ca^{2+}/C-lobe	MBP-long BDC2	0.94 ± 0.00	107.7 ± 9.5	-9.84 ± 0.30	1.1 ± 0.9	3
	MBP-long BDC2	Ca^{2+}-CaM EF12 mut	1.12 ± 0.02	124.3 ± 9.5	-8.75 ± 0.52	2.3 ± 1.8	3

CaM/BDC2 structure

A complex between CaM and BDC2 (mEAG1 727-764) was assembled and purified. In an S200 size-exclusion column this complex migrates as a species larger than CaM alone, with a difference of more than 1 mL in elution volume (Figure 31), which cannot be simply attributed to the peptide molecular weight. Instead, since we have established that the interaction with BDC2 is dominated by the C-lobe, it most likely means that CaM is in an elongated conformation.

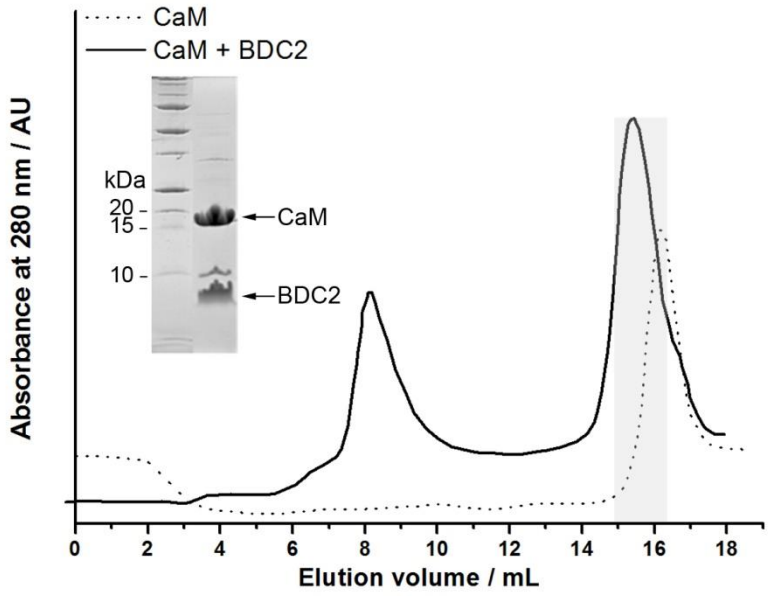

Figure 31 – Superposition of S200 size-exclusion chromatogram of CaM (dotted line) CaM/BDC2 complex (black line). Inset: 15% Tris-tricine SDS-PAGE of CaM/BDC2 complex fraction used for crystallization trials (highlighted in grey).

Crystals of the complex CaM/BDC2 were obtained at 20 ºC in a condition with 0.2 M di-ammonium citrate pH 5 and 20% PEG 3350 (Figure 32a and b).

Diffraction experiments showed that the protein complex crystallized in space group $C222_1$ with unit cell dimensions 53.6, 121.1, 73.9 Å/90 90 90°. Data extended to 2.85 Å resolution and crystallographic data and statistics are reported in Table 6. The structure was solved by molecular replacement using the apo-N-lobe from PDB code 1CFD and Ca^{2+}-C-lobe from PDB code 3OXQ (chain A) as template, containing one molecule of CaM and BDC2 per asymmetric unit The structure was refined to a final Rwork = 20.6% and Rfree = 26.5%.

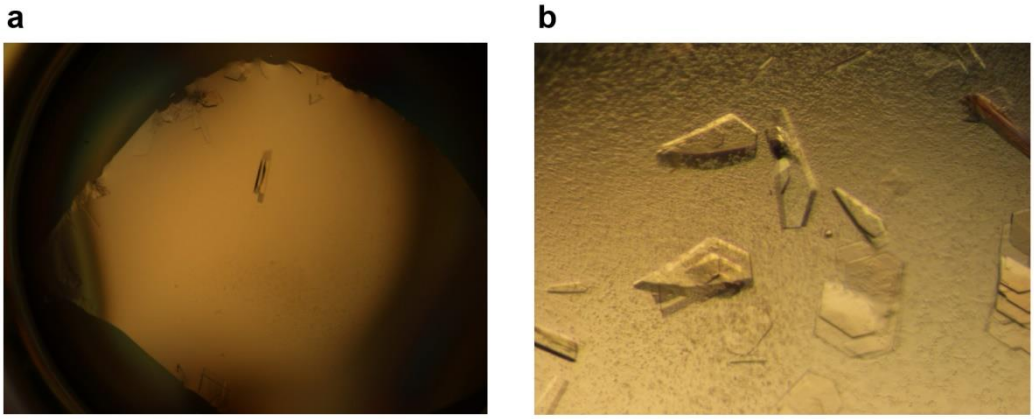

Figure 32 – CaM/BDC2 crystals grown with 0.2 M di-ammonium citrate pH 5, 20% PEG 3350. a) Original condition, from the commercial screen; b) crystals reproduced with a finescreen around the original condition.

Table 6 – Crystallographic statistics

Crystal data	
Space group	$C222_1$
Unit cell parameters	
a (Å)	53.62
b (Å)	121.14
c (Å)	73.86
α=β=γ(°)	90
Data-collection details	
Diffraction source	Soleil Proxima 2A
Wavelength (Å)	0.9765
Resolution range (Å)	46.83-2.85 (2.95-2.85)
No unique reflections	5816 (564)
No measured reflections	23869 (3540)
Multiplicity	4.1 (4.2)
Completeness (%)	98.74 (98.95)
I/σI	15.28 (2.68)
R_{meas} (%)	8.2 (70.0)
CC1/2 (%)	99.9 (79.5)
Refinement data	
Resolution range	46.83-2.85 (2.95-2.85)
No reflections	5816
R_{work}/R_{free} (%)	20.6/26.5 (28.5/34.8)
No of atoms in model: protein	1249
solvent	10
ligand	2
Average B-value (Å^2): protein	51.7
solvent	39.9
ligand	37.8
RMSD bond length (Å)	0.002
RMSD bond angles (°)	0.44

The CaM structure was built in an extended conformation, with the central linker forming a long α-helix (Figure 33a). The N-lobe of CaM is in the apo form, without calcium ions in EF-hands 1 or 2; in contrast, C-lobe's EF-hands 3 and 4 contain Ca^{2+} bound. This feature was unexpected given that high Ca^{2+} concentrations were kept throughout the purification and crystal freezing. As a consequence of the absence of Ca^{2+}, residues 57-59 from the second EF-hand from the N-lobe were very ill-defined and were not modelled. The last aminoacid of CaM, K148 was also not visible.

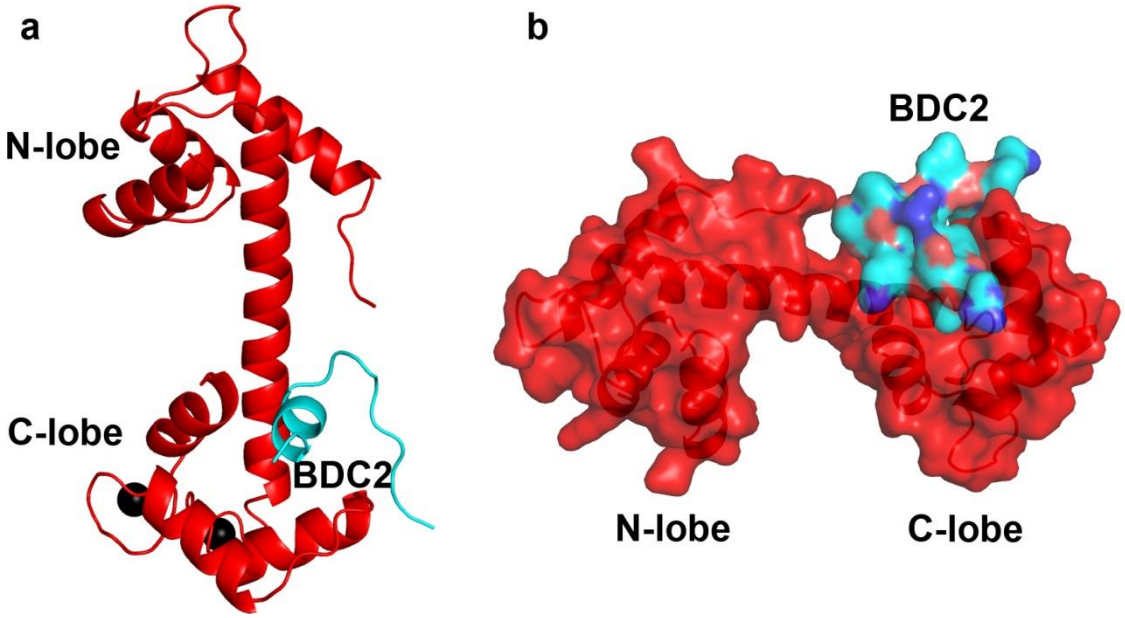

Figure 33 – a) Structure of CaM/BDC2 (CaM is in red cartoon representation and BDC2 in cyan. Calcium ions are represented by black spheres); b) Horizontal view of CaM/BDC2 complex in surface representation.

Importantly, extra electron density, corresponding to the BDC2 peptide, was detected in close proximity to the C-lobe. Residues 727-743 from the long BDC2 peptide (mEAG1 727-764), corresponding to the sequence APLILPPDHPVRRLFQR (Figure 34) were built into this density. No electron density could be seen for the C-terminal half of the peptide, probably due to crystal packing restraints. The modelled sequence is different from the sequence previously reported to be the binding site for Ca^{2+}-CaM (underlined in Table 2). The sequence is instead shifted towards the N terminus. These extra residues on the N-terminal explain why the affinity of CaM for the longer BDC2 fragment is higher than for the short version and the inability of TEV protease to cleave off the MBP tag after assembling the complex short BDC2/CaM.

The channel fragment sits on the C-lobe's hydrophobic cleft. In addition, some of the N-terminal residues lie in a groove between the C-lobe of one CaM, and the N-lobe of a symmetry related CaM (Figure 34). The conformation of the channel fragment starts with a 5-residue segment in extended conformation that bends and turns into a small helix. The helix includes part of the sequence previously reported to form BDC2 (Ziechner et al. 2006). This fold is uncommon for CaM binding peptides, which in the majority of structures deposited in the Protein Data Bank are entirely α-helical. From a collection of more than 80 structures of CaM in complex with small peptides and large proteins (Tidow & Nissen 2013), only two are bound to a short helical peptide with a bend (PDB codes 1IWQ and 4EHQ).

We submitted the CaM/BDC2 structure to the servers PIC: Protein Interactions Calculator (http://pic.mbu.iisc.ernet.in) and PISA (Protein interfaces, surfaces and assemblies) (Krissinel & Henrick 2007), from the European Bioinformatics Institute, (http://www.ebi.ac.uk/pdbe/prot_int/pistart.html), a method based on physical-chemical models of macromolecular interactions and chemical thermodynamics, to define what residues form the interacting surface between CaM and BDC2 as well as the type of interactions established between them and to determine the extent of the interface (Figure 34 and Table 7).

There is a hydrogen bond between the peptide's L729 backbone and CaM N111 backbone and between the peptide's R739 sidechain and the main chain of CaM M145 (Figure 34 and 36, Table 7). Out of the 17 mEAG1 residues modelled into the electron density, 12 are involved in the interface with CaM with a total interface area of 531 $Å^2$ and 520 $Å^2$ for peptide and CaM, respectively. Of these residues, H735, P736, V737 and L740 are the ones with a larger percentage of buried surface area upon complex formation (between 50-100%) and the last three are involved in an extensive hydrophobic interaction network with the CaM C-lobe (Figure 36 and Table 7).

Table 7 – Interaction network between BDC2 and CaM.
Residues making hydrogen bonds are underlined and the remaining residues are involved in hydrophobic interactions.

BDC2 (mEAG1)	CaM
P728	G113
L729	L112

	N111
L731	L112
P736	I85 M145
V737	A88 F92 L112 M145
R739	M145
L740	M124 M144 M145
F741	L112 E114

The analysis also revealed that the bend in BDC2 is probably stabilized by an intra-peptide main chain-main chain hydrogen bond network involving residues P732, P733, D734 and H735 (Figure 36). Furthermore, several interactions between the N-terminal extended stretch of BDC2 and a symmetry related CaM N-lobe which include a hydrogen bond between mEAG1 I730 and CaM S38 might stabilize this conformation (Figure 34).

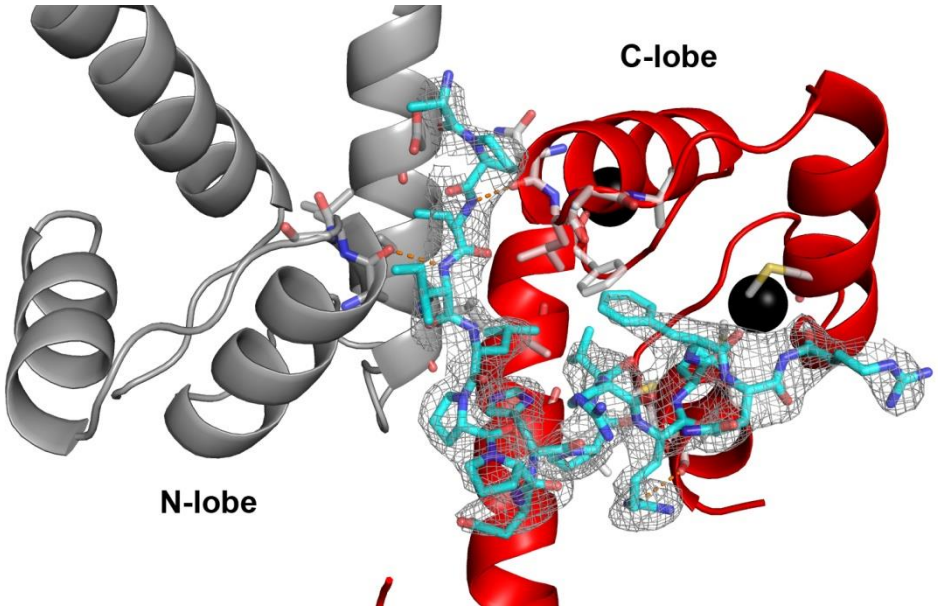

Figure 34 – Close up view of the crystal contacts on the interface between BDC2 and CaM. CaM is in red cartoon representation and the N-lobe from a symmetry related CaM is in grey. The residues in the interface of the complex are in stick representation. BDC2 is in cyan stick model with the corresponding electron density map in grey mesh contoured at 1.0 σ.

The structure was also analyzed with the Protein structure comparison service Fold at European Bioinformatics Institute (http://www.ebi.ac.uk/msd-srv/ssm), PDBeFold (Taraska et al. 2009). This server does pairwise secondary-structure match (through the α-carbon, αC) with all structures deposited on the Protein Data Bank and displays hits ordered by a "Q-score" which takes into account the root mean standard deviation (RMSD) of the superposition as well as its residue length. Values range from 0 to 1, where a score of 1 indicates a perfect match. The top 3 hits for our CaM structures have Q-scores around 0.5, which is indicative of significant differences in the structural arrangement, In general, there is a good match between our structure and the top 3 hits along the central linker and C-lobe region, but in the N-lobe region there are significant differences, particularly in the Ca^{2+} binding loops and in the angles between the helices, since all three structures have Ca^{2+} bound to the N-lobe (Figure 35a, b, c). The structure with the most similar fold to our CaM is a CaM "trapped intermediate" (PDB code 1Y6W, Figure 35a), a conformation in which the N-lobe has Ca^{2+} bound but is kept in a closed (apo-like) conformation, due to the introduction of two cysteines that form a disulfide bond, preventing the exposure of the N-lobe's hydrophobic pocket that occurs upon binding of Ca^{2+}.

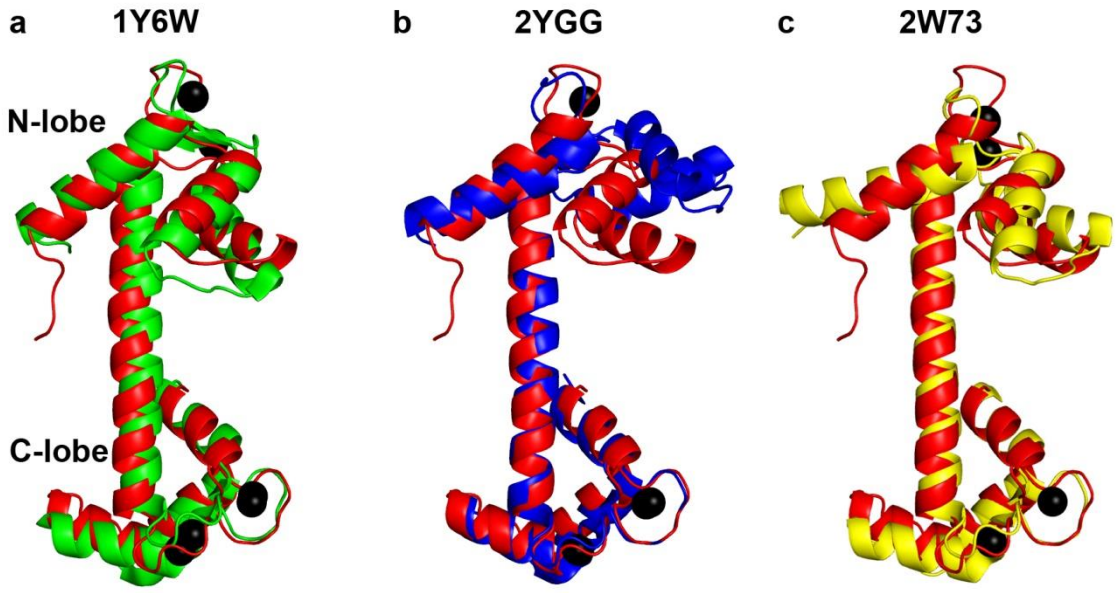

Figure 35 – Superposition of CaM from the CaM/BDC2 complex (red) with the top 3 hits obtained from PDBeFold. a) trapped intermediate of CaM (PDB code 1Y6W, green). b) CaM in complex with a fragment from a Na^+/H^+ exchanger (PDB code 2YGG, blue). c) CaM in complex with calcineurin (PDB code 2W73, yellow).

Submission of just the N-lobe of CaM from our structure into PDBeFold results in more than 700 hits with Q-scores starting in 0.58. The most similar structures are EF-hand containing-proteins like troponin C and calcium binding protein 1. The first CaM structure in the list is found at number 10 and is a soybean CaM N-lobe bound to Mg^{2+} (PDB code 2KSZ) with a Q-score of 0.49. This analysis showed that our apo-N-lobe conformation is significantly different from other deposited structures.

Overall the CaM/BDC2 structure explains well the ITC data, confirming that the interaction of CaM with BDC2 is dominated by the C-lobe.

BDC2 mutants

To assess the contributions of the different residues discussed above (Figure 36) to the stability of the CaM/BDC2 complex we performed alanine-scanning analysis on BDC2, using ITC. The thermodynamic parameters for binding of the different mutants to Ca^{2+}-CaM are summarized in Table 7. Our collaborators Johannes Oppermann and Dr. Roland Schönherr, at Jena University Hospital, performed preliminary experiments on the functional impact of some BDC2 mutations on the Ca^{2+}-dependent inhibition of the hEAG1 channels expressed in *Xenopus* oocytes.

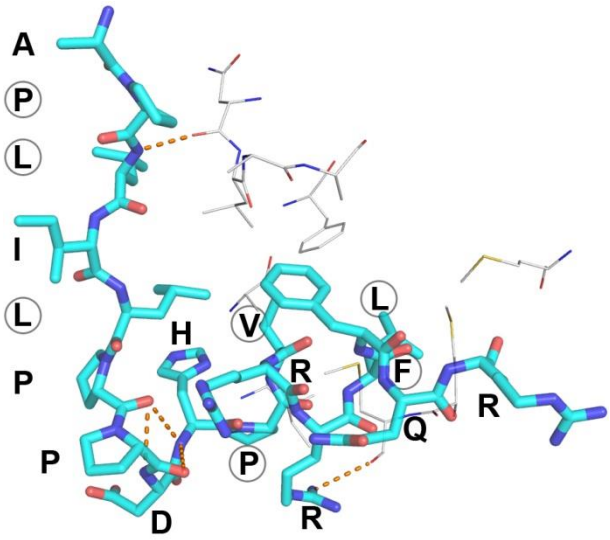

Figure 36 - Stick representation of the modelled BDC2 residues (mEAG1 727-743), labelled with the corresponding primary sequence. CaM residues that interact with BDC2 are in lines. Grey circles identify residues involved in hydrophobic interactions with CaM and the hydrogen bonds with CaM are marked with orange dashes.

We tested the importance of the interactions formed by the two leucines from the peptide's extended region. These residues make hydrophobic interactions with the C-lobe of CaM and L729 makes a main chain-main chain hydrogen bond with CaM's N111. The affinity for CaM dropped 4.5-fold, with a K_D ~ 300 nM, both in the direct and reverse titrations (Figure 37a and b). Although the affinity drop is minor, the same mutants in the context of the whole channel reveal altered Ca^{2+} sensitivity. When exposed to the calcium ionophore ionomycin, that raises the intracellular concentration of Ca^{2+}, the currents of hEAG1 channels with the double mutation are less inhibited relative to WT channels.

We also generated the BDC2 mutant L729A/L731A/R739A. The R739 is well defined on the electron density map and makes a hydrogen bond between the guanine group and the main-chain carbonyl oxygen from CaM's M145 (Figure 36). This triple mutant showed a much larger effect on ITC, the affinity dropped over 30-fold relative to the WT BDC2, to 2.1 ± 0.1 µM (Figure 37c).

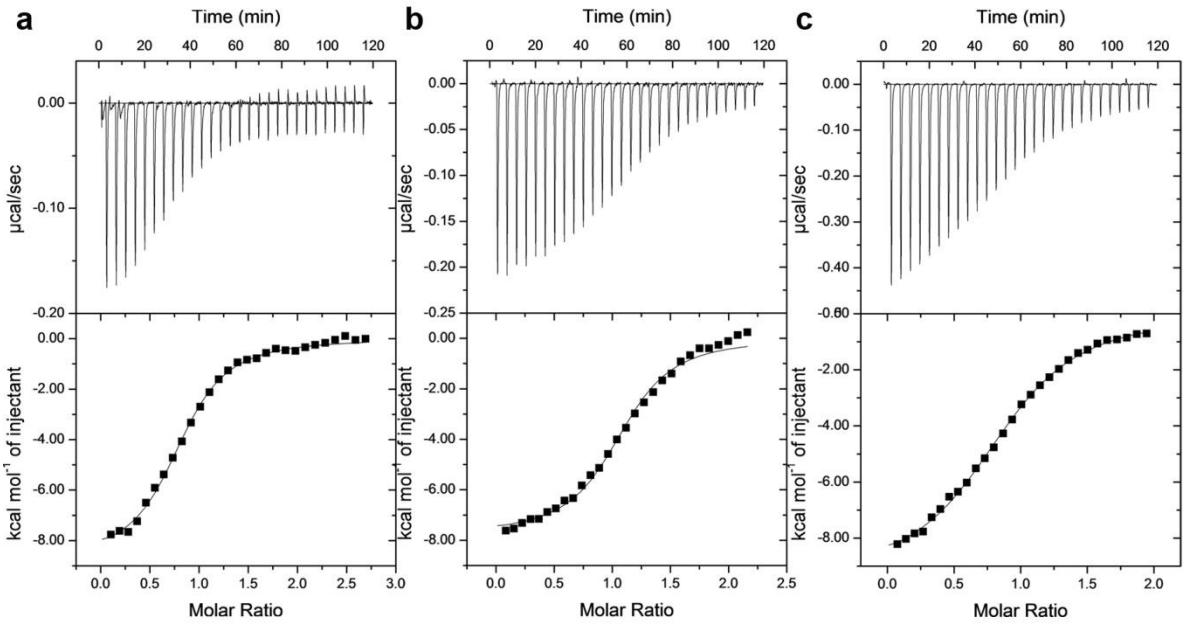

Figure 37 - a) ITC titration of 100 µM Ca^{2+}-CaM into 10 µM MBP-BDC2 mutant L729A/L731A. b) ITC titration of 80 µM MBP-BDC2 mutant L729A/L731A into 7 µM Ca^{2+}-CaM. c) ITC titration of 100 µM Ca^{2+}-CaM into 10 µM MBP-BDC2 mutant L729A/L731A/R739A.

Residues D734 and H735 are located on the BDC2 bend and make intra-peptide interactions (Figure 36). Although these residues are not directly interacting with CaM, we wanted to see if truncating their sidechains would destabilize the peptide bend conformation and consequently alter binding of BDC2 to CaM. A double mutation to alanine did not alter affinity towards CaM (K_D = 102.3 ± 11.1 nM) but the thermodynamic parameters were very different (Figure 38). This interaction is now much less enthalpically driven with a ΔH = -5.5 ± 0.1 kcal/mol, relative to the ΔH = -14.4 ± 0.2 kcal/mol for the WT. The enthalpic penalty was compensated by a large increase in entropy from -15.5 to 13.6 cal/mol/deg. It is possible that the mutations destabilized the peptide bend conformation, allowing more conformational freedom to the CaM complex increasing the entropy of the system. Strikingly, channels with this double mutation are less sensitive Ca^{2+}. This suggests that the BDC2 bend is mechanistically important.

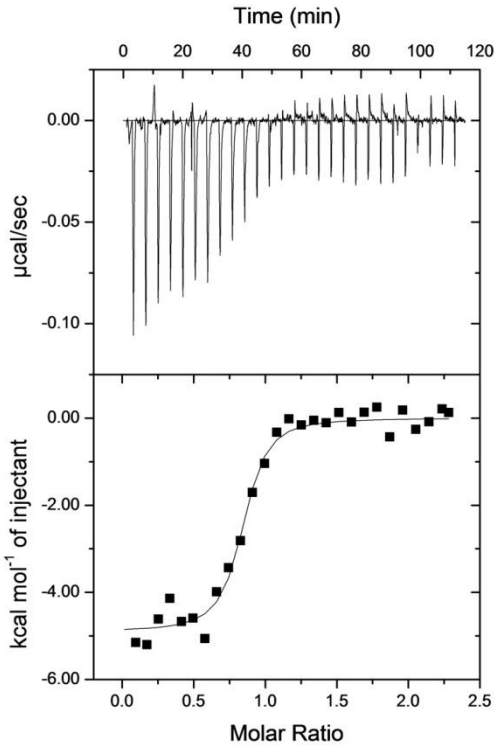

Figure 38 - ITC titration of 60 µM Ca^{2+}-CaM into 6 µM MBP-BDC2 mutant D734A/H735A.

We also investigated the impact of residues on the helical region of the peptide that face the hydrophobic cleft of CaM. Double mutant P736A/V737A hardly alters binding to CaM, with a K_D of 118.2 ± 4.4 nM (Figure 39a), ΔH of -9.5 ± 0.3 kcal/mol and ΔS around zero. Nevertheless, hEAG1 channels with these mutations show decreased Ca^{2+} sensitivity. Quadruple mutant P736A/V737A/L740A/F741A that truncates one of the phenylalanine thought to be important for the interaction between CaM and BDC2 displays a mere 3-fold drop in affinity for CaM, with a K_D of 204.0 ± 20.0 nM, and ΔH and ΔS values indistinguishable from mutant P736A/V737A (Figure 39b, Table 7), indicating that there were no significant readjustments in the CaM-mutant BDC2 interface.

Double mutation of the most buried residues V737 and L740 also does not affect the CaM affinity (Figure 40a and Table 8).

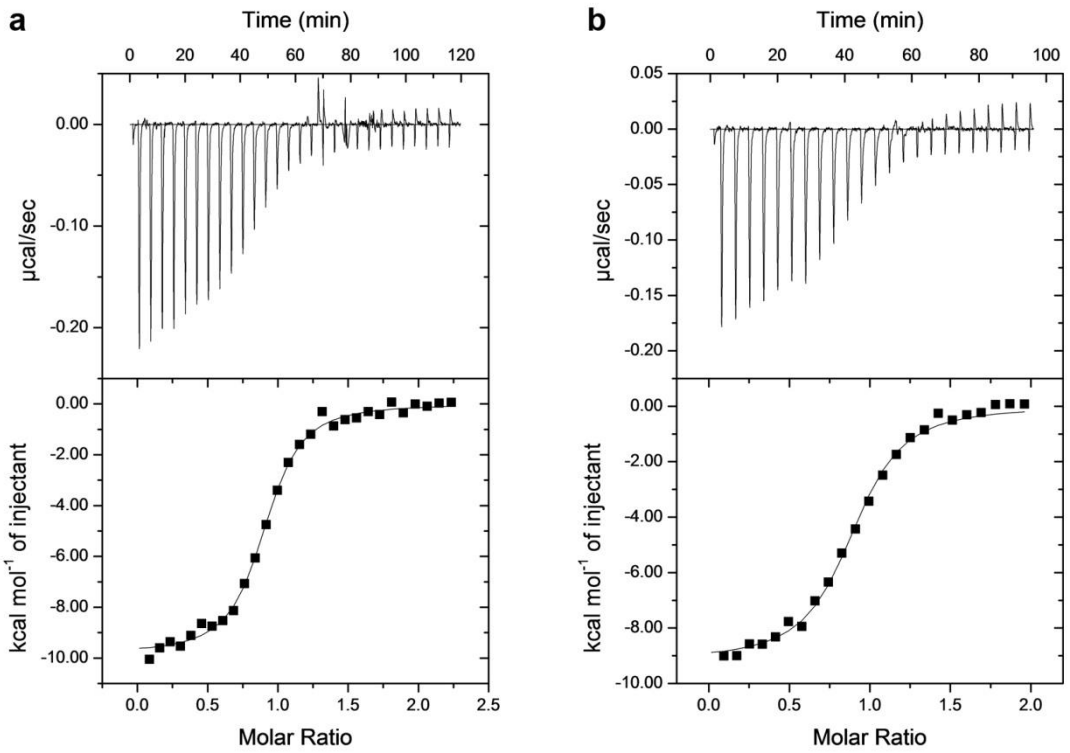

Figure 39 – a) ITC titration of 60 µM Ca^{2+}-CaM into 6 µM MBP-BDC2 mutant P736A/V737A. b) ITC titration of 60 µM Ca^{2+}-CaM into 6 µM MBP-BDC2 mutant P736A/V737A/L740A/F741A

The very small impact of these mutations was surprising, since many of these residues make extensive interactions with the C-lobe (Figure 36). To exclude the possibility that some of these BDC2 mutants are now interacting with the N-lobe of CaM, we performed a titration with CaM EF12 mutant and BDC2 mutant V737A/L740A. BDC2 V737A/L740A binds CaM EF12 mutant as well as WT BDC2 (K_D ~ 100 nM and similar ΔH and ΔS, Figure 40b), showing that truncation of sidechains buried in CaM apolar pocket still results in a interaction dominated by the C-lobe. To further explore the role of V737 and L740 on the interaction with CaM we substituted by the polar amino acid serine. We determined that the affinity for CaM is severely affected, with a K_D of 15.6 ± 0.7 µM (Figure 40c), supporting that those apolar sidechains are important for the complex, as seen in the structure.

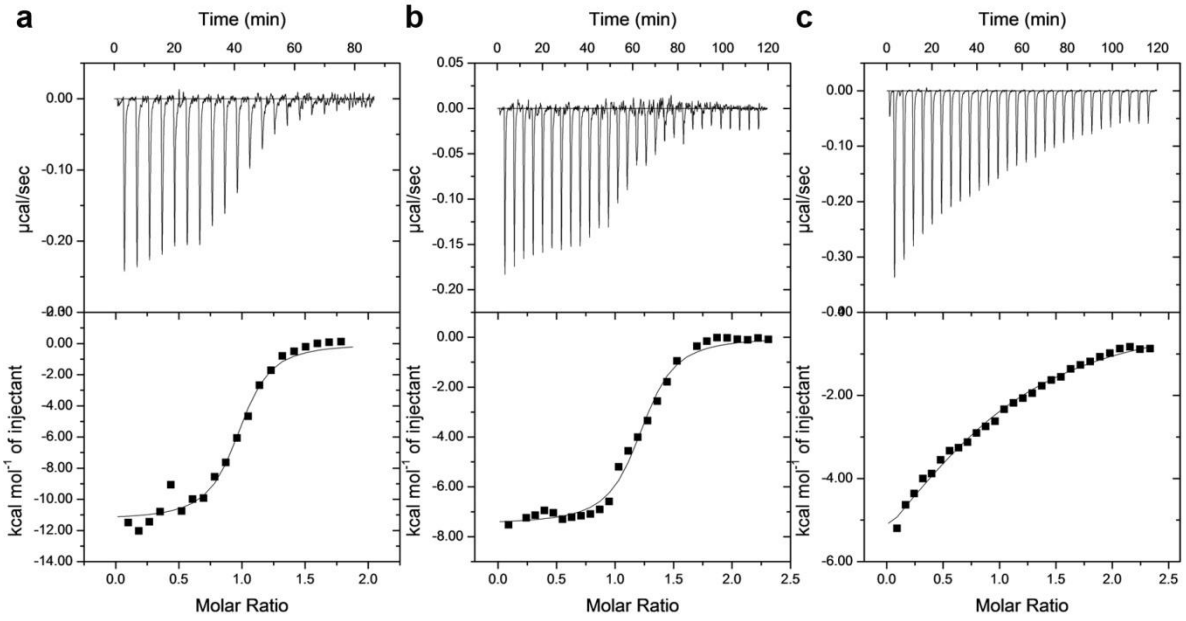

Figure 40 – a) ITC titration of 60 µM Ca^{2+}-CaM into 6 µM MBP-BDC2 mutant V737A/L740A. b) ITC titration of 60 µM Ca^{2+}-CaM EF12 mutant into 6 µM MBP-BDC2 mutant V737A/L740A. c) ITC titration of 170 µM Ca^{2+}-CaM into 17 µM MBP-BDC2 mutant V737S/L740S.

It had previously been reported that two phenylalanines in BDC2 were essential for CaM inhibition of the full-length channel (Schönherr et al. 2000). Additionally, a channel fragment containing mutations to serine in these two phenylalanines had shown a 6-fold decrease in affinity for fluorescently labelled CaM (Ziechner et al. 2006). Although we only see the first phenylalanine in our structure (F741 and F744, in mEAG1), we investigated their role on CaM binding using ITC. BDC2 mutant F741S showed a 28-fold drop in affinity towards CaM (K_D = 1.9 ± 0.1 µM, Figure 41a), which is comparable to the triple mutant L729A/L731A/R739A, whereas the double mutant F741S/F744S revealed an even more drastic effect (Figure 42b) with a K_D that is now over 500-fold higher than the WT. The further drop in affinity with the double mutant confirms that the second phenylalanine is important for CaM binding and the fact that it is not visible in the structure might be related to crystal packing restraints.

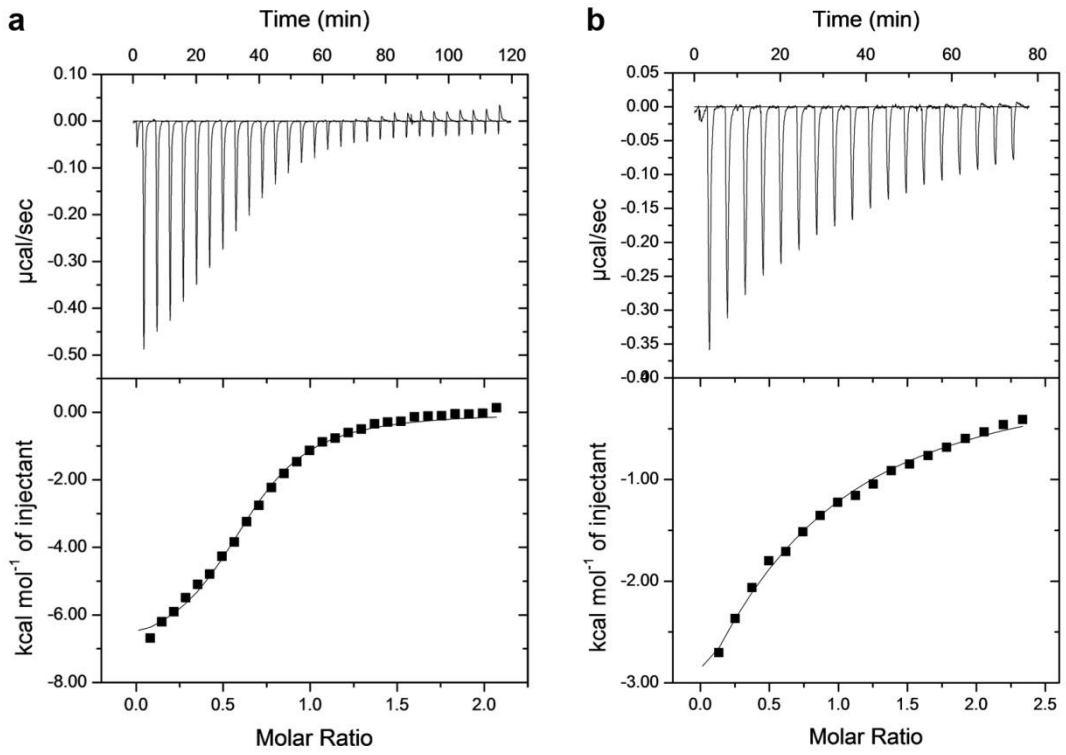

Figure 41 – a) ITC titration of 200 µM Ca^{2+}-CaM into 20 µM MBP-BDC2 mutant F741S. b) ITC titration of 336 µM Ca^{2+}-CaM into 31 µM MBP-BDC2 mutant F741S/F744S

Overall, mutations in the BDC2 residues which make interactions with CaM in the crystal structure consistently result an increase in ΔH when titrated with CaM, indicative of a weaker bonding network. While these mutations had moderate effects in the binding of CaM in solution, several of them caused a decrease in Ca^{2+}-dependent inhibition, in the context of the full-length hEAG1 channel. Importantly, we were able to show that the residues in the extended stretch of our peptide structure, which had not been described in the literature, are involved in CaM binding. Mutations on that region have an effect on binding to CaM and as well as on channel inhibition by Ca^{2+}-CaM. These results support the proposition of a new BDC2 sequence, which is extended towards residue L729.

Table 8 - Thermodynamic parameters for CaM interaction with long BDC2 mutants.

MBP-long BDC2	**K_D (nM)**	$\frac{\textbf{KD mut}}{\textbf{KD WT}}$	ΔH (kcal mol^{-1})	ΔS (cal $mol^{-1}deg^{-1}$)	N	n
WT	**67.9 ± 3.5**	**1**	**-14.43 ± 0.21**	-15.5 ± 0.8	0.80 ± 0.01	6
(reverse)	**74.2 ± 14.2**		-9.02 ± 0.18	2.5 ± 0.2	1.02 ± 0.03	2
L729A/L731A	**296.8 ± 21.8**	**4.4**	-8.87 ± 0.11	0.2 ± 0.3	0.84 ± 0.00	4
(reverse)	**303.7 ± 9.8**	**4.5**	-7.73 ± 0.50	3.9 ± 1.7	0.95 ± 0.02	2
D734A/H735A	102.3 ± 11.1	1.5	-5.53 ± 0.14	13.6 ± 0.7	0.86 ± 0.02	4
P736A/V737A	118.2 ± 4.4	1.7	-9.46 ± 0.33	0.0 ± 1.2	0.91 ± 0.02	3
P736A/V737A/L740A/F741A	**204.0** ± 20.0	**3.0**	-9.39 ± 0.26	-0.8 ± 1.0	0.87 ± 0.04	3
L729A/L731A/R739A	**$2.1x10^3 \pm 0.1x10^3$**	**31.0**	-9.14 ± 0.09	-4.7 ± 0.4	0.94 ± 0.01	3
V737A/L740A	73.8 ± 9.5	1.1	-10.76 ± 0.23	3.3 ± 0.8	0.93 ± 0.01	3
V737S/L740S	**$15.6x10^3 \pm 0.7\ x10^3$**	**230.1**	-11.08 ± 1.25	-15.2 ± 4.3	0.77 ± 0.08	2
F741S	**$1.9x10^3 \pm 0.1x10^3$**	**28.4**	-6.72 ± 0.15	3.6 ± 0.5	0.70 ± 0.02	3
F741S/F744S	**> 40000**	**> 500**	ND	ND	ND	1

CNBhD-BDC1-BDC2

After dissecting the binding properties of the individual CaM binding regions and of PAS-BDN and CNBhD-BDC1 – we studied a longer construct, comprising the CNB-homology domain and the two C-terminal CaM binding sites BDC1 and BDC2 (mEAG1 552-764).

This longer construct had to be co-expressed with CaM for protection against proteolysis. In addition, it required extra purification steps that included ion exchange chromatography (Figure 42) and CaMTrap affinity chromatography

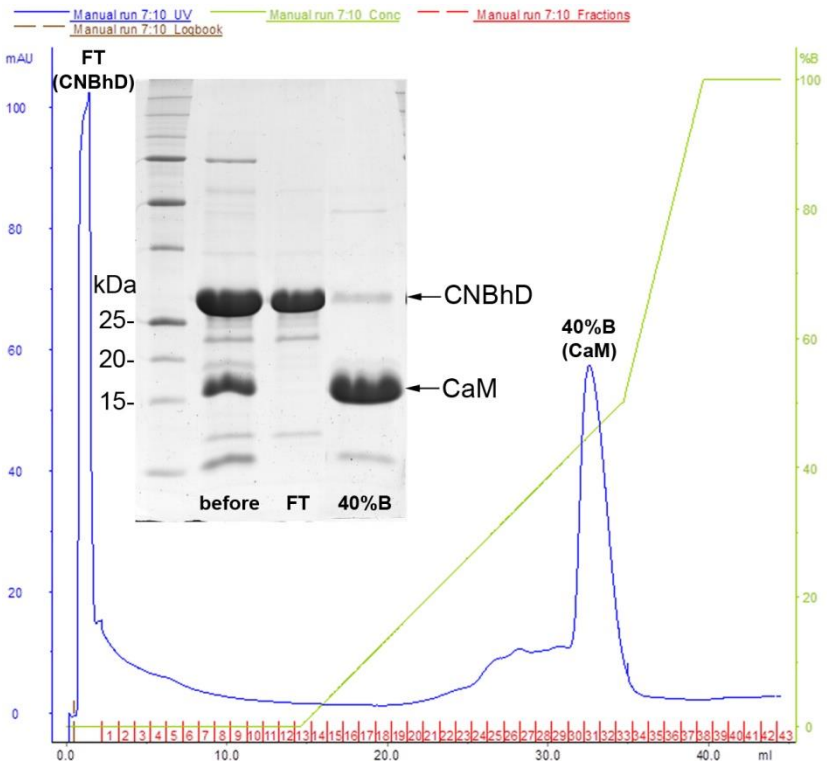

Figure 42 - HitrapQ ion exchange chromatogram of the separation of CNBhD-BDC1-BDC2 from CaM. Inset: 17% SDS-PAGE of fractions before and after ion exchange purification.

Size-exclusion chromatography profiles show that CNBhD-BDC1-BDC2 elutes at 15.2 mL, and CaM at 16.5 mL (Figure 43). Calibration of this S200 column with protein standards showed that a globular protein with the same molecular weight as CNBhD-BDC1-BDC2 (~27 kDa) elutes at 16 mL. CNBhD-BDC1-BDC2 in complex with CaM suffers a large shift in the elution profile, eluting at 14 mL. In the same S200 column, MBP fusions of ~45 KDa that consist of two globular domains with a small peptide extension on the C-terminal are eluted at 15 mL. The elution volume of the CNBhD-BDC1-BDC2/CaM complex is

suggestive of either a species larger than 44 kDa (the sum of the CaM and CNBhD-BDC1-BDC2 molecular weights) or of an elongated species.

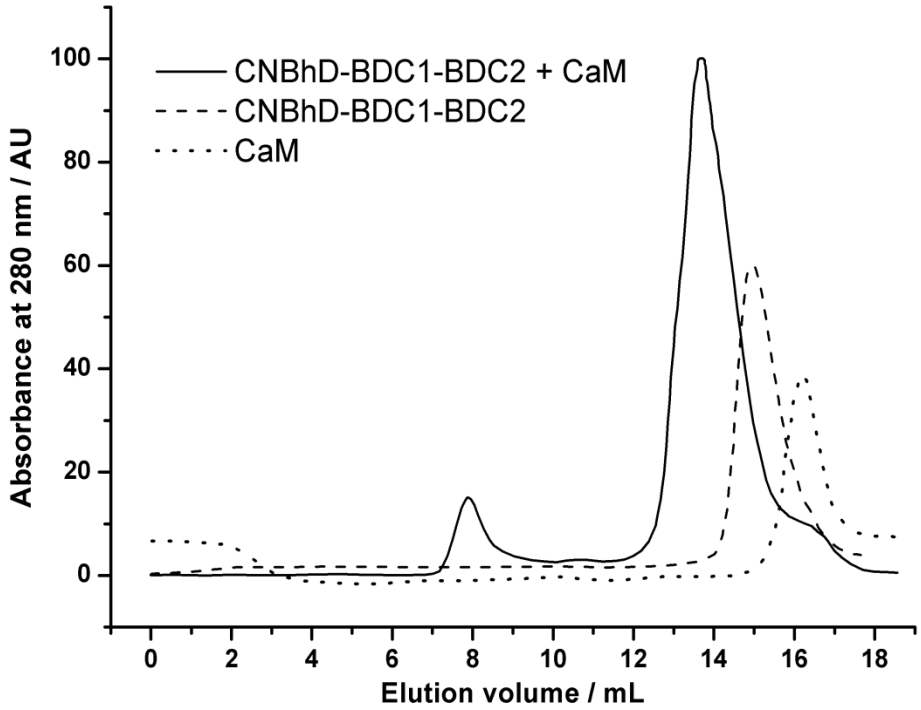

Figure 43 - Superposition of S200 size exclusion chromatograms of mEAG 552-764 (dashed line), CaM (dotted line) and equimolar amounts of mEAG 552-764 and CaM (continuous line).

The isotherm of the interaction between CNBhD-BDC1-BDC2 and CaM showed two steps with different slopes that occur at sub-stoichiometric molar ratios (Figure 44a). This isotherm could not be properly explained with the single set of sites model for 1:1 interactions implemented in the Origin for ITC software package. Reversing the titration (CNBhD-BDC1-BDC2 into CaM) resulted in an even more complicated isotherm, with three different steps (Figure 44b), and heats of reaction (ΔH) that are less than half of those of the direct titration. These isotherms suggested that there were several species in equilibrium.

Our collaborators Dr. Guillaume Gabant and Dr. Martine Cadene at CNRS, France performed native mass spectrometry to determine the oligomeric state of CNBhD-BDC1-BDC2 in isolation and in complex with CaM. This technique allows the study of intact proteins or protein complexes through the use of mild ionization conditions in the

presence of a volatile buffer that preserves the sample's quaternary structure (Heck 2008). It can be used to determine stoichiometry, topology and dynamics of protein complexes and has a large sensitivity. The native mass spectrometry analysis showed that the major CNBhD-BDC1-BDC2 species is a monomer; however, a residual amount of CNBhD-BDC1-BDC2 dimer could be observed. In the presence of CaM, the 1:1 complex was the major species but minor species of complex forms 1:2 and 2:2 were also detected (CNBhD-BDC1-BDC2:CaM).

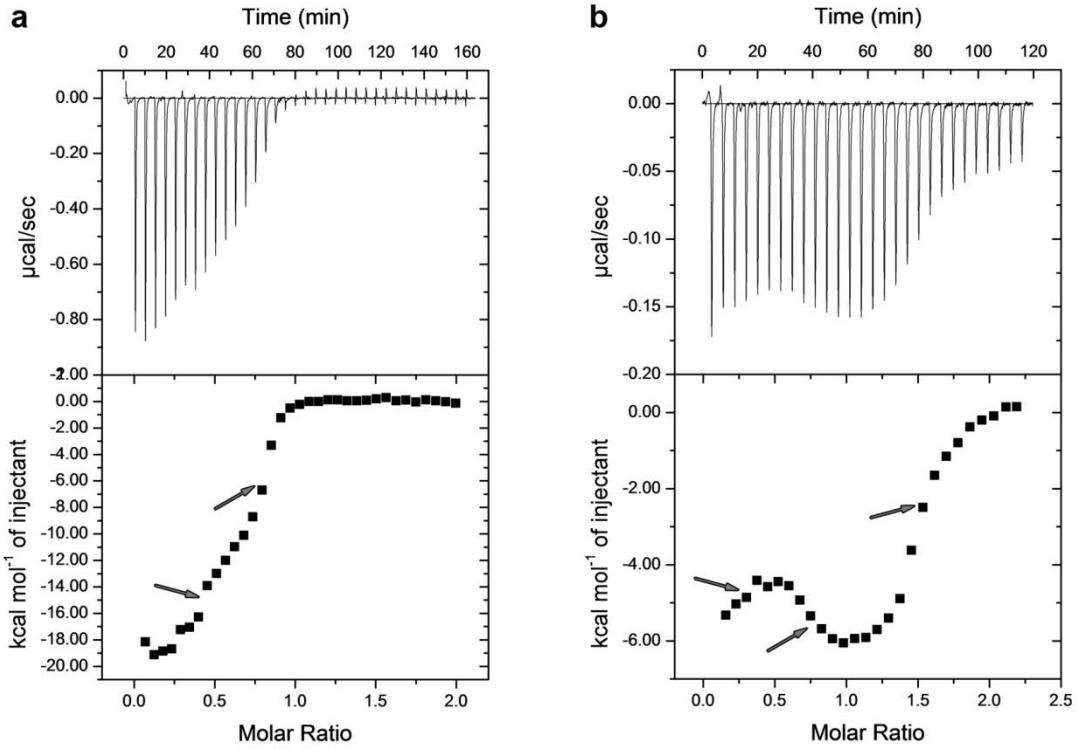

Figure 44 – a) ITC titration of 187 µM Ca^{2+}-CaM into 17 µM CNBhD-BDC1-BDC2 (direct). b) ITC titration of 60 µM CNBhD-BDC1-BDC2 into 6 µM Ca^{2+}-CaM (reverse). The different binding steps are indicated by grey arrows.

In an attempt to gain some insights into the complicated interaction of full-length CaM with this protein fragment, we performed ITC titrations with the isolated CaM lobes. CNBhD-BDC1-BDC2 binds to the CaM N-lobe with a K_D of 1.3 ± 0.1 µM and ΔH = -4.43 ± 0.09 kcal/mol (Figure 45a) and to the C-lobe with K_D = 75.0 ± 8.4 nM and ΔH = -13.13 ± 0.26 kcal/mol for the C-lobe (Figure 45b). This channel fragment interacts with the CaM lobes with distinct affinities and enthalpies, binding more tightly to the C-lobe than to the N-lobe, like we observed for BDC2. Titration of CaM EF12 mutant into CNBhD-BDC1-BDC2 has a K_D of 38.8 ± 4.4 nM and ΔH = -10.36 ± 0.32 kcal/mol and the reverse titration (CNBhD-BDC1-BDC2 into EF12 mut) gave a K_D ~ 62 nM and ΔH ~ -7.6 kcal/mol (Figure 45 c and

d, respectively), confirming that there is a parallel between CNBhD-BDC1-BDC2 and BDC2.

Interestingly, none of the titrations of the single lobes or CaM EF12 mutant with CNBhD-BDC1-BDC2 exhibited the two slopes that are observed with full-length CaM, indicating that the Ca^{2+}-N-lobe is involved in this behavior. Moreover, these titrations were easily fitted with a single binding site model with a stoichiometry close to 1, suggesting that the two slopes in the titration with full-length CaM correspond to separate interactions of N- and C-lobe.

Since we have shown before that BDC2 interacts preferentially with the C-lobe and BDC1 with the N-lobe (Marques-Carvalho et al. 2012), we wondered if BDC1 could be involved in the interaction of this longer channel fragment with CaM. To assess this, a quadruple mutation on BDC1 (R702N/R704N/R708N/K709N) that decreases the affinity of CaM for BDC1 even further was created on CNBhD-BDC1-BDC2. Titration with CaM still showed two slopes (Figure 46a), indicating that BDC1 is not responsible for this feature.

We also created MBP fusions with two channel fragments that do not include the CNB-homology domain: BDC1-BDC2 (mEAG1 696-764) and a fragment that starts just after BDC1 and includes BDC2 (mEAG1 712-764). Both fusions displayed a binding isotherm with two slopes when titrated with CaM (Figure 46b and 46c), demonstrating that the CNB-homology domain region is not involved in this multistep binding. The observation that mEAG1 712-764 still shows two steps confirms that BDC1 does not play a role in the second binding event. Overall, these experiments indicate that N- and C-lobe are interacting with a mEAG1 channel fragment that starts after BDC1 and extends towards BDC2.

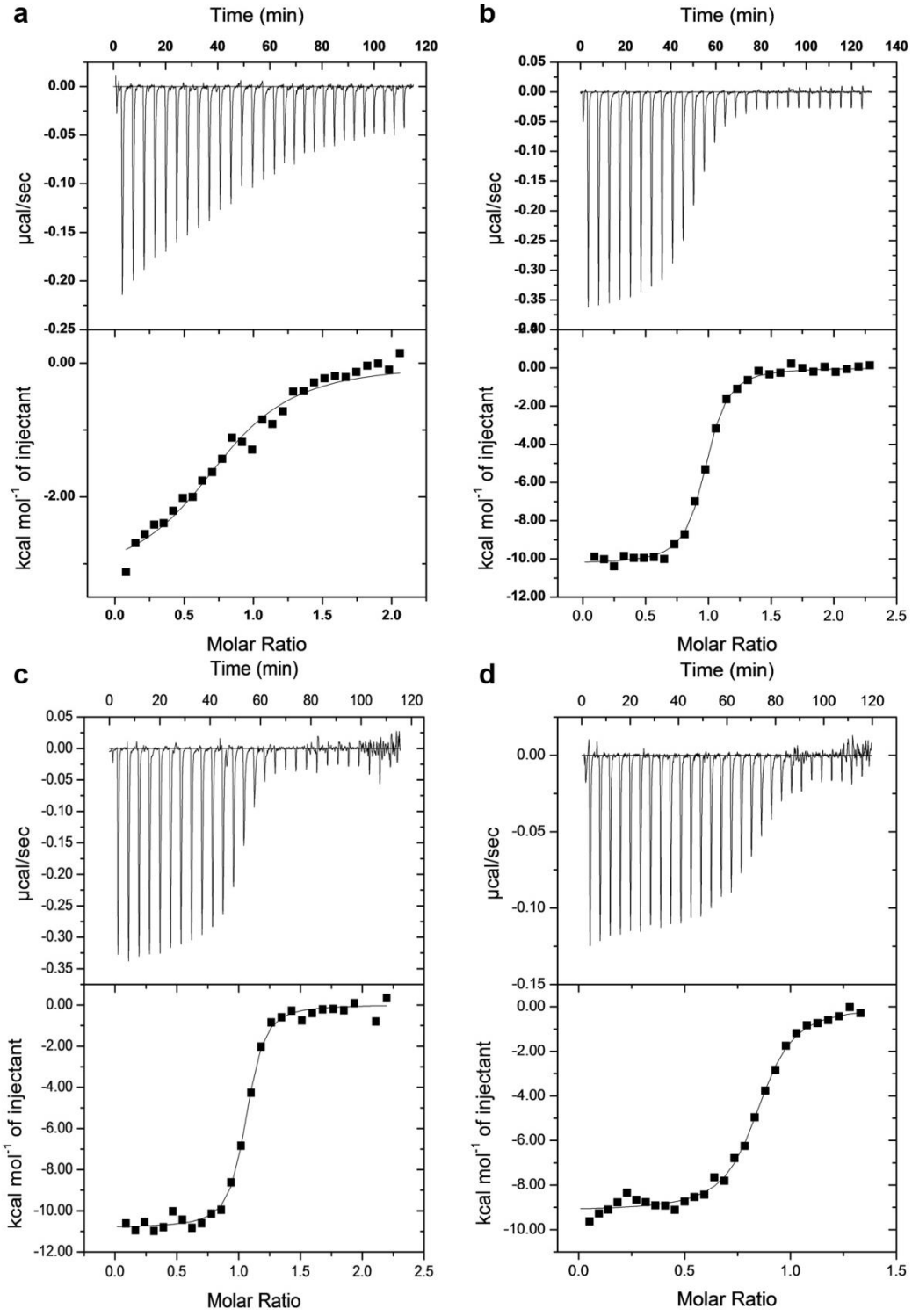

Figure 45 – a) ITC titration of 140 µM Ca^{2+}-N-lobe into 14 µM CNBhD-BDC1-BDC2. b) ITC titration of 100 µM Ca^{2+}-C-lobe into 10 µM CNBhD-BDC1-BDC2. c) ITC titration of 100 µM Ca^{2+}-CaM EF12 mutant into 100 µM CNBhD-BDC1-BDC2 (direct). d) ITC titration of 40 µM CNBhD-BDC1-BDC2 into 6 µM Ca^{2+}-CaM EF12 mutant (reverse).

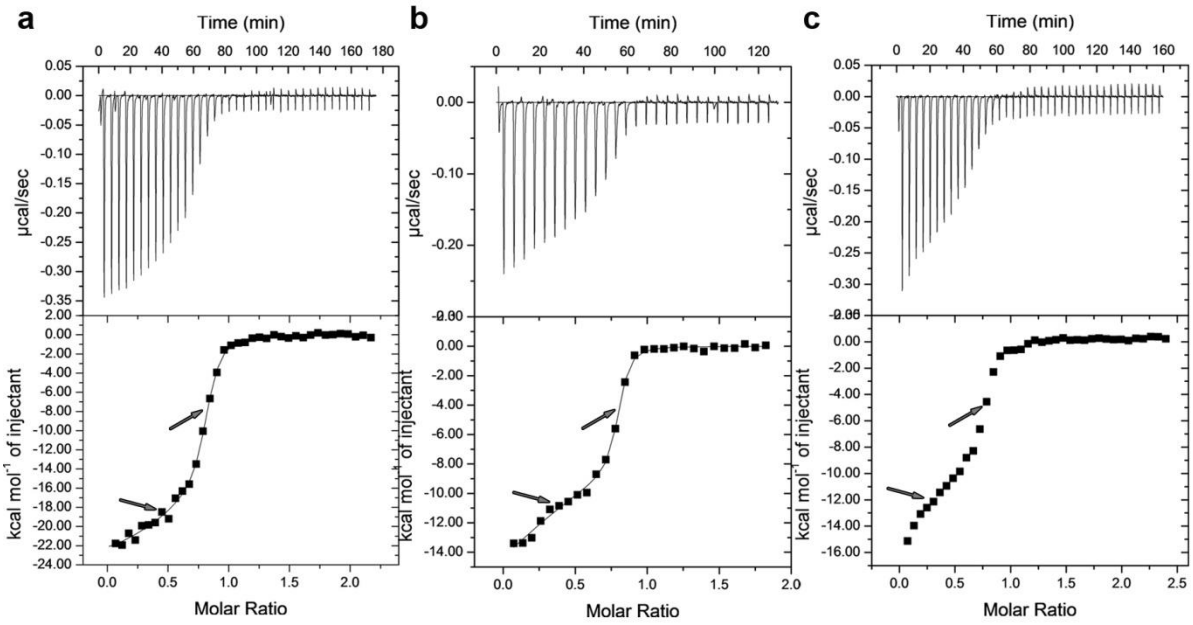

Figure 46 – a) ITC titration of 60 µM Ca^{2+}-CaM into 6 µM CNBhD-BDC1-BDC2 BDC1 mutant R702N/R704N/R708N/K709N. b) ITC titration of 60 µM Ca^{2+}-CaM into 6 µM MBP-BDC1-BDC2. c) ITC titration of 70 µM Ca^{2+}-CaM into 6 µM MBP-mEAG1 712-764. Arrows point towards the two steps in the binding isotherms.

Thus, with the help of Dr. Eva Muñoz from AFFINImeter (www.affinimeter.com), we fitted the CNBhD-BDC1-BDC2/CaM data to an independent site model that allows the extraction of site-specific binding constants, using this online isothermal titration calorimetry software. In this model, CaM is considered a two-site receptor, where the N- and C-lobe bind separately and independently to the channel fragment, as shown in Figure 47.

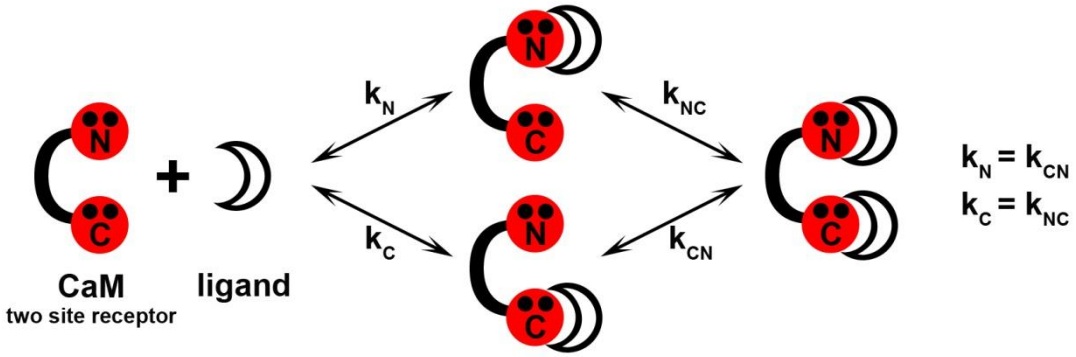

Figure 47 – Diagram of the binding equilibrium between CaM (two site receptor) and CNBhD-BDC1-BDC2 (ligand) using an independent site approach. k represents the binding site constants to each lobe (N- or C-), that are converted into K_Ds.

The fit of the data was very good (Figure 48a) and shows that there is an event with low affinity and low enthalpy (K_D = 1.3 ± 0.1 µM and ΔH = -4.25 ± 0.17 kcal/mol) and a second event with high affinity and high enthalpy (K_D = 6.5 ± 0.5 nM and ΔH = -14.27 ± 0.22 kcal/mol). Importantly, these thermodynamic parameters are in good agreement with the ones obtained for the titrations of the N- and C-lobe, respectively (Figure 45 a and b, Table 9). The species distribution plot (Figure 48b) shows the formation of two species throughout the titration: at the beginning of the titration, while there is excess of the CNBhD-BDC1-BDC2 (ligand), both lobes bind to the ligand. As the molar ratio of CaM:ligand approaches 1 and the availability of free CNBhD-BDC1-BDC2 drops, the higher affinity C-lobe displaces the N-lobe and by the end of the titration all CNBhD-BDC1-BDC2 is bound to the C-lobe.

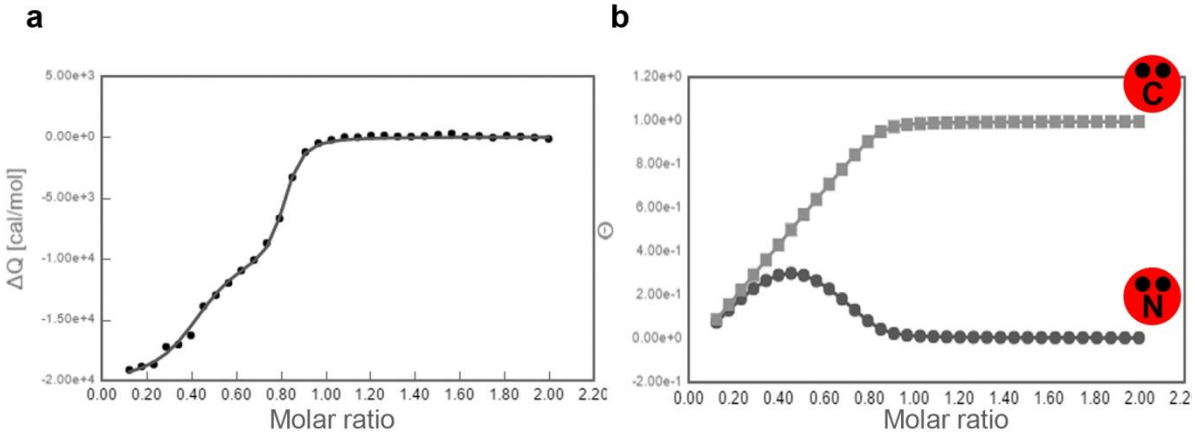

Figure 48 – a) ITC titration of 187 µM Ca^{2+}-CaM into 17 µM CNBhD-BDC1-BDC2 (same as Figure 44a) fitted with an independent site model using the software AFFINImeter. b) Species distribution plot that represents the fraction of lobes bound throughout the course of the titration.

To show that the lobes compete for the same binding sequence and confirm this model, we designed a displacement experiment. In this experiment, a mixture of CNBhD-BDC1-BDC2 pre-mixed with a saturating concentration of N-lobe was titrated with C-lobe. This titration shows a single transition (Figure 49). Fit to the single-site model provided by the Origin software, gives us an apparent K_D for C-lobe between 230-400 nM, and an apparent ΔH around -6 kcal/mol. The affinity drop and change in enthalpy in the presence of N-lobe shows that both lobes compete for the same site in CNBhD-BDC1-BDC2. Inputting the concentration and binding parameters determined for the N-lobe into a competition model gave us back thermodynamic parameters that are similar to the ones determined from the C-lobe direct titrations (K_D ~ 6.6 nM and ΔH ~ -16 kcal/mol, Figure

50a and b). The species distribution plot shows that with these concentrations, the C-lobe was able to compete out all the N-lobe.

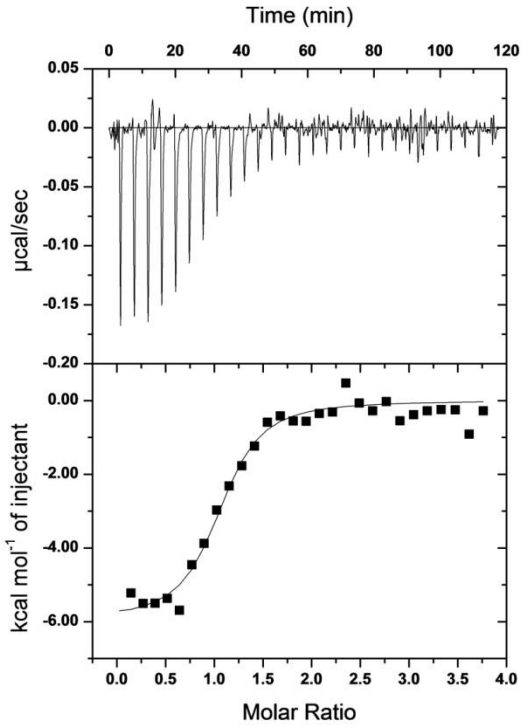

Figure 49 – ITC titration of 100 µM Ca^{2+}-C-lobe into 7 µM CNBhD-BDC1-BDC2 and 35 µM Ca^{2+}-N-lobe

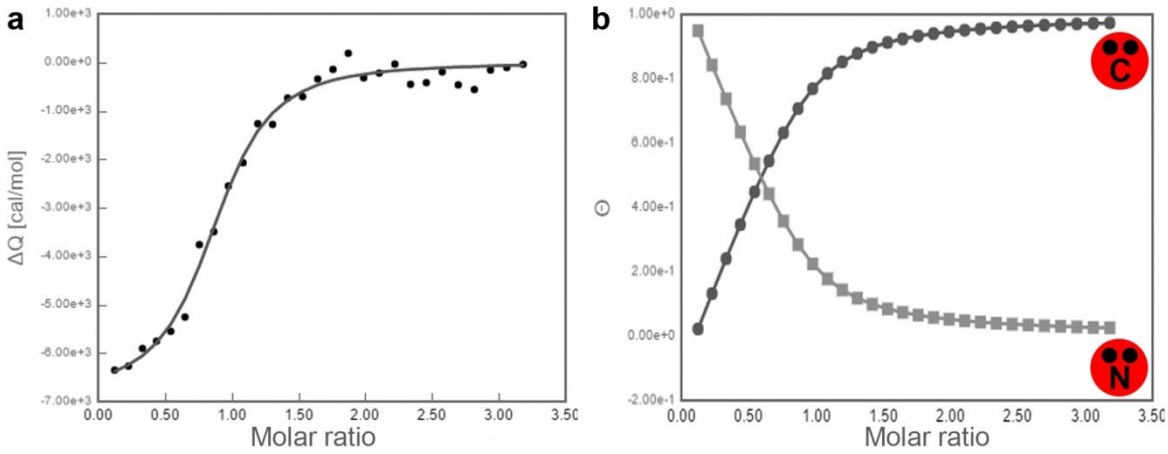

Figure 50 - a) ITC titration of 100 µM Ca^{2+}-C-lobe into 7 µM CNBhD-BDC1-BDC2 and 35 µM Ca^{2+}-N-lobe (same as Figure 49) fitted with an independent site model using the software AFFINImeter. b) Species distribution plot that represents the fraction of lobes bound throughout the course of the titration.

This model implies that reversing the titration (i.e., injecting the ligand into the two-site receptor CaM), will benefit the formation of the C-lobe complex that has higher affinity and more negative enthalpy of binding. N-lobe/channel complex will only start to form at molar ratios above 1, after all the C-lobe is saturated (Figure 51b).

A simulation of this titration, entering the binding parameters of the single lobes towards CNBhD-BDC1-BDC2 (Table 9) into the independent site model, reveals a single transition as can be seen in Figure 51a. This simulated curve is different from what we observed for the CNBhD-BDC1-BDC2 reverse titration (Figure 44b) because that protein fragment is heterogeneous at the high concentrations needed for the reverse titration, as evidenced by native mass spectrometry.

We performed reverse titrations using both extended BDC2 fusions and both of them displayed a single transition with parameters resemble the C-lobe's: K_D of 13.8 ± 2.2 nM, ΔH = 9.75 ± 1.06 kcal/mol for BDC1-BDC2 (Figure 52a) and K_D of 76.1 ± 1.0 nM, ΔH = 9.46 ± 1.47 kcal/mol for mEAG1 712-764 (Figure 52b). The plateau at the beginning and end of the titration is not symmetric: at the end, the reaction heats take longer to reach the baseline due to the contribution of the N-lobe small heats of binding, as can be followed on Figure 51b.

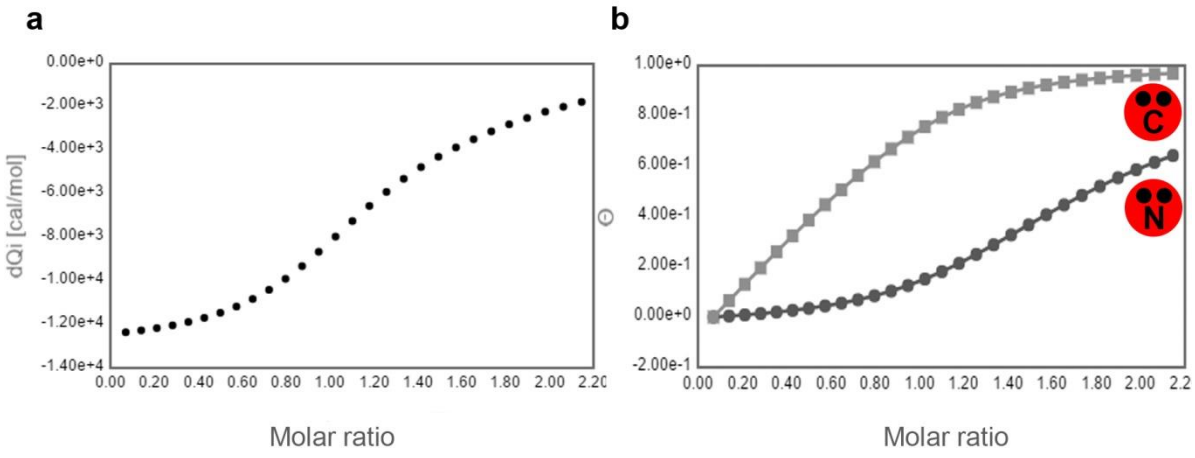

Figure 51 – a) Simulated binding isotherm for reverse titration CNBhD-BDC1-BDC2 into CaM using the concentrations from figure 44b and. b) species distribution plot of the species formed during the titration.

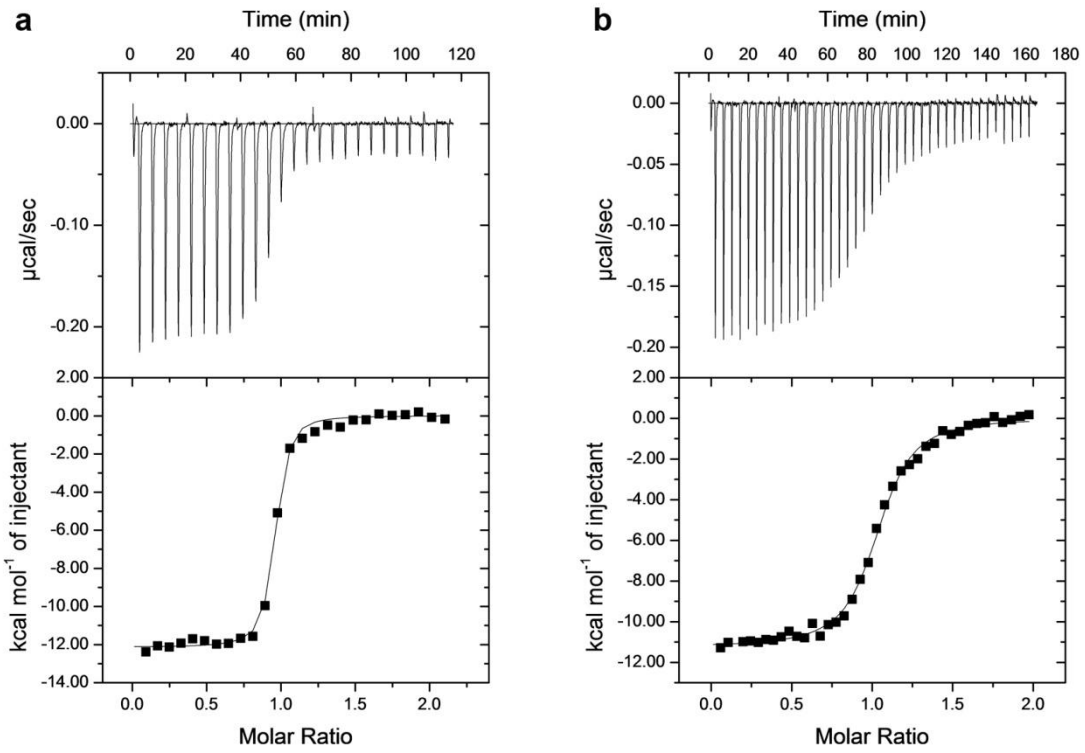

Figure 52- a) ITC titration of 60 µM MBP-BDC1-BDC2 into 6 µM Ca^{2+}-CaM. B) ITC titration of 70 µM MBP-mEAG1 712-764 into 7 µM Ca^{2+}-CaM.

Table 9 - Thermodynamic parameters for CaM interaction with protein fragments containing BDC1-BDC2.

CaM BD	Titrant	Cell	N	K_D (nM)	ΔH (kcal mol^{-1})	ΔS (cal mol^{-1} deg^{-1})	n
BDC1-BDC2	Ca^{2+}-CaM	CNBhD-BDC1-BDC2	0.76 ± 0.02	$1.3x10^3$ ± $0.1x10^3$ 6.5 ± 0.5	-4.25 ± 0.17 -14.27 ± 0.22	ND	7
	Ca^{2+}/N-lobe	CNBhD-BDC1-BDC2	0.80 ± 0.03	$1.3x10^3$ ± $0.1x10^3$	-4.43 ± 0.09	12.2 ± 0.5	3
	Ca^{2+}/C-lobe	CNBhD-BDC1-BDC2	0.80 ± 0.02	75.0 ± 8.4	-13.13 ± 0.26	-11.4 ± 0.9	3
	Ca^{2+}-CaM EF12 mut	CNBhD-BDC1-BDC2	0.94 ± 0.03	38.8 ± 4.4	-10.36 ± 0.32	0.7 ± 0.9	3
	CNBhD-BDC1-BDC2	Ca^{2+}-CaM EF12 mut	1.20	62.5	-7.65	7.3	1
	Ca^{2+}-CaM	MBP-BDC1-BDC2	ND	ND	ND	ND	3
	MBP-BDC1-BDC2	Ca^{2+}-CaM	1.13 ± 0.03	13.8 ± 2.2	-9.75 ± 1.06	3.3 ± 3.2	2
	Ca^{2+}-CaM	MBP-end of BDC1-BDC2	ND	ND	ND	ND	2
	MBP-end of BDC1-BDC2	Ca^{2+}-CaM	0.99 ± 0.01	76.1 ± 1.0	-9.46 ± 1.47	0.9 ± 4.9	2
	Ca^{2+}-CaM	CNBhD-mut BDC1-BDC2	ND	ND	ND	ND	3
	Ca^{2+}/C-lobe	CNBhD-BDC1-BDC2 + Ca^{2+}/N-lobe	ND	11.1 ± 3.2	-14.25 ± 1.25	ND	2

DISCUSSION

It was almost two decades ago that the inhibition of EAG1 currents by Ca^{2+} was described for the first time (Stansfeld et al. 1996). This process is mediated by CaM binding to the channel (Schönherr et al. 2000; Ziechner et al. 2006) and three sites for CaM binding were identified: one in the N terminus (BDN), after the PAS domain, and two on the C terminus (BDC1 and BDC2) after the CNB-homology domain. Mutations in each of these sites severely affected Ca^{2+}-CaM inhibition (Ziechner et al. 2006) suggesting that all sites were important. However, the affinity of CaM for the BDC1 site is not consensual and the functional relevance of this site has been questioned (Gonçalves & Stühmer 2010; Marques-Carvalho et al. 2012). As to this date, the molecular mechanism of inhibition of EAG1 channels by Ca^{2+}-CaM is not fully understood.

Using a combination of isothermal titration calorimetry and X-ray crystallography, we characterized the binding of calmodulin to several channel fragments encompassing the calmodulin binding sequences BDN, BDC1 and BDC2. We also assessed the contribution of the individual CaM lobes and evaluated the effect of the PAS and CNB-homology domains on CaM binding to these sites.

CaM has high affinity for CaM BDC1, an interaction that is entropically driven. The presence of the CNB-homology domain drastically lowers the affinity of CaM for BDC1 due to a decrease in the entropy of the system. The low affinity of BDC1 agrees with the observation that this site is occluded in the PAS/CNB-homology domain structure (Haitin et al. 2013b), which is consistent with a reduced conformational freedom (entropy). Our data shows that mutations in the BDC1 region that lower CaM's affinity (Marques-Carvalho et al. 2012) and make EAG1 channels nearly insensitive to Ca^{2+}-CaM (Ziechner et al. 2006), disrupt the interaction of the CNB-homology domain with the PAS domain. Altogether, the data available on the BDC1 region leads us to propose that, with a K_D in the micromolar range, BDC1 is not important for CaM inhibition, a process that has an IC_{50} ~ 6 nM for CaM. BDC1 might instead have a different regulatory role through the interaction with the PAS domain.

We also demonstrated that CaM binds to BDN with high affinity using both lobes, in a Ca^{2+}-dependent fashion. The presence of the PAS domain slightly lowers the affinity of CaM for BDN. The interaction of CaM with PAS-BDN has a more negative enthalpy change which is accompanied by an increase in the order of the system, suggesting that CaM might also interact with the surface of the PAS domain.

Interestingly, CaM binds to BDC2 in a non-canonical manner – the C-lobe has a much higher affinity for BDC2 than the N-lobe. The structure of the CaM/BDC2 complex shows that CaM is in an elongated conformation, with the C-lobe interacting with the channel sequence and the N-lobe without Ca^{2+}. The observation that the N-lobe does not contain any Ca^{2+} bound is most likely related to not being engaged in this interaction. The BDC2 peptide is bent, with an extended conformation at the N terminus before turning into a small α-helix. It includes residues that had not been previously described to be involved in binding to CaM. Mutations in the extended N-terminal stretch that decreased the CaM affinity also decreased Ca^{2+} sensitivity of full-length channels, supporting the importance of these residues for CaM modulation. The C-terminal part of the peptide is disordered in our structure, despite including residues that are important for CaM binding (Schönherr et al. 2000). This can be attributed to crystal packing restraints, since there is a symmetry related peptide in close proximity. The bent conformation of the peptide is unusual and may result from the positioning of BDC2 in a groove formed by the C-lobe of one CaM and the N-lobe of a symmetry related CaM, making interactions with both. While the physiological relevance of the bend is not clear, channels with mutations aimed at disrupting intra-peptide interactions at the bend were less sensitive to Ca^{2+}, leading us to suggest that the bend is important for this mechanism. It is not known how CaM binding results in channel inhibition but a possibility is that the bend formation could be a part of the gating mechanism, by introducing rearrangements in the disposition of the channel's cytoplasmic domains that would lead to channel closure.

Finally, we observed that CaM binding to a longer channel fragment that includes CNB-homology domain, BDC1 and BDC2 exhibits an isotherm with two slopes. We established that this interaction is also dominated by the C-lobe, but that the Ca^{2}-N-lobe is involved in this behavior. These binding isotherms could only be explained if CaM was described as having two independent binding sites for this region - its individual N- and C-lobes. We were able to show that both lobes bind in a competitive manner to the same residue stretch, with parameters that resemble the titrations with the single lobes. We narrowed down the region to which both lobes bind to a stretch that starts after the BDC1 and extends to BDC2, reinforcing the observation that residues between BDC1 and the previously described BDC2 sequence are also important for this CaM binding. With this new knowledge, a subtle bump at the beginning of the CaM into BDC2 titration could also be detected upon a closer look, although much less accentuated than when the protein is extended towards the N-terminal. This feature is more subtle given that the heats associated with binding of the N-lobe to BDC2 are lower. Because of this, fit to the independent sites model was not successful, but it explains the difference in enthalpies for

direct and reverse titration observed for BDC2. Consistent with the competitive model, reverse titrations of the extended BDC2 peptides into CaM revealed a single transition, with binding parameters that are close to the C-lobe's. At the start of the titration, CaM is in excess and the equilibrium is shifted towards the more enthapically driven, higher affinity interaction (C-lobe/channel fragment). Species of N-lobe/channel fragment only start to form after all the C-lobe is saturated (at molar ratios above 1). The reverse titration of CNBhD-BDC1-BDC2 into CaM displayed a more complicated behavior because of the heterogeneity of the sample at high concentrations.

In summary, we have established that each EAG1 CaM binding site has very distinct CaM binding properties and that the affinity towards CaM is affected by the presence of the globular domains PAS and CNB-homology domain.

V. CONCLUDING REMARKS

The work described in this dissertation represents a structural, biochemical and biophysical characterization of the cytoplasmic regions of the EAG1 channels, focusing on their interaction with calmodulin.

KCNH channels contain large cytoplasmic regions on the N- and C-terminal that are involved in channel gating. It has been well established that the PAS domain interacts with the CNB-homology domain in KCNH channels (Gustina & Trudeau 2013; Haitin et al. 2013b) and that this interaction is important for the channel's gating properties.

Structures of KCNH CNB-homology domains showed a self-liganded conformation with an intrinsic ligand bound in the pocket. The C-terminal tail of the mEAG1 CNB-homology domain includes a previously identified CaM binding sequence (BDC1) that does not exist in the other KCNH channel subfamilies. This region is partially occluded as a result of the self-liganded state and is also part of the interface of the PAS/CNB-homology domain complex (Haitin et al. 2013b). We explored the existence of an unliganded conformation, making use of CaM as well as by introducing mutations that destabilize the self-liganded conformation. We showed that CaM BDC1 is a weak binding site for CaM and that mutations that released the C-terminal tail resulted in higher affinities towards CaM. We also demonstrated that CaM binding causes structural changes in the CNB-homology domain, suggesting that the C-terminal tail peels away from the surface of the domain. Mutations in the intrinsic ligand affected the voltage-dependence of EAG1 channels, suggesting that the CNB-homology domain has a role in channel gating. A possibility is

that the effect of the intrinsic ligand mutations is related to the destabilization of the PAS/CNB-homology domain complex. However, the role of the individual intrinsic ligand residues is not understood since opposite effects are found among different KCNH subfamilies.

Using ITC, we performed a comprehensive characterization of CaM binding to the EAG1 CaM binding sequences and evaluated the effect of the globular domains PAS and CNB-homology domain on this interaction. We propose that BDC1 is not important for CaM modulation and that the effect that BDC1 mutations have on Ca^{2+}-CaM inhibition is due to the destabilization of the complex between PAS and CNB-homology domain. CaM binds to BDN in a Ca^{2+}-dependent manner, involving both lobes and it might also interact with the surface of the PAS domain. CaM BDC2 site shows a non-canonical binding mode to CaM, involving mainly the C-lobe, with little contribution from the N-lobe. Channel fragments that included BDC2 and were extended towards the N terminus showed complicated binding isotherms to CaM which could not be explained with a simple 1:1 model. Using a combination of ITC, structural data and electrophysiology we have redefined the limits of the BDC2 site. The extended site spans from the end of BDC1, until the end of the previously identified BDC2. CaM binds to this region using both lobes independently and competitively, with different K_Ds and ΔH, with the C-lobe binding tighter than the N-lobe.

It is easy to imagine that there is a very high local concentration of CaM binding sites below the EAG1 pore, given that the EAG1 channel is tetrameric, with large cytoplasmic regions that include more than one site for CaM binding per subunit. An implication of the weak binding of the N-lobe to the C terminus of the channel is that it is free to engage with other parts of the channel, BDN or a CaM binding site from a neighbor subunit, for instance.

The lack of CaM inhibition of channels with the entire N terminus deleted or channels with mutations on BDC1 (Ziechner et al. 2006), together with new data on the PAS/CNB-homology domain complex stability seem to suggest that the integrity of this complex is necessary for Ca^{2+}-CaM to exert its inhibitory function. It is possible that this complex is required to bring together certain channel regions, important for CaM modulation.

All the functional analysis on Ca^{2+}-CaM inhibition of EAG1 was performed at constant voltage and it would be very interesting to study if this process is voltage-dependent. Moreover, it would be of great interest to evaluate whether CaM induces conformational changes on the EAG1 globular domains. Extensive crystallization attempts were made of complexes between CaM and different sized CaM binding peptides, as well as with CNB-

homology domain or PAS-containing fragments but no crystals of the complexes were ever obtained, apart from CaM/BDC2. The high solubility and flexibility of CaM might underlie the low success rate, so it would be interesting to explore this further using another structural biology technique like NMR.

The present work has provided more detailed insights into binding of CaM to EAG1 cytoplasmic regions but we are far from understanding the molecular mechanisms of EAG1 channel inhibition by Ca^{2+}-CaM.

VI. REFERENCES

Adaixo, R. et al., 2013. Structural properties of PAS domains from the KCNH potassium channels. *PloS one*, 8(3), p.e59265. Available at: http://www.pubmedcentral.nih.gov/articlerender.fcgi?artid=3598652&tool=pmcentrez&rendertype=abstract [Accessed June 18, 2013].

Adams, P.D. et al., 2010. PHENIX: a comprehensive Python-based system for macromolecular structure solution. *Acta crystallographica. Section D, Biological crystallography*, 66(Pt 2), pp.213–21. Available at: http://www.pubmedcentral.nih.gov/articlerender.fcgi?artid=2815670&tool=pmcentrez&rendertype=abstract [Accessed October 4, 2010].

Adams, P.J. et al., 2014. Apocalmodulin Itself Promotes Ion Channel Opening and Ca 2 + Regulation. *Cell*, 159(3), pp.608–622. Available at: http://dx.doi.org/10.1016/j.cell.2014.09.047.

Adelman, J.P., 2015. SK Channels and Calmodulin. *Channels*, (May), pp.00–00. Available at: http://www.tandfonline.com/doi/full/10.1080/19336950.2015.1029688.

Aggarwal, S.K. & MacKinnon, R., 1996. Contribution of the S4 segment to gating charge in the Shaker K+ channel. *Neuron*, 16(6), pp.1169–77. Available at: http://www.ncbi.nlm.nih.gov/pubmed/8663993.

Alaimo, A. et al., 2014. Pivoting between calmodulin lobes triggered by calcium in the Kv7.2/calmodulin complex. *PloS one*, 9(1), p.e86711. Available at: http://www.pubmedcentral.nih.gov/articlerender.fcgi?artid=3904923&tool=pmcentrez&rendertype=abstract [Accessed May 4, 2014].

Altieri, S.L. et al., 2008. Structural and energetic analysis of activation by a cyclic nucleotide binding domain. *Journal of molecular biology*, 381(3), pp.655–69. Available at: http://www.ncbi.nlm.nih.gov/pubmed/18619611.

Bauer, C.K. & Schwarz, J.R., 2001. Physiology of EAG K+ channels. *The Journal of membrane biology*, 182(1), pp.1–15. Available at: http://www.ncbi.nlm.nih.gov/pubmed/11426295 [Accessed August 2, 2010].

Bax, A., 1994. Multidimensional nuclear magnetic resonance methods for protein studies. *Current opinion in structural biology*, 4, pp.738–744.

Becchetti, A. et al., 2002. The functional properties of the human ether-à-go-go-like (HELK2) K+ channel. *European Journal of Neuroscience*, 16(3), pp.415–428. Available at: http://doi.wiley.com/10.1046/j.1460-9568.2002.02079.x [Accessed March 19, 2012].

Ben-Johny, M. et al., 2014. Conservation of Ca2+/calmodulin regulation across Na and Ca 2+ channels. *Cell*, 157(7), pp.1657–1670.

Ben-Johny, M. & Yue, D.T., 2014. Calmodulin regulation (calmodulation) of voltage-gated calcium channels. *The Journal of General Physiology*, 143(6), pp.679–692. Available at: http://www.jgp.org/cgi/doi/10.1085/jgp.201311153.

Brelidze, T.I. et al., 2012. Structure of the carboxy-terminal region of a KCNH channel. *Nature*, 481(7382), pp.530–533. Available at: http://www.nature.com/doifinder/10.1038/nature10735 [Accessed January 10, 2012].

Brelidze, T.I. et al., 2013. Structure of the C-terminal region of an ERG channel and functional implications. *Proceedings of the National Academy of Sciences of the United States of America*, 110(28), pp.11648–53. Available at: http://www.ncbi.nlm.nih.gov/pubmed/23801759 [Accessed September 13, 2013].

Brelidze, T.I., Carlson, A.E. & Zagotta, W.N., 2009. Absence of direct cyclic nucleotide modulation of mEAG1 and hERG1 channels revealed with fluorescence and electrophysiological methods. *The Journal of biological chemistry*, 284(41), pp.27989–97. Available at: http://www.pubmedcentral.nih.gov/articlerender.fcgi?artid=2788851&tool=pmcentrez&rendertype=abstract [Accessed July 31, 2010].

Cadene, M. & Chait, B.T., 2000. A robust, detergent-friendly method for mass spectrometric analysis of integral membrane proteins. *Analytical chemistry*, 72(22), pp.5655–8. Available at: http://www.ncbi.nlm.nih.gov/pubmed/11101244.

Carlson, A.E., Brelidze, T.I. & Zagotta, W.N., 2013. Flavonoid regulation of EAG1 channels. *The Journal of general physiology*, 141(3), pp.347–58. Available at: http://www.ncbi.nlm.nih.gov/pubmed/23440277 [Accessed June 27, 2013].

Catterall, W.A., 2011. Voltage-Gated Calcium Channels.

Cherubini, A. et al., 2005. Human ether-a-go-go-related Gene 1 Channels Are Physically Linked to ¹ 1 Integrins and Modulate Adhesion-dependent Signaling. *Molecular Biology of the Cell*, 16(June), pp.2972–2983.

Clayton, G.M. et al., 2004. Structural basis of ligand activation in a cyclic nucleotide regulated potassium channel. *Cell*, 119(5), pp.615–27. Available at: http://www.ncbi.nlm.nih.gov/pubmed/15550244 [Accessed August 2, 2010].

Craven, K.B. & Zagotta, W.N., 2006. CNG and HCN channels: two peas, one pod. *Annual review of physiology*, 68, pp.375–401. Available at: http://www.ncbi.nlm.nih.gov/pubmed/16460277 [Accessed July 22, 2010].

Crociani, O. et al., 2003. Cell cycle-dependent expression of HERG1 and HERG1B isoforms in tumor cells. *Journal of Biological Chemistry*, 278(5), pp.2947–2955.

Delaglio, F. et al., 1995. NMRPipe: A multidimensional spectral processing system based on UNIX pipes. *Journal of Biomolecular NMR*, 6(3), pp.277–293.

DeLano, W.L., 2002. The PyMOL Molecular Graphics System, Schrödinger, LLC. Available at: www.pymol.org.

Doyle, D.A. et al., 1998. The structure of the potassium channel: molecular basis of K+ conduction and selectivity. *Science (New York, N.Y.)*, 280(5360), pp.69–77. Available at: http://www.ncbi.nlm.nih.gov/pubmed/9525859 [Accessed August 2, 2010].

Emsley, P. & Cowtan, K., 2004. Coot: model-building tools for molecular graphics. *Acta crystallographica. Section D, Biological crystallography*, 60(Pt 12 Pt 1), pp.2126–32. Available at: http://www.ncbi.nlm.nih.gov/pubmed/15572765.

Evans, P.R. & Murshudov, G.N., 2013. How good are my data and what is the resolution? *Acta Crystallographica Section D: Biological Crystallography*, 69, pp.1204–1214.

Farmer, B.T. et al., 1996. Localizing the NADP+ binding site on the MurB enzyme by NMR. *Nat Struct Mol Biol*, 3(12), pp.995–997. Available at: http://dx.doi.org/10.1038/nsb1296-995.

Gabant, G. & Cadene, M., 2008. Mass spectrometry of full-length integral membrane proteins to define functionally relevant structural features. *Methods (San Diego, Calif.)*, 46(2), pp.54–61. Available at: http://www.ncbi.nlm.nih.gov/pubmed/18976710 [Accessed August 21, 2010].

Gianulis, E.C., Liu, Q. & Trudeau, M.C., 2013. Direct interaction of eag domains and cyclic nucleotide-binding homology domains regulate deactivation gating in hERG channels. *The Journal of general physiology*, 142(4), pp.351–66. Available at: http://www.ncbi.nlm.nih.gov/pubmed/24043860.

Gonçalves, J.T. & Stühmer, W., 2010. Calmodulin interaction with hEAG1 visualized by FRET microscopy. *PloS one*, 5(5), p.e10873. Available at: http://www.pubmedcentral.nih.gov/articlerender.fcgi?artid=2877719&tool=pmcentrez&rendertype=abstract [Accessed July 31, 2010].

Gustina, A.S. & Trudeau, M.C., 2013. The eag domain regulates hERG channel inactivation gating via a direct interaction. *The Journal of general physiology*, 141(2), pp.229–41. Available at: http://www.pubmedcentral.nih.gov/articlerender.fcgi?artid=3557309&tool=pmcentrez&rendertype=abstract [Accessed September 12, 2013].

Haitin, Y., Carlson, A.E. & Zagotta, W.N., 2013a. The structural mechanism of KCNH-channel regulation by the eag domain SUPP. *Nature*, 1, pp.1–10. Available at: http://www.ncbi.nlm.nih.gov/pubmed/23975098 [Accessed August 29, 2013].

Haitin, Y., Carlson, A.E. & Zagotta, W.N., 2013b. The structural mechanism of KCNH-channel regulation by the eag domain. *Nature*, 501(7467), pp.444–8. Available at: 10.1038/nature12487.

Heck, A.J.R., 2008. Native mass spectrometry: a bridge between interactomics and structural biology. *Nature methods*, 5(11), pp.927–933.

Henry, J.T. & Crosson, S., 2011. Ligand-Binding PAS Domains in a Genomic, Cellular, and Structural Context. *Annual Review of Microbiology*, 65(1), pp.261–286.

Hidalgo, P. & MacKinnon, R., 1995. Revealing the architecture of a K+ channel pore through mutant cycles with a peptide inhibitor. *Science (New York, N.Y.)*, 268(5208), pp.307–310.

Hodgkin, A.L. & Keynes, R.D., 1955. The potassium permeability of a giant nerve fibre. *The Journal of physiology*, 128(1), pp.61–88.

Holmgren, M., Smith, P.L. & Yellen, G., 1997. Trapping of organic blockers by closing of voltage-dependent K+ channels: evidence for a trap door mechanism of activation gating. *The Journal of general physiology*, 109(5), pp.527–35. Available at: http://www.pubmedcentral.nih.gov/articlerender.fcgi?artid=2217058&tool=pmcentrez&rendertype=abstract.

Kabsch, W., 2010. Integration, scaling, space-group assignment and post-refinement. *Acta Crystallographica Section D: Biological Crystallography*, 66, pp.133–144.

Kaupp, U.B. & Seifert, R., 2002. Cyclic nucleotide-gated ion channels. *Physiological reviews*, 82(3), pp.769–824. Available at: http://www.ncbi.nlm.nih.gov/pubmed/20729090.

Kim, D., McCoy, J. & Nimigean, C., 2015. Ion selectivity and conductance. In *Handbook of Ion Channels*. CRC Press, pp. 13–24. Available at: http://dx.doi.org/10.1201/b18027-4.

Kim, E.Y. et al., 2010. Multiple C-terminal tail Ca(2+)/CaMs regulate Ca(V)1.2 function but do not mediate channel dimerization. *The EMBO journal*, 29(23), pp.3924–38. Available at: http://www.pubmedcentral.nih.gov/articlerender.fcgi?artid=3020648&tool=pmcentrez&rendertype=abstract [Accessed January 31, 2011].

Kincaid, R.L. et al., 1982. Ca2+-dependent interaction of 5-dimethylaminonaphthalene-1-sulfonyl-calmodulin with cyclic nucleotide phosphodiesterase, calcineurin, and troponin I. *The Journal of biological chemistry*, 257(18), pp.10638–43. Available at: http://www.ncbi.nlm.nih.gov/pubmed/6286665.

Kincaid, R.L., Billingsley, M.L. & Vaughan, M., 1988. Preparation of fluorescent, cross-linking, and biotinylated calmodulin derivatives and their use in studies of calmodulin-activated phosphodiesterase and protein phosphatase. *Methods in enzymology*, 159, pp.605–26. Available at: http://www.ncbi.nlm.nih.gov/pubmed/2842624.

Krissinel, E. & Henrick, K., 2007. Inference of Macromolecular Assemblies from Crystalline State. *Journal of Molecular Biology*, 372(3), pp.774–797.

Li, Q. et al., 2010. NMR solution structure of the N-terminal domain of hERG and its interaction with the S4-S5 linker. *Biochemical and Biophysical Research Communications*, 403(1), pp.126–132. Available at: http://dx.doi.org/10.1016/j.bbrc.2010.10.132.

Li, Q. et al., 2014. Structural mechanism of voltage-dependent gating in an isolated voltage-sensing domain. *Nature structural & molecular biology*, 21(3), pp.244–52. Available at: http://www.ncbi.nlm.nih.gov/pubmed/24487958.

Liu, Y. et al., 1997. Gated access to the pore of a voltage-dependent K+ channel. *Neuron*, 19(1), pp.175–84. Available at: http://www.ncbi.nlm.nih.gov/pubmed/9247273.

Long, S.B., Campbell, E.B. & Mackinnon, R., 2005. Crystal structure of a mammalian voltage-dependent Shaker family K+ channel. *Science (New York, N.Y.)*, 309(5736), pp.897–903.

Lu, J. & Deutsch, C., 2001. Pegylation: a method for assessing topological accessibilities in Kv1.3. *Biochemistry*, 40(44), pp.13288–301. Available at: http://www.ncbi.nlm.nih.gov/pubmed/11683639.

MacKinnon, R., 2003. Potassium channels. *FEBS Letters*, 555(1), pp.62–65. Available at: http://linkinghub.elsevier.com/retrieve/pii/S0014579303011049.

MacKinnon, R., 2004. Potassium channels and the atomic basis of selective ion conduction (Nobel Lecture). *Angewandte Chemie (International ed. in English)*, 43(33), pp.4265–77. Available at: http://www.ncbi.nlm.nih.gov/pubmed/15368373.

Marques Carvalho, M.J. et al., 2012. Structural and Biochemical Characterization of a Cyclic Nucleotide Binding Domain from the EAG Family. *Biophysical Journal*, 102(3), p.330a. Available at: http://linkinghub.elsevier.com/retrieve/pii/S0006349511031572 [Accessed June 22, 2012].

Marques-Carvalho, M.J. et al., 2012. Structural, biochemical, and functional characterization of the cyclic nucleotide binding homology domain from the mouse EAG1 potassium channel. *Journal of molecular biology*, 423(1), pp.34–46. Available at: http://www.ncbi.nlm.nih.gov/pubmed/22732247 [Accessed January 9, 2014].

Marques-Carvalho, M.J. & Morais-Cabral, J.H., 2012. Crystallization and preliminary X-ray crystallographic characterization of a cyclic nucleotide-binding homology domain from the mouse EAG potassium channel. *Acta Crystallographica Section F Structural Biology and Crystallization Communications*, 68(3), pp.337–339. Available at: http://scripts.iucr.org/cgi-bin/paper?S1744309112004216 [Accessed March 14, 2012].

McCoy, A.J. et al., 2007. Phaser crystallographic software. *Journal of applied crystallography*, 40(Pt 4), pp.658–674. Available at: http://www.pubmedcentral.nih.gov/articlerender.fcgi?artid=2483472&tool=pmcentrez&rendertype=abstract [Accessed July 18, 2011].

Morais Cabral, J.H. et al., 1998. Crystal structure and functional analysis of the HERG potassium channel N terminus: a eukaryotic PAS domain. *Cell*, 95(5), pp.649–55. Available at: http://www.ncbi.nlm.nih.gov/pubmed/9845367 [Accessed July 31, 2010].

Morais-Cabral, J.H., Zhou, Y. & MacKinnon, R., 2001. Energetic optimization of ion conduction rate by the K+ selectivity filter. *Nature*, 414(6859), pp.37–42.

Mori, M.X., Erickson, M.G. & Yue, D.T., 2004. Functional stoichiometry and local enrichment of calmodulin interacting with Ca2+ channels. *Science (New York, N.Y.)*, 304(5669), pp.432–5. Available at: http://www.ncbi.nlm.nih.gov/pubmed/15087548 [Accessed April 7, 2011].

Mortensen, L.S. et al., 2015. K V 10.1 opposes activity-dependent increase in Ca 2+ influx into the presynaptic terminal of the parallel fibre-Purkinje cell synapse. *The Journal of Physiology*, 593(1), pp.181–196. Available at: http://doi.wiley.com/10.1113/jphysiol.2014.281600.

Mruk, K. et al., 2012. Structural insights into neuronal K+ channel-calmodulin complexes. *Proceedings of the National Academy of Sciences of the United States of America*, 109(34), pp.13579–83. Available at:

http://www.pubmedcentral.nih.gov/articlerender.fcgi?artid=3427091&tool=pmcentrez&rendertype=abstract [Accessed May 17, 2014].

Muskett, F.W. et al., 2011. Mechanistic insight into human ether-??-go-go-related gene (hERG) K + channel deactivation gating from the solution structure of the EAG domain. *Journal of Biological Chemistry*, 286(8), pp.6184–6191.

Ng, C.A. et al., 2011. The N-terminal tail of hERG contains an amphipathic ??-helix that regulates channel deactivation. *PLoS ONE*, 6(1).

Painter, J. & Merritt, E. a, 2006. Optimal description of a protein structure in terms of multiple groups undergoing TLS motion. *Acta crystallographica. Section D, Biological crystallography*, 62(Pt 4), pp.439–50. Available at: http://www.ncbi.nlm.nih.gov/pubmed/16552146.

Pardo, L. a & Stühmer, W., 2014. The roles of K(+) channels in cancer. *Nature reviews. Cancer*, 14(1), pp.39–48. Available at: http://www.ncbi.nlm.nih.gov/pubmed/24336491.

Pardo, L. a & Sühmer, W., 2008. Eag1 as a cancer target. *Expert opinion on therapeutic targets*, 12(7), pp.837–843. Available at: http://www.ncbi.nlm.nih.gov/pubmed/18554152 [Accessed June 20, 2012].

Persechini, A. & Stemmer, P.M., 2002. Calmodulin is a limiting factor in the cell. *Trends in Cardiovascular Medicine*, 12(1), pp.32–37.

Pervushin, K. et al., 1997. Attenuated T2 relaxation by mutual cancellation of dipole-dipole coupling and chemical shift anisotropy indicates an avenue to NMR structures of very large biological macromolecules in solution. *Proceedings of the National Academy of Sciences of the United States of America*, 94(23), pp.12366–12371.

Van Petegem, F., Chatelain, F.C. & Minor, D.L., 2005. Insights into voltage-gated calcium channel regulation from the structure of the CaV1.2 IQ domain-Ca2+/calmodulin complex. *Nature structural & molecular biology*, 12(12), pp.1108–15. Available at: http://www.ncbi.nlm.nih.gov/pubmed/16299511.

Ranganathan, R., Lewis, J.H. & MacKinnon, R., 1996. Spatial localization of the K+ channel selectivity filter by mutant cycle-based structure analysis. *Neuron*, 16(1), pp.131–9. Available at: http://www.ncbi.nlm.nih.gov/pubmed/8562077.

Rehmann, H., Wittinghofer, A. & Bos, J.L., 2007. Capturing cyclic nucleotides in action: snapshots from crystallographic studies. *Nature reviews. Molecular cell biology*, 8(1), pp.63–73. Available at: http://www.ncbi.nlm.nih.gov/pubmed/17183361 [Accessed July 31, 2010].

Rhoads, A.R. & Friedberg, F., 1997. Sequence motifs for calmodulin recognition. *The FASEB journal : official publication of the Federation of American Societies for Experimental Biology*, 11(5), pp.331–40. Available at: http://www.ncbi.nlm.nih.gov/pubmed/9141499 [Accessed November 11, 2010].

Sahoo, N. et al., 2010. Current inhibition of human EAG1 potassium channel by the Ca(2+) binding protein S100B. *FEBS letters*, (August), pp.1–5. Available at: http://www.ncbi.nlm.nih.gov/pubmed/20708613 [Accessed August 17, 2010].

Saimi, Y. & Kung, C., 2002. Calmodulin as an ion channel subunit. *Annual review of physiology*, 64, pp.289–311. Available at: http://www.ncbi.nlm.nih.gov/pubmed/11826271 [Accessed June 5, 2013].

Sarhan, M.F. et al., 2012. Crystallographic basis for calcium regulation of sodium channels. *Proceedings of the National Academy of Sciences of the United States of America*, 109(9), pp.3558–63. Available at: http://www.pubmedcentral.nih.gov/articlerender.fcgi?artid=3295267&tool=pmcentrez&rendertype=abstract [Accessed March 14, 2012].

Schönherr, R. et al., 1999. Individual subunits contribute independently to slow gating of bovine EAG potassium channels. *Journal of Biological Chemistry*, 274(9), pp.5362–5369.

Schönherr, R., Löber, K. & Heinemann, S.H., 2000. Inhibition of human ether à go-go potassium channels by Ca(2+)/calmodulin. *The EMBO journal*, 19(13), pp.3263–71. Available at: http://www.pubmedcentral.nih.gov/articlerender.fcgi?artid=313935&tool=pmcentrez&rendertype=abstract.

Schumacher, M. a et al., 2001. Structure of the gating domain of a Ca2+-activated K+ channel complexed with Ca2+/calmodulin. *Nature*, 410(6832), pp.1120–4. Available at: http://www.ncbi.nlm.nih.gov/pubmed/11323678.

Schumacher, M. a, Crum, M. & Miller, M.C., 2004. Crystal structures of apocalmodulin and an apocalmodulin/SK potassium channel gating domain complex. *Structure (London, England : 1993)*, 12(5), pp.849–60. Available at: http://www.ncbi.nlm.nih.gov/pubmed/15130477 [Accessed August 16, 2010].

Sharma, H. et al., 2009. Structure of apo-CAP reveals that large conformational changes are necessary for DNA binding. *Proceedings of the National Academy of Sciences of the United States of America*, 106(39), pp.16604–16609.

Sklenar, V. et al., 1993. Gradient-Tailored Water Suppression for 1H-15N HSQC Experiments Optimized to Retain Full Sensitivity. *Journal of Magnetic Resonance, Series A*, 102(2), pp.241–245.

Stansfeld, C.E. et al., 1996. Elevation of intracellular calcium by muscarinic receptor activation induces a block of voltage-activated rat ether-à-go-go channels in a stably transfected cell line. *Proceedings of the National Academy of Sciences of the United States of America*, 93(18), pp.9910–4. Available at: http://www.pubmedcentral.nih.gov/articlerender.fcgi?artid=38528&tool=pmcentrez&rendertype=abstract.

Strasburg, G.M. et al., 1988. Site-specific derivatives of wheat germ calmodulin. Interactions with troponin and sarcoplasmic reticulum. *The Journal of biological chemistry*, 263(1), pp.542–8. Available at: http://www.ncbi.nlm.nih.gov/pubmed/2961748.

Sun, X.X. et al., 2004. The eag potassium channel binds and locally activates calcium/calmodulin-dependent protein kinase II. *The Journal of biological chemistry*, 279(11), pp.10206–14. Available at: http://www.ncbi.nlm.nih.gov/pubmed/14699099 [Accessed July 21, 2011].

Tadross, M.R., Dick, I.E. & Yue, D.T., 2008. Mechanism of local and global Ca2+ sensing by calmodulin in complex with a Ca2+ channel. *Cell*, 133(7), pp.1228–40. Available at: http://www.ncbi.nlm.nih.gov/pubmed/18585356.

Taraska, J.W. et al., 2009. Mapping the structure and conformational movements of proteins with transition metal ion FRET. *Nature methods*, 6(7), pp.532–7. Available at: http://www.pubmedcentral.nih.gov/articlerender.fcgi?artid=2738593&tool=pmcentrez&rendertype=abstract [Accessed October 29, 2010].

Terlau, H. et al., 1997. Amino terminal-dependent gating of the potassium channel rat eag is compensated by a mutation in the S4 segment. *Journal of Physiology*, 502, pp.537–543.

Tidow, H. & Nissen, P., 2013. Structural diversity of calmodulin binding to its target sites. , 280, pp.5551–5565.

Tombola, F., Pathak, M.M. & Isacoff, E.Y., 2006. How does voltage open an ion channel? *Annual review of cell and developmental biology*, 22, pp.23–52. Available at: http://www.ncbi.nlm.nih.gov/pubmed/16704338 [Accessed July 31, 2010].

Tristani-Firouzi, M. & Sanguinetti, M.C., 2006. hERG potassium channels and cardiac arrhythmia. *Nature*, 440(7083), pp.463–9. Available at: http://www.ncbi.nlm.nih.gov/pubmed/16554806.

Urrego, D. et al., 2014. Potassium channels in cell cycle and cell proliferation. *Philosophical transactions of the Royal Society of London. Series B, Biological sciences*, 369(1638), p.20130094. Available at: http://www.pubmedcentral.nih.gov/articlerender.fcgi?artid=3917348&tool=pmcentrez&rendertype=abstract.

Vieira-Pires, R.S. & Morais-Cabral, J.H., 2010. 3(10) Helices in Channels and Other Membrane Proteins. *The Journal of general physiology*, 136(6), pp.585–592.

Villarroel, A. et al., 2014. The ever changing moods of calmodulin: How structural plasticity entails transductional adaptability. *Journal of Molecular Biology*, 426(15), pp.2717–2735. Available at: http://dx.doi.org/10.1016/j.jmb.2014.05.016.

Wang, Z., Wilson, G.F. & Griffith, L.C., 2002. Calcium/calmodulin-dependent protein kinase II phosphorylates and regulates the Drosophila eag potassium channel. *The Journal of biological chemistry*, 277(27), pp.24022–9. Available at: http://www.ncbi.nlm.nih.gov/pubmed/11980904 [Accessed July 21, 2011].

Warmke, J., Drysdale, R. & Ganetzky, B., 1991. A distinct potassium channel polypeptide encoded by the Drosophila eag locus. *Science (New York, N.Y.)*, 252(5012), pp.1560–2. Available at: http://www.ncbi.nlm.nih.gov/pubmed/1840699.

Warmke, J.W. & Ganetzky, B., 1994. A family of potassium channel genes related to eag in Drosophila and mammals. *Proceedings of the National Academy of Sciences of the United States of America*, 91(8), pp.3438–42. Available at: http://www.pubmedcentral.nih.gov/articlerender.fcgi?artid=43592&tool=pmcentrez&rendertype=abstract [Accessed August 2, 2010].

Williamson, R. a et al., 1997. Mapping the binding site for matrix metalloproteinase on the N-terminal domain of the tissue inhibitor of metalloproteinases-2 by NMR chemical shift perturbation. *Biochemistry*, 36(45), pp.13882–9. Available at: http://www.ncbi.nlm.nih.gov/pubmed/9374866.

Winn, M.D. et al., 2011. Overview of the CCP4 suite and current developments. *Acta Crystallographica Section D: Biological Crystallography*, 67, pp.235–242.

Xu, Q. et al., 2013. Structure of a Ca(2+)/CaM:Kv7.4 (KCNQ4) B-helix complex provides insight into M current modulation. *Journal of molecular biology*, 425(2), pp.378–94. Available at: http://www.pubmedcentral.nih.gov/articlerender.fcgi?artid=3540129&tool=pmcentrez&rendertype=abstract [Accessed May 4, 2014].

Yamniuk, A.P. & Vogel, H.J., 2004. Calmodulin ' s Flexibility Allows for Promiscuity in Its Interactions with Target Proteins and Peptides. , 27(403), pp.35–57.

Zhou, Y. et al., 2001. Chemistry of ion coordination and hydration revealed by a K+ channel-Fab complex at 2.0 A resolution. *Nature*, 414(6859), pp.43–48.

Ziechner, U. et al., 2006. Inhibition of human ether à go-go potassium channels by Ca2+/calmodulin binding to the cytosolic N- and C-termini. *The FEBS journal*, 273(5), pp.1074–86. Available at: http://www.ncbi.nlm.nih.gov/pubmed/16478480.

doi:10.1016/j.jmb.2012.06.025 J. Mol. Biol. (2012) 423, 34–46

Contents lists available at www.sciencedirect.com

Journal of Molecular Biology

journal homepage: http://ees.elsevier.com.jmb

Structural, Biochemical, and Functional Characterization of the Cyclic Nucleotide Binding Homology Domain from the Mouse EAG1 Potassium Channel

Maria J. Marques-Carvalho[1,2], Nirakar Sahoo[3], Frederick W. Muskett[4], Ricardo S. Vieira-Pires[1], Guillaume Gabant[5], Martine Cadene[5], Roland Schönherr[3] and João H. Morais-Cabral[1]*

[1]*Instituto de Biologia Molecular e Celular, Universidade do Porto, Rua do Campo Alegre 823, 4150-180 Porto, Portugal*
[2]*Instituto de Ciências Biomédicas Abel Salazar, Universidade do Porto, Portugal*
[3]*Center for Molecular Biomedicine, Department of Biophysics, Jena University Hospital, Jena, Germany*
[4]*Department of Biochemistry, University of Leicester, UK*
[5]*Centre de Biophysique Moléculaire, CNRS UPR430, Orléans, France*

Received 17 May 2012;
received in revised form
14 June 2012;
accepted 16 June 2012
Available online
23 June 2012

Edited by J. Bowie

Keywords:
CNB domain;
CNB-homology domain;
calmodulin;
crystal structure

KCNH channels are voltage-gated potassium channels with important physiological functions. In these channels, a C-terminal cytoplasmic region, known as the cyclic nucleotide binding homology (CNB-homology) domain displays strong sequence similarity to cyclic nucleotide binding (CNB) domains. However, the isolated domain does not bind cyclic nucleotides. Here, we report the X-ray structure of the CNB-homology domain from the mouse EAG1 channel. Through comparison with the recently determined structure of the CNB-homology domain from the zebrafish ELK (eag-like K^+) channel and the CNB domains from the MlotiK1 and HCN (hyperpolarization-activated cyclic nucleotide-gated) potassium channels, we establish the structural features of CNB-homology domains that explain the low affinity for cyclic nucleotides. Our structure establishes that the "self-liganded" conformation, where two residues of the C-terminus of the domain are bound in an equivalent position to cyclic nucleotides in CNB domains, is a conserved feature of CNB-homology domains. Importantly, we provide biochemical evidence that suggests that there is also an unliganded conformation where the C-terminus of the domain peels away from its bound position. A functional characterization of this unliganded conformation reveals a role of the CNB-homology domain in channel gating.

*Corresponding author. E-mail address: jcabral@ibmc.up.pt.

Abbreviations used: CNB, cyclic nucleotide binding; EAG, ether-a-go-go; ELK, eag-like K^+; CNG, cyclic nucleotide-gated; HCN, hyperpolarization-activated cyclic nucleotide-gated; mEAG1, mouse EAG1; wt, wild type; PDB, Protein Data Bank; 3D, three-dimensional; HSQC, heteronuclear single quantum coherence.

Introduction

The KCNH channel family includes EAG (ether-a-go-go) channels, ERG (eag-related gene) channels, and ELK (eag-like K^+) channels.[1] KCNH channels are voltage-gated potassium channels that have important roles in cardiac repolarization,[2] neuronal excitability,[3] and cellular proliferation and tumor

growth.[4] They are tetrameric potassium channels with six transmembrane helices per subunit; similar to other voltage-gated potassium channels, the membrane-buried regions are organized as four voltage sensor domains surrounding a central pore domain.[1] KCNH channels are also characterized by having large N- and C-terminal cytoplasmic regions, which include a Per-Arnt-Sim domain at the very N-terminus and a domain displaying sequence homology to cyclic nucleotide binding domains (the CNB-homology domain) on the C-terminal region, just after the last transmembrane helix.

The functional role of the cytoplasmic regions remains unclear. It is thought that they are involved in regulation of channel function and act as interfaces for cellular signaling networks; there is evidence showing that these regions include phosphorylation sites,[5] sites for interaction with kinases,[6] integrins,[7] and calmodulin.[8] Ca^{2+}/calmodulin regulation has been well established in the human EAG1 channel[8]; the channel is inhibited by increasing Ca^{2+} concentration, an effect that is mediated through calmodulin binding to the channel. Three different calmodulin binding sequences have been identified, one in the cytoplasmic N-terminal region (BD-N) and two in the C-terminal region (BD-C1 and BD-C2), immediately after the CNB-homology domain.[9] The *in vitro* affinity for Ca^{2+}/calmodulin has been determined for the three sites: 100–200 nM for BD-N and BD-C2, while for BD-C1, the reported affinity varied between ~300 nM and more than 5 μM, depending on the approach used. Fluorescence resonance energy transfer analysis of the interaction between calmodulin and the human EAG1 channel in culture cells revealed that calmodulin binds to BD-N both in low and in high cytosolic Ca^{2+} concentrations, while binding of calmodulin to site BD-C2 appears to occur only in high Ca^{2+} concentrations.[10] A channel with mutations in BD-N and BD-C2 (reducing their calmodulin affinity) and an intact BD-C1 site showed no fluorescence resonance energy transfer signal, consistent with a low-affinity site. Importantly, mutations that reduce calmodulin affinity at any of the three sites also drastically reduce channel inhibition by Ca^{2+}/calmodulin, supporting the functional importance of all three sites for Ca^{2+}/calmodulin regulation.[9]

The CNB-homology domains in the KCNH channels are particularly intriguing. These domains have strong sequence similarity to cyclic nucleotide binding (CNB) domains of cyclic nucleotide-gated (CNG) channels and hyperpolarization-activated cyclic nucleotide-gated (HCN) channels.[1] In HCN and CNG channels, binding of cAMP or cGMP to the CNB domain induces a conformational change in the domain, which is propagated to the gate of the channel favoring channel activation.[11–13] However, it has been shown that the *in vitro* affinity of the CNB-homology domain of mouse EAG1 (mEAG1) and human ERG channels for cyclic nucleotides is very low ($K_d \geq 50$ μM) and that the function of KCNH channels is not altered upon exposure to cyclic nucleotides.[14]

Very recently, the structure of the CNB-homology domain from a zebrafish ELK (zELK) channel was reported by Brelidze *et al.*[15] This structure reveals the typical fold of CNB domains as expected. Surprisingly, the domain adopts a self-liganded conformation, where side chains from two conserved residues at the C-terminus interact with the domain region that is equivalent to the ligand binding pocket in CNB domains. The structure raises many questions: Is the self-liganded conformation a conserved feature of CNB-homology domains? Does an "unliganded" state exist in CNB-homology domains? Are the many similarities between *bona fide* CNB domains and CNB-homology domains also reflected at the functional level?

With the purpose of better understanding the structural and functional properties of the CNB-homology domain of the KCNH channels, we have determined the crystal structure of this domain from the mEAG1 channel and have performed a biochemical and functional characterization.

Results

Structure of the CNB-homology domain from mEAG1

We have determined the structure of the CNB-homology domain from the mEAG1 channel at 2.2 Å (Fig. 1a and b and Supplementary Fig. 1; Table 1); it shows the typical fold of a CNB domain, with three helices (αA, αB, and αC) lying on the surface of a β-roll. Residues immediately after the αC helix (residues 696 to 707), which we designate as the C-terminal tail of the domain, adopt an extended conformation and snake over the surface of the structure. The structure also includes part of the C-linker (helices αD′, αE′, and αF′) that connects the domain to the last transmembrane helix of the channel.

Superposition through the β-roll of our CNB-homology structure with the CNB-homology structure from the zELK channel shows the strong similarities (Fig. 2a). The domain helices are differently positioned on the surface of the β-roll but maintain the same relative disposition between each other (Fig. 2b). Importantly, the two structures adopt the same "self-liganded" conformation. In both structures, two residues in the C-terminal tail (Y699 and L701 in the mEAG1 channel), which are conserved across KCNH channels (Supplementary Fig. 1), occupy the volume taken up by cAMP in the

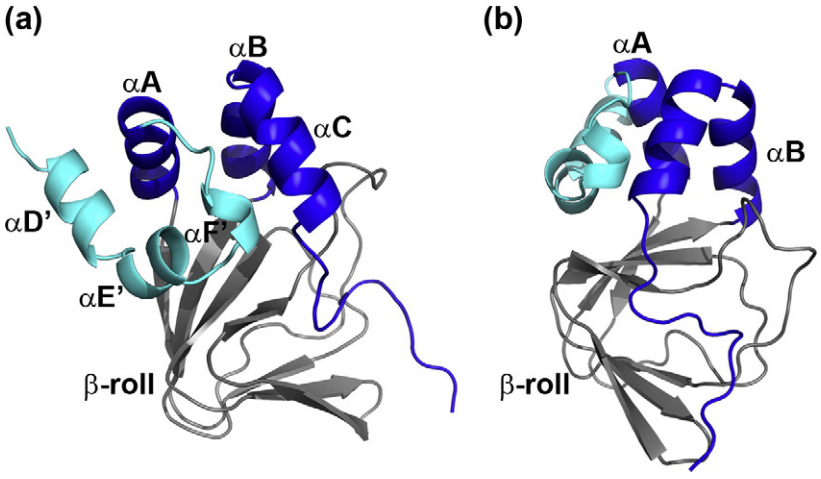

Fig. 1. Structure of the CNB-homology domain from the mEAG1 channel. (a and b) Cartoon representations of the CNB-homology domain (two different views rotated ~90°). C-linker stretch is depicted in cyan, CNB-homology domain helices are in dark blue, and β-roll is in gray.

CNB domains of the HCN and MlotiK1 channels (Fig. 2c and d). The presence of the same conformation in the two different crystal structures, determined from domain constructs with very different limits (the mEAG1 domain includes only part of the C-linker while the domain from zELK has the whole linker) and originating from different KCNH channel subfamilies (with just ~40% identity over the domain sequence), supports the proposal that this conformation is a significant feature of KCNH channels.

Table 1. Crystallographic statistics

Crystal data	
Space group	$P3_121$
Unit cell parameters	
$a=b$ (Å)	60.3
c (Å)	85.4
α = β (°)	90
γ (°)	120
Data collection details	
Diffraction source	ESRF beamline ID14_4
Wavelength (Å)	0.9765
Resolution range (Å)	52.3–2.2 (2.31–2.2)
No. of unique reflections	9566 (1356)
No. of measured reflections	59,240 (7118)
Multiplicity	6.2 (5.2)
Completeness (%)	99.4 (97.5)
$I/\sigma I$	4.8 (2.2)
R_{sym} (%)	8.9 (25.1)
Refinement data	
Resolution range	52.3–2.2 (2.34–2.2)
No. of reflections	9540
R_{work}/R_{free} (%)	18.6/21.8 (28.7/34.0)
No. of atoms in model	
Protein	1151
Solvent	49
Average B value (Å^2)	
Protein	56.5
Solvent	58.2
RMSD bond length (Å)	0.008
RMSD bond angles (°)	1.085

The values in parentheses correspond to statistics for data in the highest-resolution shell.

The pocket in the CNB-homology domains

To better understand the structural underpinnings of the low affinity of cyclic nucleotides for the CNB-homology domains, we compared the structures of CNB-homology domains and CNB domains. Similar to CNB domains, there is a shallow "binding pocket" in CNB-homology domains (Fig. 3a and b and Supplementary Fig. 2a). This pocket is more open than the CNB domain binding pockets. For example, in the bound or unbound conformations of the CNB domains from the MlotiK1 channel, the C^{α}–C^{α} distance between F296 and S308 is 10.6 Å (Fig. 3b), while in the HCN2 channel CNB domain, the equivalent distance is 10.8 Å (F580 to T592); in contrast, in the CNB-homology domains, the distance between equivalent residues [F644 to C658 in mEAG1 (Fig. 3a); I683 to N697 in zELK] is 12.5 Å and 12.1 Å, respectively. There is also an interesting aspect in the conservation of residues of the pocket. Many of the residues that surround the base of the nucleotide in the MlotiK1 CNB domain (V282, L290, F296, and V311) (Fig. 3b), and which are fairly conserved across CNB domains, are basically unchanged in the mEAG1 CNB-homology domain (V628, L638, F644, and V661) (Fig. 3a) and in zELK (V667, L677, I683, and V700) (Supplementary Fig. 1). In contrast, the residues that interact with the ribose and phosphate groups of the nucleotide, and which are conserved in the CNB domains, are very different from the ones present in the equivalent region of the mEAG1 channel (Fig. 3a and b). Even when there is chemical similarity between residues in this region, such as E298 in MlotiK1 (highly conserved across all CNB domains) and D646 in mEAG1, the structures diverge, resulting in a very different disposition of the side chains (Fig. 3a and b). Moreover, the key arginine that interacts with the phosphate group in CNB domains (R307 in MlotiK1) and determines much of the affinity for the ligand[16] is not present in the homology domains and its

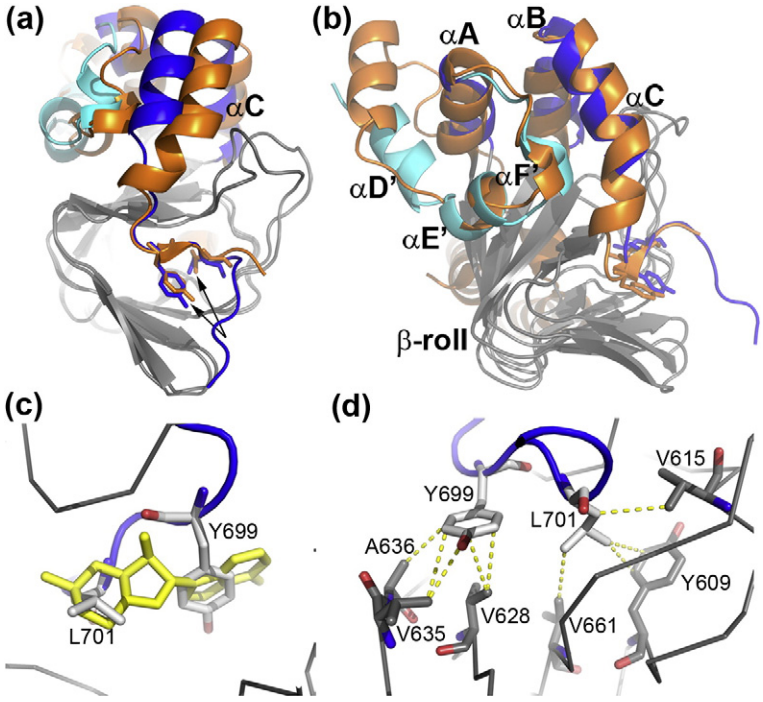

Fig. 2. Structural features of CNB-homology domains. Superpositions of the mEAG1 CNB-homology domain (in gray, cyan, and blue) and the zELK CNB-homology domain (PDB code: 3UKN) (in gray and orange) through the β-roll (a) and through the α-helices (b). Both CNB-homology domain structures share a self-liganded conformation. Residues bound in the pocket are shown in stick model and are indicated by arrows. (c) Close-up view (viewed from binding pocket) of residues Y699 and L701 in the CNB-homology domain from mEAG1 superimposed with cAMP molecule (in yellow stick) from the MlotiK1 CNB domain (PDB code: 1VP6). Superposition of structures was done through residues in β-roll. (d) Residues of CNB-homology domain binding pocket interacting with Y699 and L701 (in white). Residues were selected with a 4-Å radius. View is rotated 180° relative to (c).

space is now shared between two residues (Y609 and V615) in mEAG1 (Fig. 3a and b) or three residues (I648, L654, and T696) in zELK.

Another clear structural difference between the binding pockets is the absence of the αP helix in the CNB-homology domain (Supplementary Fig. 2). This helix is part of the phosphate-binding cassette in the CNB domain. It has been shown to readjust upon ligand binding and to establish essential contacts with the helix αB for the mechanism of ligand-induced conformational change.[13,17] In the CNB-homology domains, αP is replaced by a long loop, and as a consequence, the packing between residues in the pocket and residues in αB is very different.

Overall, the differences in the structure and amino acid composition of the pocket of CNB-homology domains relative to CNB domains can explain the very low affinity of the homology domains for cyclic nucleotides.

Strikingly, in the mEAG1 CNB-homology domain, the two conserved residues (Y699 and L701) bound in the pocket occupy the same volume cyclic nucleotides take up in CNB domains (Fig. 2c). Moreover, the two residues establish an extensive network of interactions with residues in the pocket (Fig. 2d) and some of these interactions are similar to the ones established by cyclic nucleotides in CNB domains. The aromatic ring of the tyrosine is

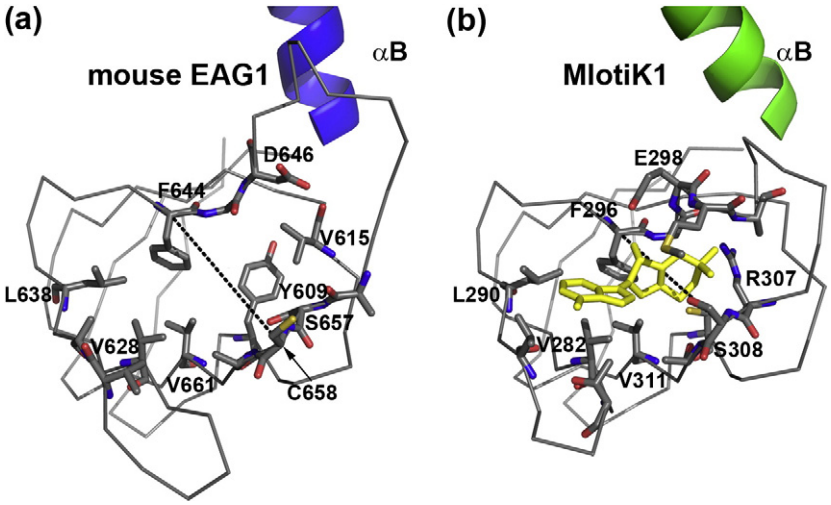

Fig. 3. Comparing binding pockets. (a) Close-up of binding pocket in the CNB-homology domain. (b) Close-up of cAMP binding pocket in CNB domain from MlotiK1; cAMP in yellow stick. PDB code: 1VP6. Some of the residues that line the cAMP binding pocket in MlotiK1, and corresponding residues in the CNB-homology domain, are shown in stick and are labeled. Dotted lines indicate distances measured across the pockets, between equivalent residues: 10.6 Å for the MlotiK1 domain and 12.5 Å for the mEAG1 domain.

roughly at the same position as the aromatic base of the cyclic nucleotide and interacts with some of the residues conserved across CNB and CNB-homology domains; the leucine side chain overlaps with the cyclic phosphate group and interacts with Y609 and V615 (in mEAG1) that take up the position of the arginine conserved in CNB domains.

Biochemical analysis of the self-liganded conformation

An underlying implication of the proposal that the CNB-homology domain adopts a self-liganded conformation is that an unliganded conformation might exist; however, no evidence for this other conformation has been provided. In this context, it is interesting to realize that in our structure, the C-terminal tail includes a significant amino acid stretch (residues 702 to 707) of the previously identified low-affinity BD-C1 calmodulin binding site (residues 702 to 712) (Fig. 4a and Supplementary Fig. 1).[9] This site is not present in the CNB-homology domain of zELK. The site starts immediately after the two residues (Y699 and L701) bound in the pocket and is partially occluded by steric contacts with residues on the surface of the domain. Considering the molecular volume of calmodulin, it becomes clear that the steric occlusion of the BD-C1 site will affect binding of calmodulin and that tight interaction between the two proteins will only occur when the site becomes accessible upon displacement of most of the C-terminal tail away from the domain. This new conformation would correspond to an unliganded state. Importantly, in an unliganded conformation, the apparent affinity of Ca^{2+}/calmodulin will be higher than in the self-liganded state and therefore mutations that destabilize the self-liganded conformation would increase calmodulin affinity.

To explore the existence of an unliganded state, we performed a series of biochemical experiments using dansylated calmodulin, a fluorescent form of the protein.[18] Dansylated calmodulin has previously been reported to have similar properties to native calmodulin, and we ensured that the calmodulin used in our experiments had, on average, just over one dansyl group per protein molecule, as evaluated by mass spectrometry. We first determined the affinity of Ca^{2+}/dansyl calmodulin for BD-C1 (K_d = 1.0 ± 0.1 μM, Fig. 5a) by fusing the peptide sequence (residues 696 to 736 of mEAG1) to maltose-binding protein (MPB-BD-C1) through a long linker. A competition experiment with wild-type (wt) calmodulin confirmed that both labeled and unlabeled forms of calmodulin have similar binding properties (K_d = 1.2 ± 0.1 μM for Ca^{2+}/wt calmodulin, Fig. 5a), and we made use of the modified calmodulin for the rest of our study. We also verified that calmodulin does not bind to MBP alone (Supplementary Fig. 3). These results confirmed previous reports of weak calmodulin binding at the BD-C1 site.[9]

We then measured the affinity of Ca^{2+}/dansyl calmodulin for two different constructs spanning the complete CNB-homology domain and the whole BD-C1 site (residues 552–724 and 552–736). Calmodulin affinity to these constructs is 10- to 20-fold lower than that measured for the BD-C1 site alone, with K_d values of 12.1 ± 1.4 μM and 16 ± 2.6 μM for the shorter and longer constructs, respectively (Fig. 5b). This is consistent with our observation in the structure of partial steric occlusion of BD-C1. From this point onward, we used the smaller CNB-homology domain/BD-C1 construct (residues 552–724).

By mutating residues that appear to hold the C-terminal tail in position, we should destabilize the self-liganded conformation and thus increase the apparent affinity for calmodulin. In the CNB-homology/BD-C1 construct, we generated the C-terminal tail double mutants L697A/Y699A and Y699A/L701A. Y699 and L701 are the two residues in the domain structure that interact with the domain pocket (Fig. 2); L697 is not in the pocket but has

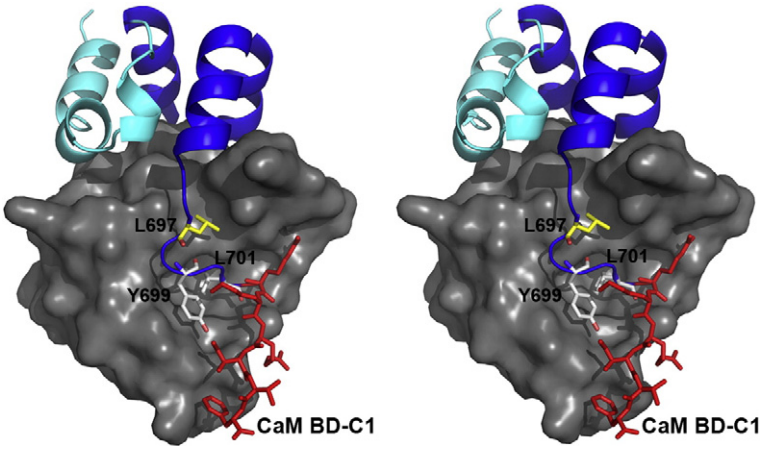

Fig. 4. View of self-liganded conformation and calmodulin binding site. (a) Stereo view of the CNB-homology domain with the two conserved residues bound in the binding pocket. β-Roll is shown as surface representation. Residues from the C-terminal tail that reside in the pocket (Y699 and L701) are shown in white stick; residue L697 is shown in yellow stick. Section of the calmodulin BD-C1 binding site present in the structure is shown in red sticks.

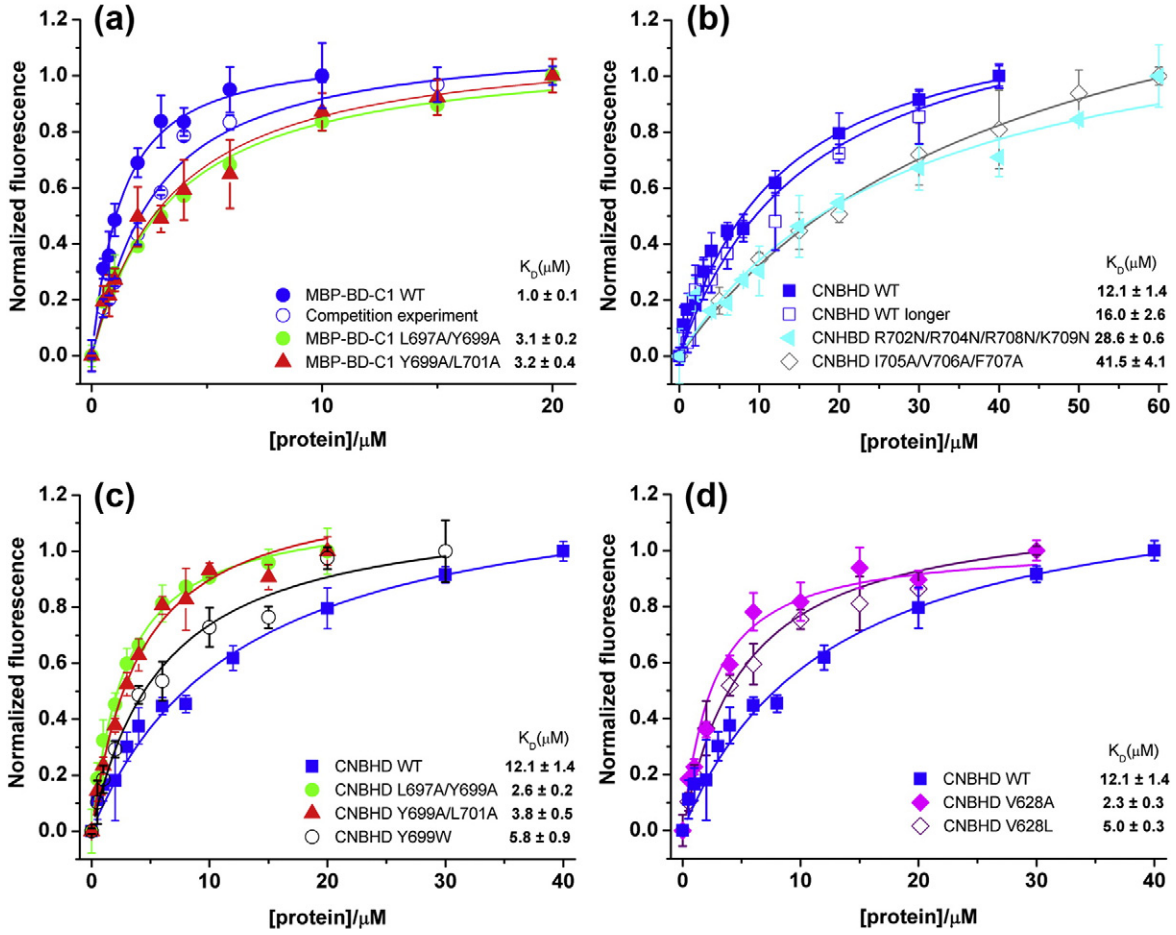

Fig. 5. Fluorescence binding curves with dansylated calmodulin. (a) Titration with calmodulin binding site BD-C1 fused to MBP (blue ●, $N=7$). Competition experiment with wt calmodulin (blue ○, $N=6$). MBP-BD-C1 fusion with mutations L697A/Y699A (green ●, $N=3$) and Y699A/L701A (red ▲, $N=3$). (b) Titration with mEAG1 protein fragments that span the CNB-homology domain and the calmodulin binding site BD-C1. wt mEAG1 spanning residues 552 to 724 (blue ■, $N=4$) and spanning residues 552–736 (blue □, $N=4$). mEAG 552–724 with mutations in the calmodulin binding site: R702N/R704N/R708N/K709N (cyan ◀, $N=2$) and I705A/V706A/F707A (gray ◊, $N=3$). (c) Titration with C-terminal tail mutants of mEAG1 552–724, comparison with wt (blue ■). Mutants L697A/Y699A (green ●, $N=3$), Y699A/L701A (red ▲, $N=3$), and Y699W (black ○, $N=3$). (d) Titration with binding pocket mutants of mEAG1 552–724, comparison with wt (blue ■). Mutants V628A (magenta ◆, $N=3$) and V628L (purple ◊, $N=3$). Error bars are mean ± standard deviation.

extensive contacts with residues in the β-roll (Fig. 4). As was predicted above, the affinity of calmodulin for these mutant domains is higher than that of the wt domain (Fig. 5c), $K_d = 2.6 \pm 0.2$ μM for L697A/Y699A and 3.8 ± 0.5 μM for Y699A/L701A.

We also analyzed the same double mutants (L697A/Y699A and Y699A/L701A) as MBP-BD-C1 fusions. As shown in Fig. 5a, the mutants show similar affinities (L697A/Y699A has a K_d of 3.1 ± 0.2 μM, and Y699A/L701A has a K_d of 3.2 ± 0.4 μM) to the ones determined above for the same mutants in the domain. This similarity supports the notion that in these mutant domains, the BD-C1 site is as accessible as in the MBP fusion and therefore that the C-terminal tail has peeled away from the domain and is exposed. In addition, the small but significant effect of the double mutations in MBP-BD-C1 relative to the wt MBP fusion (Fig. 5a) shows that calmodulin binding to BD-C1 extends all the way to these residues.

Other mutations that are expected to destabilize the self-liganded conformation were also analyzed. The single-residue change Y699W, in the C-terminal tail, also increased the apparent calmodulin affinity but had a milder effect, K_d ~6 μM (Fig. 5c). Importantly, mutations of a residue in the pocket, which in the structure interacts with Y699, also lead to an increase in apparent calmodulin affinity:

V628A and V628L have K_d values of 2.3 and 5 μM, respectively (Fig. 5d).

To better understand the weak interaction between calmodulin and the CNB-homology/BD-C1 channel fragment, we used NMR and performed a minimal chemical shift mapping with ^{15}N-labeled calmodulin.[19,20] In this experiment, we looked exclusively at the changes that occur in calmodulin upon interaction with the domain. Plotting of the minimal chemical shift data (i.e., the sum of the root-mean-square differences in nitrogen and proton chemical shift between free and bound Ca^{2+}/calmodulin) shows that upon binding, the large changes (mean chemical shift difference ≥ 0.08 ppm) are mainly concentrated in residues of the N-terminal lobe of calmodulin (Supplementary Fig. 4a). We mapped the chemical shift data onto a representative structure of calmodulin bound to a peptide stretch [Protein Data Bank (PDB) code: 3OXQ, chain A].[21] Our model shows that the large chemical shifts occur in residues directly involved in the interaction with the peptide (Supplementary Fig. 4b and c). In contrast, in the C-lobe, the major change occurs in T146, which does not interact directly with the bound helix (Fig. 4d). These results indicate that binding to BD-C1 occurs through the calmodulin N-lobe with little participation of the C-lobe, providing an explanation for the low affinity of Ca^{2+}/calmodulin to the BD-C1 site. This type of single-lobe interaction has been described in the literature for calmodulin interaction with sites in voltage-gated calcium channels[21] and in voltage-gated sodium channels.[22] Importantly, the data strongly support the idea that, despite being weak, the *in vitro* interaction of the N-lobe of calmodulin with BD-C1 has the hallmarks of a canonical interaction between a calmodulin lobe and a protein segment and is extensive since it involves residues across the binding surface of the N-lobe.

Overall, the data confirm our expectation that the occlusion of BD-C1 weakens the interaction between the domain and calmodulin. Moreover, destabilization of the self-liganded conformation can be achieved through mutagenesis of residues that in the structure appear to hold the C-terminal tail in position. Importantly, the data also show that much of the stability of the self-liganded conformation results from the residues that interact in the pocket of the domain since mutation of these residues caused the largest increase in calmodulin affinity. However, these experiments do not demonstrate that calmodulin binding to the domain causes destabilization of the self-liganded state. We cannot rule out that the interaction of calmodulin with the CNB-homology/BD-C1 channel fragment involves only part of the binding site. It could happen that the interaction is occurring just with the C-terminal end of the site. In this position, calmodulin is away from the domain and it may not affect its conformation. Binding to the whole BD-C1 site would occur only upon destabilization of the self-liganded conformation by mutagenesis, which would result in the release of the C-terminal tail and exposure of the site.

To address this issue, we performed two different biochemical experiments. First, we showed that the calmodulin interaction with the CNB-homology/BD-C1 does involve residues that are in the amino acid stretch partially occluded and that immediately follow the two conserved residues in the pocket (residues 702 to 707; Fig. 4). Consistent with this, combined mutations of the large apolar residues (I705A, V706A, and F707A) present in the occluded stretch resulted in a lower binding affinity (K_d ~41 μM) (Fig. 5b). These values are most likely an underestimation, because we could not reach the high protein concentrations necessary for saturation in these experiments (≥ 60 μM). Mutations of the positively charged residues in a slightly longer stretch, residues 702 to 709, also showed a contribution to the interaction, although to a lesser extent (K_d ~28 μM for R702N, R704N, R708N, and K709N; Fig. 5b).

Second, we showed that calmodulin binding to the domain has a direct effect on the domain structure. For this, we made use of the seven cysteines in the CNB-homology domain (Supplementary Fig. 5), while both the C-terminal tail (including the calmodulin binding site BD-C1) and calmodulin have none. We monitored changes in cysteine accessibility due to wt calmodulin binding with maleimide–polyethylene glycol 5000, which reacts with free-thiol groups and adds ≥ 10 kDa to the apparent mass of a protein for each modified cysteine.[23] We reasoned that if calmodulin binding alters the structure of the CNB-homology domain, we would expect to observe changes in the accessibility of the cysteines and therefore changes in the rate of cysteine reaction with the reagent. Western blot analysis of a reaction time course clearly shows differences in the pattern of bands consistent with changes in cysteine accessibility resulting from calmodulin binding (Fig. 6); in the sample with saturating amounts of calmodulin, the larger molecular weight bands show up at earlier time points.

Taken together, these two approaches demonstrate that (1) calmodulin binding to the CNB-homology domain occurs very close to the body of the domain, involving residues in the stretch immediately after the two residues that are essential for stabilizing the self-liganded state (Y699/L701), and (2) calmodulin binding results in conformational and/or dynamical changes in the structure of the domain.

Our biochemical and structural analyses show that destabilization of the self-liganded conformation, through mutations of residues involved in contacts between the C-terminal tail and the rest of

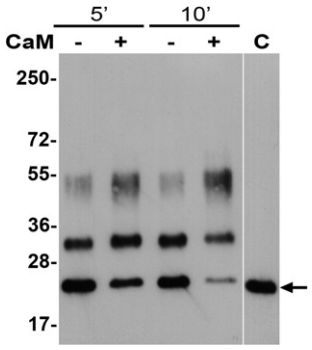

Fig. 6. Structural changes induced by calmodulin binding. Western blot analysis of aliquots from pegylation reaction. Pegylation of wt mEAG1 552–724 was performed in the presence (+) and absence (−) of saturating concentrations of calmodulin and stopped at 5 min and 10 min. Unmodified mEAG1 552–724 (lane C) is indicated by an arrow. Western blot was probed with an anti-His-tag monoclonal antibody.

the domain, results in an increase on the apparent affinity of calmodulin binding to BD-C1. Crucially, they also show that calmodulin binding to the domain is dependent on residues that are on the occluded stretch of the BD-C1 site. A simple consideration of the molecular bulk of calmodulin suggests that this can only occur if this C-terminal tail region peels away from the body of the domain. Consistent with this, we show that binding of calmodulin results in structural changes in the body of the domain. Overall, our biochemical characterization suggests the existence of an unliganded conformation in the CNB-homology domain, a structural counterpart to the self-liganded conformation observed in the domain crystal structure.

Functional analysis

The CNB domains of CNG and HCN channels are involved in regulation of channel activation. It is therefore reasonable to ask if the CNB-homology domain also has a similar role in KCNH channels. To explore this role, we performed electrophysiological recordings on the human EAG1 channel expressed in *Xenopus* oocytes. The amino acid sequence of the sequence stretch spanning the CNB-homology domain and the two C-terminal calmodulin binding sites is identical in the mouse and the human EAG1 channels (Supplementary Fig. 1); however, the human channel has been better functionally characterized.[8,24]

Strikingly, whole-cell two-electrode measurements showed that the destabilization of the self-liganded conformation by mutagenesis is reflected in the gating properties of the channel. Currents elicited at different voltages from wt and C-terminal tail mutant channels are shown in Fig. 7a. It is immediately apparent that the double mutation Y672A/L674A, equivalent to Y699A/L701A in the mEAG1, has effects on channel gating. The rise time to reach 80% current amplitude at +50 mV is longer [251.5 ± 26.8 ms (n = 15)] for this double mutant than for the wt channel [31.9 ± 3.9 ms (n = 17)]. From these currents, we also extracted $V_{1/2}$ of activation (Fig. 7b and c) and the respective slope factor (Fig. 7d). While the slope factors of the activation dependence on voltage were unchanged, the $V_{1/2}$ values for activation were different: −16 mV for the wt channel, 0 mV for the single mutant L670A (equivalent to L697A in mEAG1), and −24 mV and −23 mV, respectively, for the mutants Y672A and L674A (equivalent to Y699A and L701 in mEAG1). The double mutants revealed drastic differences in their effect; the $V_{1/2}$ value for the L670A/Y672A mutant was right shifted to ~2 mV, while the Y672A/L674A mutant is left shifted to −34 mV. The results for the double mutants are surprising since our biochemical experiments with the isolated domain showed that both sets display similar biochemical properties, involving the release of the C-terminal tail. However, in the channel, the double mutants have opposite effects to each other: L670A/Y672A stabilized the closed state over the open state, while Y672A/L674A caused a stabilization of the open state over the closed state.

We also evaluated if channel inhibition by calmodulin is altered in the double mutants. Measurements with excised patches exposed to Ca^{2+}/calmodulin revealed no changes in the sensitivity to Ca^{2+}/calmodulin (Supplementary Fig. 6); inhibition levels as well as on- and off-rates of calmodulin binding were indistinguishable from wt channels. The same experiments were not possible with the other double mutant (Y672A/L674A, equivalent to the mouse Y699A/L701A) due to low expression levels. The lack of effect on inhibition by the mutations that increase *in vitro* calmodulin affinity for BD-C1 may be a reflection of the low importance of this site in the inhibition mechanism. Alternatively, it could be that the relatively small increase (10- to 20-fold) in calmodulin apparent affinity that we measured, with the isolated domain, is difficult to detect in an inhibition process that has a half-maximal inhibition concentration (IC_{50}) of 6 nM for calmodulin[25] and 100 nM for Ca^{2+}.[8]

Discussion

The CNB-homology domain from KCNH channels has raised a lot of interest. These domains have high sequence similarity with the CNB domains in CNG and HCN channels; however, KCNH channel function is not affected by cyclic nucleotide

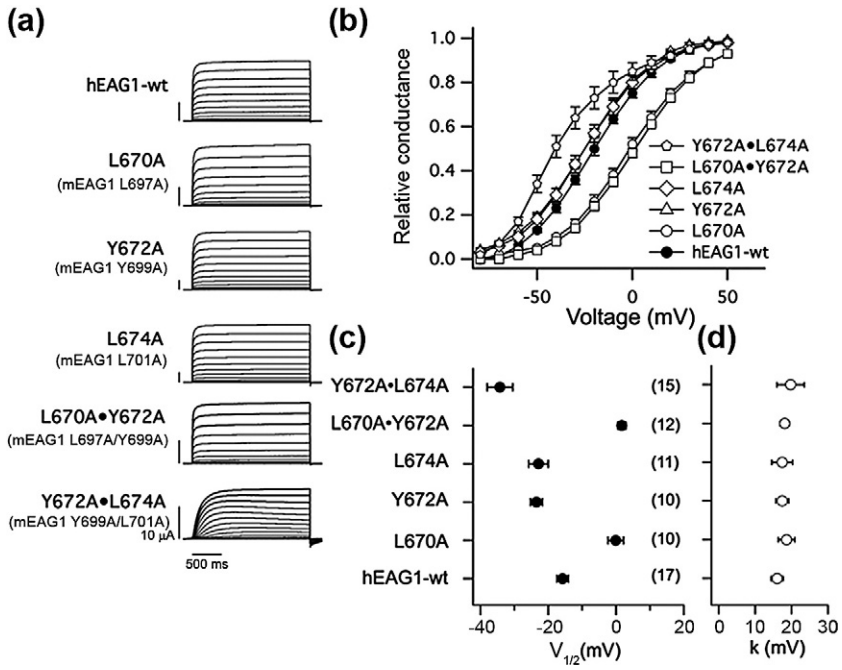

Fig. 7. Functional experiments. (a) Two-electrode voltage-clamp current traces of human EAG1 (hEAG1) and indicated mutants expressed in *Xenopus* oocytes. Residue numbering of mutations in human channel and numbering for equivalent residues in the mouse channel (in parentheses) are indicated. Currents were elicited by 2-s depolarizing pulses from a holding voltage of −90 mV in 10 mV increments between −80 mV and +50 mV. (b) Plot of relative conductance as a function of voltage for wt hEAG1 and the indicated mutants. (c) Plot of $V_{1/2}$ of activation for wt hEAG1 (−15.8 ± 1.7 mV) and mutants (L670A, −0.1 ± 2.3 mV; Y672A, −23.5 ± 1.8 mV; L674A, −22.9 ± 2.9 mV; L670A · Y672A, 1.7 ± 1.3 mV; Y672A · L674A, −34.3 ± 3.8 mV). (d) Plot of values for slope factors corresponding to the $V_{1/2}$ data in (c) (wt, 16.0 ± 0.4 mV; L670A, 18.6 ± 0.7 mV; Y672A, 17.4 ± 0.7 mV; L674A, 17.4 ± 0.9 mV; L670A · Y672A, 18.1 ± 0.6 mV; Y672A · L674A, 19.7 ± 1.9 mV).

exposure.[14] We have now determined the structure of the CNB-homology domain of the mEAG1 channel. A comparison of our structure with the recently reported structure of the CNB-homology domain from the zELK channel and with structures of CNB domains clearly shows that these KCNH channel domains share many of the structural features present in CNB domains. The comparison also reveals crucial sequence and structural differences in the pocket of the CNB-homology domains relative to CNB domains, which provide an explanation for the very low affinity of the CNB-homology domain for cyclic nucleotides. In particular, the CNB-homology domain pocket is more wide open than the ligand binding pocket of CNB domains. In addition, the residues that interact with the cyclic phosphate in CNB domains are absent in CNB-homology domains. Interestingly, the residues that interact with the base of the cyclic nucleotide in CNB domains are conserved in CNB-homology domains.

Importantly, our structure shows that the C-terminal tail of the domain extends over its surface and that two well-conserved residues (Y699 and L701) in the tail occupy the same space that cyclic nucleotides inhabit in CNB domains. This self-liganded conformation is also present in the recently determined structure of the CNB-homology domain of the ELK channel from zebrafish,[15] strongly suggesting that it is a conserved feature of these KCNH channel domains. In our domain, the C-terminal tail also includes a partially occluded stretch of a previously described calmodulin binding site.[9]

By characterizing the CNB-homology domain conformation as self-liganded, it becomes implicit that there is also an unliganded state but there is no evidence for this other conformation. A central aspect of this work is that we have provided biochemical evidence that supports the existence of an unliganded conformation, where the C-terminal tail peels away from the domain. For this, we made use of the affinity of calmodulin to the partially occluded binding site at the end of the C-terminal tail. We demonstrated that mutagenesis of the residues that in the domain structure appear to hold the C-terminal tail in position results in an increase in the apparent affinity of calmodulin, consistent with a release of the tail and increased exposure of the calmodulin binding site. In addition, we showed that calmodulin interaction extends to residues in the occluded stretch of the calmodulin binding site since mutation of some of these residues decreased calmodulin affinity. These residues are immediately after Y699 and L701, and the molecular volume of calmodulin requires a peeling away of the C-terminal tail so that the interaction can occur. Consistent with this interpretation, we showed also that calmodulin binding causes a structural change in the domain as reflected in changes in cysteine accessibility.

Interestingly, the sequence and structural parallels between CNB-homology domains and CNB domains lead naturally to a conclusion that the tail movement is reminiscent of the repositioning of the C-helix away from the ligand-binding pocket, which occurs in CNB domains upon release of cyclic nucleotide.[13,26,27]

Our functional analysis suggests that the CNB-homology domain has a role in channel gating since mutations that destabilize the self-liganded conformation by releasing the C-terminal tail also affect the voltage dependence of activation. Strikingly, these functional effects are not what would be expected from the parallel between the release of the C-terminal tail in the CNB-homology domain and the movement of the C-helix away from its bound-state position that occurs in CNB domains upon release of cyclic nucleotide. In CNG and HCN channels, this CNB domain conformational change favors closure of the channel gate.[11,12] In the human EAG1 channel, the two double mutants, both of which lead to the release the C-terminal tail, have very different effects, stabilizing either the open or the closed state of the channel. This contrasting result indicates that in the full-length channel, these residues have as yet unidentified individual roles besides the shared function of holding the C-terminal tail in its position. This outcome reveals that despite the sequence, structural, and even biochemical similarities, the role of CNB-homology domain in gating of KCNH channels is not identical with the role of CNB domains in HCN and CNG channels. The properties of these domains still require further investigation.

Materials and Methods

Expression and purification of mEAG1 constructs

mEAG1 552–707 (mEAG1—accession codes NP_034730.1 and GI:6754422) was cloned into expression vector pET-15b (Novagen). Construct mEAG1 552–724 and 552–736 were cloned into co-expression vector pRSFDuet-1 (Novagen). A fusion of maltose-binding protein with mEAG1 BDC1 (residues 696–736) was cloned into pRSFDuet-1. Mutants were created using the QuikChange Site-Directed Mutagenesis Kit (Stratagene).

mEAG1 constructs were expressed in *Escherichia coli* BL21(DE3) cells, overnight at 18 °C. Protein was purified by histidine-tag affinity and size-exclusion chromatography, as previously described.[28] The fusion MBP-BD-C1 was expressed and purified with the same basic procedure except 250 mM KCl was used instead of NaCl to minimize aggregation. Protein for crystallization trials was dialyzed overnight at 4 °C against gel-filtration buffer (20 mM Tris–HCl, pH 7.5, 150 mM NaCl, and 5 mM DTT) in the presence of thrombin. Protein for fluorescence binding assays was dialyzed against fluorescence buffer [50 mM Tris–HCl, pH 7.5, 150 mM NaCl, 5 mM $MgCl_2$, 0.1 mM ethylene glycol bis(β-aminoethyl ether) *N*,*N*′-tetraacetic acid, and 2 mM $CaCl_2$ (1.9 mM free Ca^{2+})] without cleaving the tag. In both situations, dialyzed protein was loaded onto a gel-filtration Superdex 200 column (Pharmacia). Protein concentration was determined by measuring absorbance at 280 nm and using the calculated extinction coefficients determined from the ExPASy tool, ProtParam.

Crystallization, data collection, and refinement

Protein was crystallized by mixing 1:1 volumes of protein (at 10 mg/ml in 20 mM Tris–HCl, pH 8, 150 mM NaCl, and 5 mM DTT) and precipitant solution (0.2 M trisodium citrate dihydrate, 20% polyethylene glycol 3350).[28] A data set was collected at the ID14-4 beamline of the European Synchrotron Radiation Facility (ESRF), and the structure was solved by molecular replacement. Model refinement was done in PHENIX[29]; TLS refinement was applied.[30] Model building was performed in Coot[31] and figures were created using PyMOL.[32]

Expression and purification of calmodulin

BL21(DE3) competent cells were transformed with expression vector (pT7-7 human calmodulin) and grown until they reached an OD_{600} (optical density at 600 nm) of 0.6–0.8. IPTG (0.5 mM) was added, followed by a 3-h induction at 37 °C. Cells were resuspended in 50 mM Tris–HCl, pH 7.5, 100 mM NaCl, 5 mM DTT, and 2 mM ethylenediaminetetraacetic acid, supplemented with protease inhibitors. Cell lysis was done in an Emulsiflex-C5 (Avestin), and the lysate was centrifuged. Supernatant was loaded onto a phenyl Sepharose CL-4B (Sigma-Aldrich) column and calmodulin was eluted with 50 mM Tris–HCl, pH 7.5, 2 mM ethylenediaminetetraacetic acid, and 5 mM DTT. Concentration was determined by measuring absorbance at 277 nm and using the extinction coefficient $\varepsilon_{277nm} = 3029\ M^{-1}\ cm^{-1}$.[33]

Derivatization of calmodulin with the fluorophore Dansyl-Cl

wt human calmodulin was derivatized with 5-(dimethylamino)naphthalene-1-sulfonyl chloride (Dansyl-Cl, Molecular Probes), a reagent that reacts with primary amines, as previously described.[18,34]

Fluorescence assay

Dansylated calmodulin at 400 nM was incubated with different protein concentrations at room temperature, for at least 20 min, in fluorescence buffer [50 mM Tris–HCl, pH 7.5, 150 mM NaCl, 5 mM $MgCl_2$, 0.1 mM ethylene glycol bis(β-aminoethyl ether) *N*,*N*′-tetraacetic acid, and 2 mM $CaCl_2$ (1.9 mM free Ca^{2+})]. Fluorescent measurements were done at 26 °C using a Horiba Fluoromax-4 spectrofluorimeter. All emission spectra were obtained using an excitation wavelength of 340 nm, with slit widths of 4 or 5 nm.[18] For each titration curve, fluorescence was measured at the wavelength corresponding to the maximum shift in the emission spectra. The data were normalized using $F_{norm} = (F - F_0)/(F_{max} - F_0)$, where F is the measured fluorescence value for each concentration, F_{max} is the maximum measured fluorescence, and F_0 is the measured fluorescence before adding any mEAG1 protein. F_{norm} was plotted as a function of total protein concentration using OriginPro8. Data were fitted to a modified hyperbolic function of the form: $F_{norm} = F/(1 + 2/(-1 - (1/K_d)[\text{dansyl-CaM}] + (1/K_d)[\text{mEAG1}] + \text{sqrt}\ ((1 + (1/K_d)[\text{dansyl-CaM}] - (1/K_d)[\text{mEAG1}])^2 + 4(1/K_d)[\text{mEAG1}])))$,

where K_d is the dissociation constant, [dansyl-CaM] is the total concentration of dansylated calmodulin, [mEAG1] is the total concentration of the mEAG1 domain, and F is an adjusting factor.

The competition experiment was performed in the presence of 4 μM wt calmodulin, and data were fitted to the function[35]

$$F_{\text{norm}} = F\left(2\cos(d/3)\,\text{sqrt}\left(a^2-3b\right)-a\right) / \left(3\left(1/K_d\text{dansyl}\right) + \left(2\cos(d/3)\,\text{sqrt}\left(a^2-3b\right)-a\right)\right)$$

$$a = \left(1/K_d\text{dansyl}\right) + \left(1/K_d\text{WT}\right) + \left[\text{dansyl–CaM}\right] + [\text{WT–CaM}] + [\text{mEAG1}]$$

$$b = \left(1/K_d\text{WT}\right)\left(\left[\text{dansyl–CaM}\right]-[\text{mEAG1}]\right) + \left(1/K_d\text{dansyl}\right)\left([\text{WT–CaM}]-[\text{mEAG1}]\right) + \left(1/K_d\text{dansyl}\right)\left(1/K_d\text{WT}\right)$$

$$c = -\left(1/K_d\text{dansyl}\right)\left(1/K_d\text{WT}\right)[\text{mEAG1}]$$

$$d = a\cos\left(\left(-2a^3 + 9ab - 27c\right) / \left(2\,\text{sqrt}\left(\left(a^2-3b\right)^3\right)\right)\right)$$

where K_d dansyl is the dissociation constant for dansylated calmodulin, K_d WT is the dissociation constant for wt calmodulin, [dansyl-CaM] is the total concentration of dansylated calmodulin, [WT-CaM] is the total concentration of wt calmodulin, [mEAG1] is the total concentration of the mEAG1 domain, and F is an adjusting factor.

Pegylation assay

wt mEAG1 552–724 was diluted to 2 μM in fluorescence buffer with 1 mM TCEP and incubated at room temperature for 1 h in the presence and absence of 50 μM calmodulin. Methoxypolyethylene glycol maleimide (Fluka/Sigma-Aldrich) was added to the protein mixture at 5 mM and incubated at 4 °C for 5 or 10 min. Reactions were stopped by addition of DTT to a final concentration of 200 mM, incubation for 30 min, and addition of SDS-PAGE loading buffer. Samples were run on a 15% SDS-PAGE and analyzed by Western blot. Proteins were probed with an anti-His-tag monoclonal antibody (Qiagen).

Mass spectrometry

Proteins were analyzed by MALDI-TOF MS (matrix-assisted laser desorption/ionization time-of-flight mass spectrometry). The matrix solution consisted of saturated 4-hydroxy-α-cyano-cinnamic acid in 66.5% H_2O, 33.3% CH_3CN, and 0.1% trifluoroacetic acid. Analytes in the micromolar range were prepared by 20-fold to 200-fold dilution into the matrix solution. The analyte-matrix samples were spotted onto a gold-plated sample probe using the ultrathin layer method as previously described[36,37] and analyzed in linear positive ion mode. Spots were washed with 0.1% trifluoroacetic acid before acquisition. Analyses were performed using an Autoflex I or an Ultraflex I mass spectrometer (Bruker Daltonics, Germany) equipped with a 337-nm nitrogen laser and a gridless delayed extraction ion source. An accelerating voltage of 20 kV was used and delay was optimized between 500 and 650 ns to achieve a mass resolution greater than 1000 over the mass range of interest (10,000–20,000 Da). A deflection of matrix ions up to 600 Da was applied to prevent detector saturation. Spectra were acquired in linear positive ion mode by accumulation of 300–500 laser shots. The instrument was controlled using Bruker FlexControl software. Calibration was performed externally using apomyoglobin and cytochrome *c*. MALDI-TOF-MS spectra were processed using FlexAnalysis 2.0 software from Bruker Daltonics and cleavage peptides were assigned using Paws version 8.5.0.3 (ProteoMetrics, New York, NY).

NMR spectroscopy

NMR spectra for the backbone assignment of CaM were acquired from 0.35-ml samples of 0.4 mM calmodulin in a 20 mM Tris, 140 mM sodium chloride, 10 mM $CaCl_2$, 0.2 mM AEBSF, and 0.02% (w/v) sodium azide buffer at pH 7.5, containing 5% D_2O/95% H_2O. All NMR experiments were acquired at 298 K and were performed on Bruker DRX or AvanceII spectrometers operating at either 600 or 800 MHz that were fitted with cryogenically cooled probe heads. The two-dimensional (2D) and three-dimensional (3D) spectra recorded to obtain sequence-specific assignments for CaM were as follows: $^{15}N/^{1}H$ heteronuclear single quantum coherence (HSQC); nuclear Overhauser enhancement spectroscopy-HSQC with a nuclear Overhauser enhancement mixing time of 100 ms; $^{13}C/^{1}H$ HSQC and $^{15}N/^{13}C/^{1}H$ HNCACB, CBCA(CO)NH, HNCA, and HN(CO)CA (Ref. 38 and references therein). Typical acquisition times in F_1 and F_2 for the 3D experiments were 20 ms for ^{15}N, 6.6–9.6 ms for ^{13}C, and 18 ms for ^{1}H, with an acquisition time of 80 ms in F_3 (^{1}H). The majority of the 3D spectra were collected over approximately 48 h, and $^{15}N/^{1}H$ and $^{13}C/^{1}H$ HSQC spectra were collected over about 1 h. Typical acquisition times in 2D experiments were 60 ms (^{15}N), 9 ms (^{13}C), and 80 ms in F_2 (^{1}H). Water suppression was achieved using the gradient-based WATERGATE method.[39] The 3D NMR data were processed using NMRPipe[40] with linear prediction used to extend the effective acquisition times by up to twofold in F_1 and F_2. The resulting spectra were analyzed using the program Sparky (T. D. Goddard and D. G. Kneller, Sparky 3, University of California, San Francisco).

NMR chemical shift mapping of binding sites

$^{15}N/^{1}H$ transverse relaxation optimized spectroscopy[41] spectra of calmodulin were acquired in the presence and absence of mEAG1 552–724 to identify the changes in the positions of signals induced by CNB-homology domain binding. In these experiments, amounts of unlabeled mEAG1 552–724 were added to 100 μM ^{15}N-labeled calmodulin to achieve 30% and 90% saturation of calmodulin based on the determined K_d. Experiments were performed in the same buffer as used for calmodulin assignment but with the addition of 2 mM DTT. Typical acquisition times for the transverse relaxation optimized spectroscopy experiments were 80 ms in F_2 (^{1}H) and 30 ms in F_1 (^{15}N), with the spectra collected over

approximately 3 h. The perturbation of backbone amide chemical shifts in the presence of mEAG1 552–724 was calculated relative to calmodulin alone using the minimum chemical shift procedure[19,20] and then used to identify the intramolecular interface of mEAG1 552–724 on calmodulin.

Electrophysiological measurements and data analysis

Recording and data analysis were described previously.[42] In brief, stage V *Xenopus* oocytes were injected with 50 nl of mRNA and currents were recorded at 20–23 °C, 2 to 4 days after injection. A two-electrode voltage clamp amplifier (Turbo-TEC 10CD, npi electronic, Tamm, Germany) was controlled by PatchMaster software (HEKA Elektronik, Lambrecht, Germany). A P/n method was used for leak correction. The bath solution contained (in millimolar): 115 NaCl, 2.5 KCl, 1.8 $CaCl_2$, and 10 Hepes, pH 7.2 (NaOH). Data were analyzed with FitMaster software (HEKA Elektronik). Normalized conductances were obtained by fitting the following equation to the current–voltage data:

$$I(V) = GV\left(1-e^{-((V-E_{rev})/25\ mV)}\right) / \left(1-e^{-(V/25\ mV)}\right)*1 \\ / \left(1+e^{-((V-V_{1/2})/k)}\right)$$

G is the maximal conductance and E_{rev} the estimated reversal potential. The second term describes the channel open probability (or relative conductance), characterized by $V_{1/2}$, the voltage of half-maximal activation, and a slope factor, k.

Accession numbers

Coordinates and structure factors have been deposited in the PDB with accession number 4F8A.

Acknowledgements

We thank access to ESRF through the Portuguese BAG and help from the ID14-4 support staff. We also thank Carol Harley for helpful discussions. Support for this work has been provided to J.H.M.-C. by the European Molecular Biology Organization (Installation grant). Funds were also provided through FEDER-POPC-COMPETE program and Fundação de Ciência e Tecnologia (FCOMP-010124-Feder-007427/PTDC/QUI/66171/2006), (FCOMP-01-0124-FEDER-022718 (PEst-C/SAU/LA0002/2011)).

Supplementary Data

Supplementary data to this article can be found online at http://dx.doi.org/10.1016/j.jmb.2012.06.025

References

1. Warmke, J. W. & Ganetzky, B. (1994). A family of potassium channel genes related to eag in *Drosophila* and mammals. *Proc. Natl Acad. Sci. USA*, **91**, 3438–3442.
2. Sanguinetti, M. C. & Tristani-Firouzi, M. (2006). hERG potassium channels and cardiac arrhythmia. *Nature*, **440**, 463–469.
3. Becchetti, A., De Fusco, M., Crociani, O., Cherubini, A., Restano-Cassulini, R., Lecchi, M. *et al.* (2002). The functional properties of the human ether-a-go-go-like (HELK2) K+ channel. *Eur. J. Neurosci.* **16**, 415–428.
4. Pardo, L. A. & Suhmer, W. (2008). Eag1 as a cancer target. *Expert Opin. Ther. Targets*, **12**, 837–843.
5. Wang, Z., Wilson, G. F. & Griffith, L. C. (2002). Calcium/calmodulin-dependent protein kinase II phosphorylates and regulates the *Drosophila* eag potassium channel. *J. Biol. Chem.* **277**, 24022–24029.
6. Sun, X. X., Hodge, J. J., Zhou, Y., Nguyen, M. & Griffith, L. C. (2004). The eag potassium channel binds and locally activates calcium/calmodulin-dependent protein kinase II. *J. Biol. Chem.* **279**, 10206–10214.
7. Cherubini, A., Hofmann, G., Pillozzi, S., Guasti, L., Crociani, O., Cilia, E. *et al.* (2005). Human ether-a-go-go-related gene 1 channels are physically linked to beta1 integrins and modulate adhesion-dependent signaling. *Mol. Biol. Cell*, **16**, 2972–2983.
8. Schonherr, R., Lober, K. & Heinemann, S. H. (2000). Inhibition of human ether a go-go potassium channels by Ca(2+)/calmodulin. *EMBO J.* **19**, 3263–3271.
9. Ziechner, U., Schonherr, R., Born, A. K., Gavrilova-Ruch, O., Glaser, R. W., Malesevic, M. *et al.* (2006). Inhibition of human ether a go-go potassium channels by Ca2+/calmodulin binding to the cytosolic N- and C-termini. *FEBS J.* **273**, 1074–1086.
10. Goncalves, J. T. & Stuhmer, W. (2010). Calmodulin interaction with hEAG1 visualized by FRET microscopy. *PLoS One*, **5**, e10873.
11. Craven, K. B. & Zagotta, W. N. (2006). CNG and HCN channels: two peas, one pod. *Annu. Rev. Physiol.* **68**, 375–401.
12. Kaupp, U. B. & Seifert, R. (2002). Cyclic nucleotide-gated ion channels. *Physiol. Rev.* **82**, 769–824.
13. Rehmann, H., Wittinghofer, A. & Bos, J. L. (2007). Capturing cyclic nucleotides in action: snapshots from crystallographic studies. *Nat. Rev. Mol. Cell Biol.* **8**, 63–73.
14. Brelidze, T. I., Carlson, A. E. & Zagotta, W. N. (2009). Absence of direct cyclic nucleotide modulation of mEAG1 and hERG1 channels revealed with fluorescence and electrophysiological methods. *J. Biol. Chem.* **284**, 27989–27997.
15. Brelidze, T. I., Carlson, A. E., Sankaran, B. & Zagotta, W. N. (2012). Structure of the carboxy-terminal region of a KCNH channel. *Nature*, **481**, 530–533.
16. Altieri, S. L., Clayton, G. M., Silverman, W. R., Olivares, A. O., De la Cruz, E. M., Thomas, L. R. & Morais-Cabral, J. H. (2008). Structural and energetic analysis of activation by a cyclic nucleotide binding domain. *J. Mol. Biol.* **381**, 655–669.
17. Rehmann, H., Prakash, B., Wolf, E., Rueppel, A., de Rooij, J., Bos, J. L. & Wittinghofer, A. (2003). Structure

and regulation of the cAMP-binding domains of Epac2. *Nat. Struct. Biol.* **10**, 26–32.
18. Kincaid, R. L., Billingsley, M. L. & Vaughan, M. (1988). Preparation of fluorescent, cross-linking, and biotinylated calmodulin derivatives and their use in studies of calmodulin-activated phosphodiesterase and protein phosphatase. *Methods Enzymol.* **159**, 605–626.
19. Farmer, B. T., 2nd, Constantine, K. L., Goldfarb, V., Friedrichs, M. S., Wittekind, M., Yanchunas, J., Jr *et al.* (1996). Localizing the NADP+ binding site on the MurB enzyme by NMR. *Nat. Struct. Biol.* **3**, 995–997.
20. Williamson, R. A., Carr, M. D., Frenkiel, T. A., Feeney, J. & Freedman, R. B. (1997). Mapping the binding site for matrix metalloproteinase on the N-terminal domain of the tissue inhibitor of metalloproteinases-2 by NMR chemical shift perturbation. *Biochemistry*, **36**, 13882–13889.
21. Kim, E. Y., Rumpf, C. H., Van Petegem, F., Arant, R. J., Findeisen, F., Cooley, E. S. *et al.* (2010). Multiple C-terminal tail Ca(2+)/CaMs regulate Ca(V)1.2 function but do not mediate channel dimerization. *EMBO J.* **29**, 3924–3938.
22. Sarhan, M. F., Tung, C. C., Van Petegem, F. & Ahern, C. A. (2012). Crystallographic basis for calcium regulation of sodium channels. *Proc. Natl Acad. Sci. USA*, **109**, 3558–3563.
23. Lu, J. & Deutsch, C. (2001). Pegylation: a method for assessing topological accessibilities in Kv1.3. *Biochemistry*, **40**, 13288–13301.
24. Gavrilova-Ruch, O., Schonherr, K., Gessner, G., Schonherr, R., Klapperstuck, T., Wohlrab, W. & Heinemann, S. H. (2002). Effects of imipramine on ion channels and proliferation of IGR1 melanoma cells. *J. Membr. Biol.* **188**, 137–149.
25. Sahoo, N., Troger, J., Heinemann, S. H. & Schonherr, R. (2010). Current inhibition of human EAG1 potassium channels by the Ca^{2+} binding protein S100B. *FEBS Lett.* **584**, 3896–3900.
26. Clayton, G. M., Silverman, W. R., Heginbotham, L. & Morais-Cabral, J. H. (2004). Structural basis of ligand activation in a cyclic nucleotide regulated potassium channel. *Cell*, **119**, 615–627.
27. Sharma, H., Yu, S., Kong, J., Wang, J. & Steitz, T. A. (2009). Structure of apo-CAP reveals that large conformational changes are necessary for DNA binding. *Proc. Natl Acad. Sci. USA*, **106**, 16604–16609.
28. Marques-Carvalho, M. J. & Morais-Cabral, J. H. (2012). Crystallization and preliminary X-ray crystallographic characterization of a cyclic nucleotide-binding homology domain from the mouse EAG potassium channel. *Acta Crystallogr., Sect. F: Struct. Biol. Cryst. Commun.* **68**, 337–339.
29. Adams, P. D., Afonine, P. V., Bunkoczi, G., Chen, V. B., Davis, I. W., Echols, N. *et al.* (2010). PHENIX: a comprehensive Python-based system for macromolecular structure solution. *Acta Crystallogr., Sect. D: Biol. Crystallogr.* **66**, 213–221.
30. Painter, J. & Merritt, E. A. (2006). Optimal description of a protein structure in terms of multiple groups undergoing TLS motion. *Acta Crystallogr., Sect. D: Biol. Crystallogr.* **62**, 439–450.
31. Emsley, P. & Cowtan, K. (2004). Coot: model-building tools for molecular graphics. *Acta Crystallogr., Sect. D: Biol. Crystallogr.* **60**, 2126–2132.
32. Schrodinger, LLC. (2010). The AxPyMOL Molecular Graphics Plugin for Microsoft PowerPoint, Version 1.0.
33. Strasburg, G. M., Hogan, M., Birmachu, W., Thomas, D. D. & Louis, C. F. (1988). Site-specific derivatives of wheat germ calmodulin. Interactions with troponin and sarcoplasmic reticulum. *J. Biol. Chem.* **263**, 542–548.
34. Forar, F. L., Kincaid, R. L., Preston, R. L. & Hillers, J. K. (1982). Variation of inorganic phosphorus in blood plasma and milk of lactating cows. *J. Dairy Sci.* **65**, 760–763.
35. Wang, Z. X. (1995). An exact mathematical expression for describing competitive binding of two different ligands to a protein molecule. *FEBS Lett.* **360**, 111–114.
36. Cadene, M. & Chait, B. T. (2000). A robust, detergent-friendly method for mass spectrometric analysis of integral membrane proteins. *Anal. Chem.* **72**, 5655–5658.
37. Gabant, G. & Cadene, M. (2008). Mass spectrometry of full-length integral membrane proteins to define functionally relevant structural features. *Methods*, **46**, 54–61.
38. Bax, A. (1994). Multidimensional nuclear-magnetic-resonance methods for protein studies. *Curr. Opin. Struct. Biol.* **4**, 738–744.
39. Sklenar, V., Piotto, M., Leppik, R. & Saudek, V. (1993). Gradient-tailored water suppression for H-1–N-15 HSQC experiments optimized to retain full sensitivity. *J. Magn. Reson., Ser. A*, **102**, 241–245.
40. Delaglio, F., Grzesiek, S., Vuister, G. W., Zhu, G., Pfeifer, J. & Bax, A. (1995). NMRPipe—a multidimensional spectral processing system based on unix pipes. *J. Biomol. NMR*, **6**, 277–293.
41. Pervushin, K., Riek, R., Wider, G. & Wuthrich, K. (1997). Attenuated T-2 relaxation by mutual cancellation of dipole–dipole coupling and chemical shift anisotropy indicates an avenue to NMR structures of very large biological macromolecules in solution. *Proc. Natl Acad. Sci. USA*, **94**, 12366–12371.
42. Schonherr, R., Hehl, S., Terlau, H., Baumann, A. & Heinemann, S. H. (1999). Individual subunits contribute independently to slow gating of bovine EAG potassium channels. *J. Biol. Chem.* **274**, 5362–5369.

Supplementary Materials

Supplementary figure 1

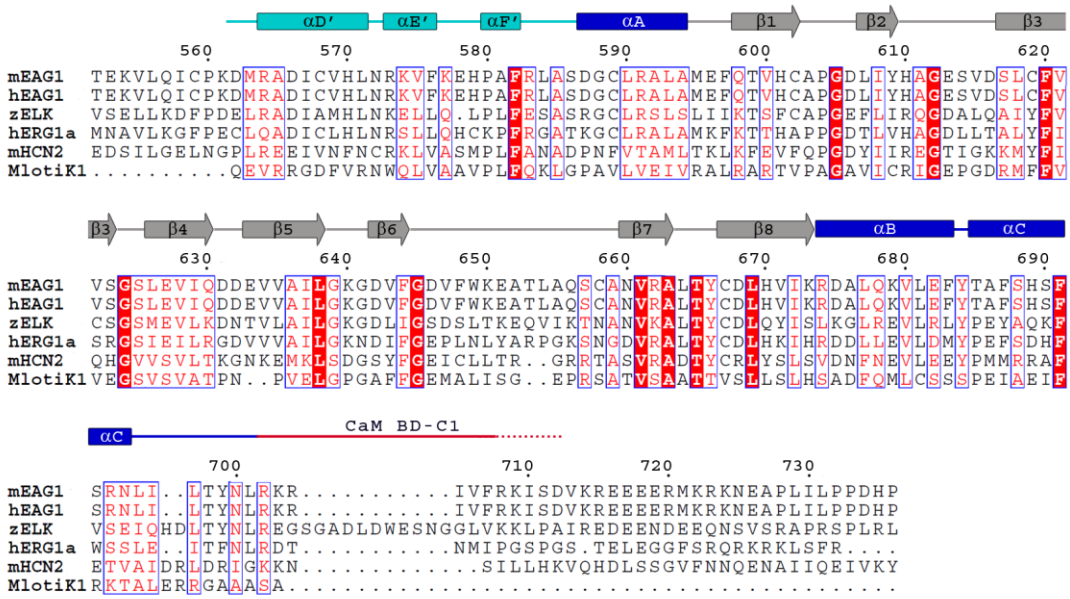

Supplementary figure 1 - Amino acid sequence alignment of C-terminal region of ion channels mouse EAG1 (mEAG1, NP_034730.1) and human EAG1 (hEAG1, NP_758872.1), zebra fish ELK (zELK, XP_001919436.2), human ERG1a (hERG1a, NP_000229.1), mouse HCN2 (mHCN2, NP_032252.1) and MlotiK1 (Q98GN8.1), graphically enhanced with Espript [1]. Above the alignment are the secondary structure elements of the CNB-homology domain. Bars represent α-helices and arrows β-strands. C-linker is colored in cyan, other helices in domain are in dark blue and β-roll in grey. Calmodulin BD-C1 binding site sequence is represented in red, where continuous line is the region present in the structure and dotted line the region absent from the structure. Amino acid numbering is of mouse EAG1.

Supplementary figure 2

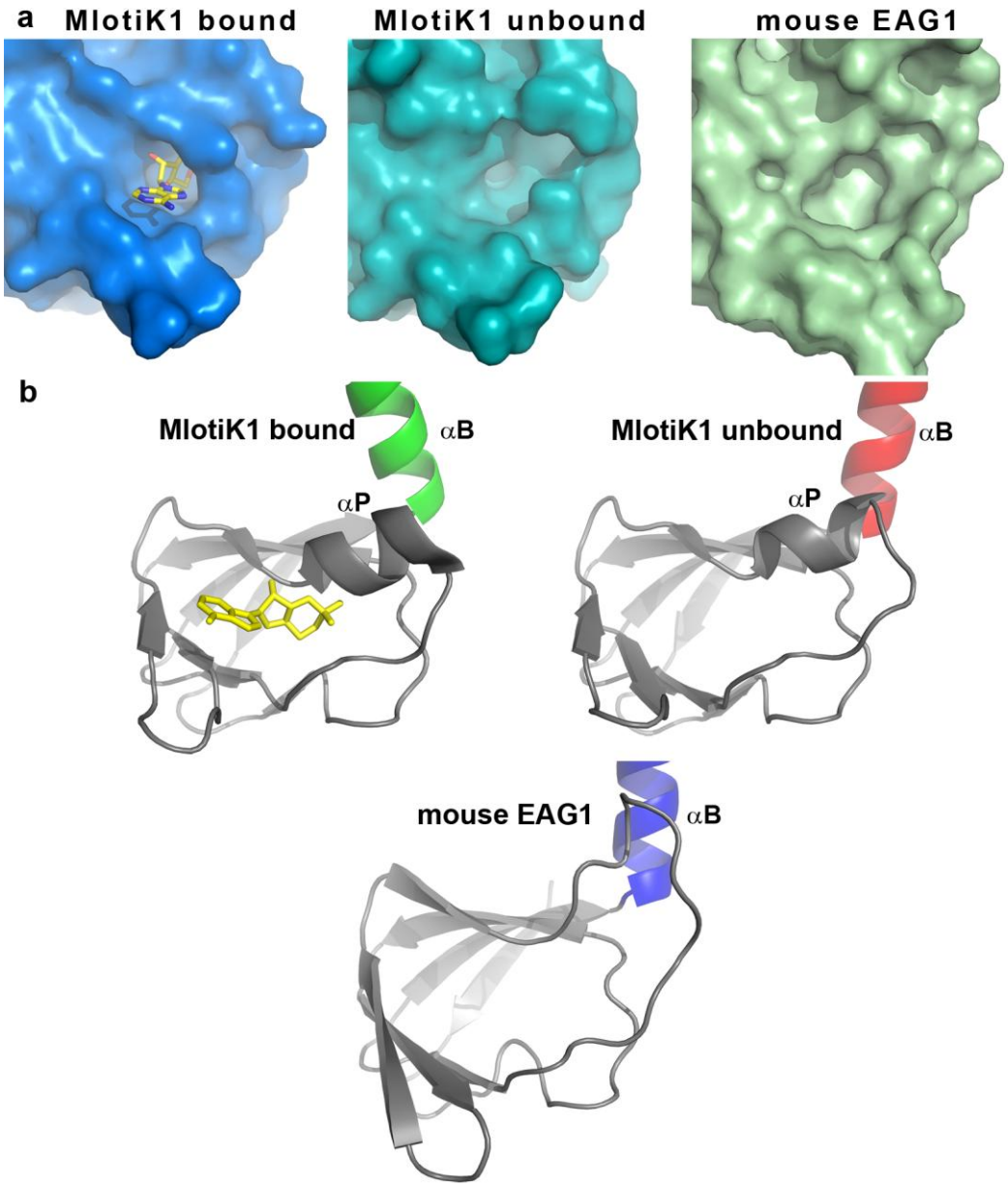

Supplementary figure 2 – Pockets in CNB-homology and CNB domains. **a)** Surface representations of binding pockets from: MlotiK1 bound structure (PDB code: 1VP6), with nucleotide in sticks; MlotiK1 unbound structure (PBD code: 1U12) and mouse EAG1 CNB-homology domain. **b)** Cartoon representations of binding pockets from MlotiK1 bound structure, MlotiK1 unbound structure and mouse EAG1 CNB-homology domain. αP helix in phosphate binding cassette of CNB domains is shown and labeled.

Supplementary Figure 3

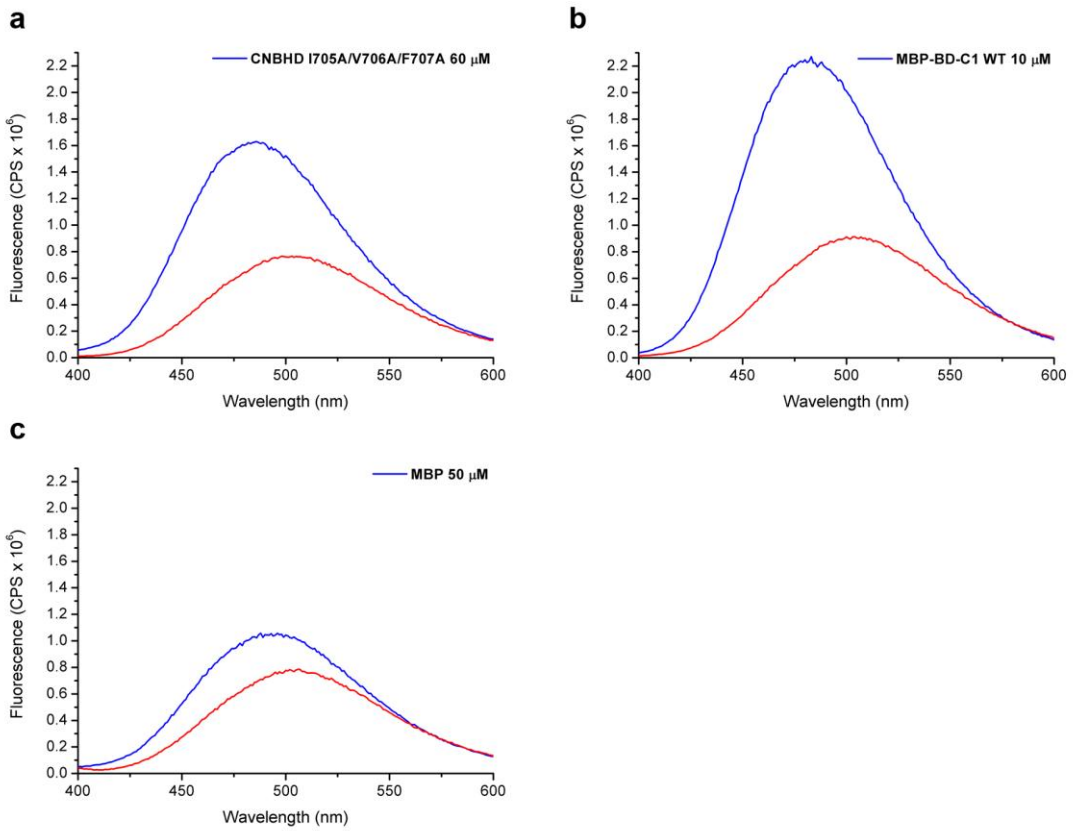

Supplementary Figure 3 – Emission fluorescence spectra from dansyl-calmodulin titrated with different protein constructs. Red curve is spectra for dansyl-calmodulin alone and blue curve for dansyl-calmodulin titrated with maximum concentration of protein, as indicated on each graph. **a)** Titration with CNB-homology domain triple BD-C1 site mutant up to 60 μM causes a shift of the emission maximum from 503 nm to 485 nm and an increase in intensity of more than 2-fold. **b)** Titration with fusion Maltose binding protein/BD-C1 site (up to 10 μM) causes a shift of the emission maximum from 504 nm to 482 nm and an increase in intensity of ~2.5-fold. **c)** Titration with Maltose binding protein (MBP) alone (up to 50 μM) causes a minor shift of the emission maximum from 505 nm to 493 nm and an increase in intensity of just ~1.4-fold. The very small blue shift and small increase in fluorescence are an indication of a very weak interaction, much weaker than the interaction measured in a) which has a K_D ~40 μM.

Supplementary Figure 4

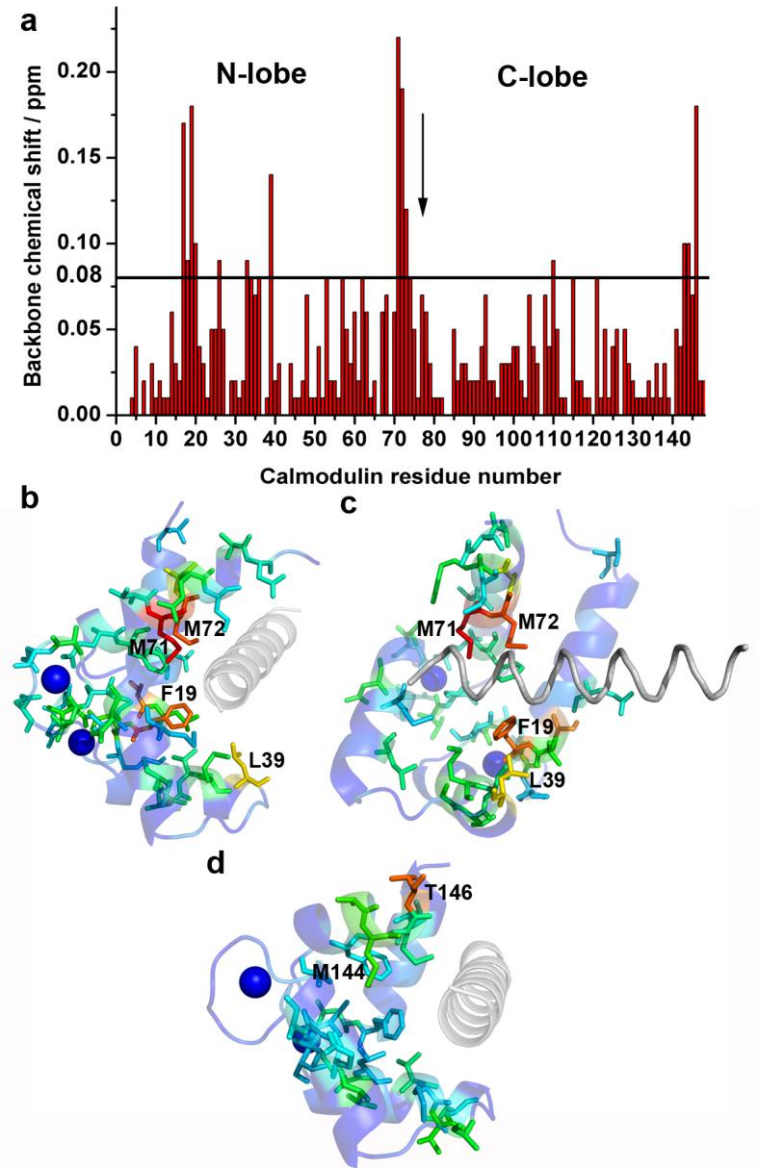

Supplementary Figure 4 – Mapping of interaction between CNB-homology domain and calmodulin. **a)** Plot of backbone residue chemical shift changes that occur upon binding to mEAG 552-724. Horizontal line marks cutoff of 0.08 ppm used for large changes. Arrow indicates the separation between the N- (to the left of arrow) and C-lobe (to the right of arrow). **b)** and **c)** Two views related by ~90°, of mapping of chemical shifts onto the structure of calmodulin N-lobe bound to a helical peptide (from PDB code 3OXQ). Calmodulin residues are rainbow colored (dark-blue to red) according to chemical shift difference (0.0-0.22ppm). No change is dark blue, large change is intense red. **d)** Structure of calmodulin C-lobe bound to helical peptide (from PDB code 3OXQ). Colored as in b).

Supplementary Figure 5

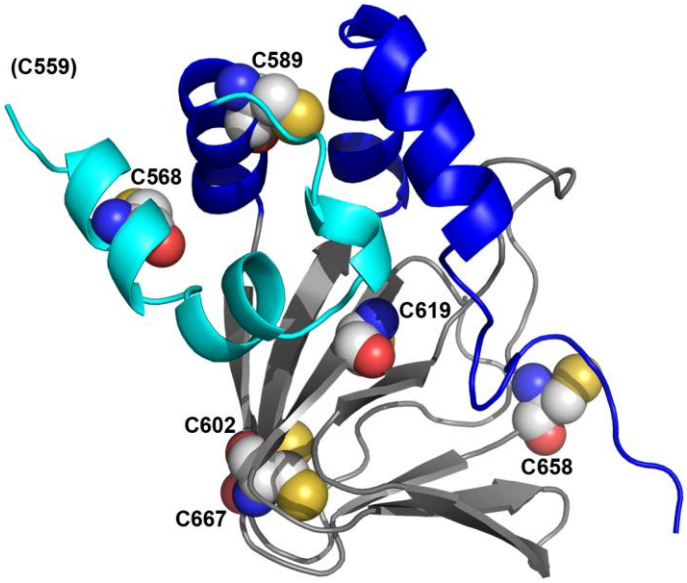

Supplementary Figure 5 – Cartoon representation of the structure of the CNB-homology domain from mEAG1 channel. Orientation and coloring is identical to Figure 1. Cysteine residues present in the structure are shown as spheres and are labeled. Number in parenthesis indicates the residue number of a cysteine present in the crystallized protein but not defined in the structure.

Supplementary Figure 6

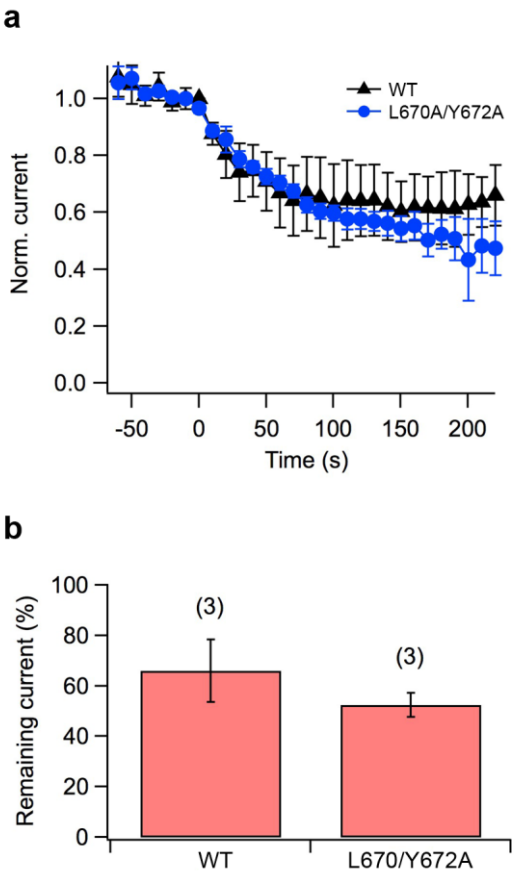

Supplementary Figure 6 – Ca^{2+}/calmodulin inhibition of human EAG1 channel. **a)** At time 0 excised patches expressing hEAG1 channel were exposed to a solution containing 500 nM calmodulin and 250 nM Ca^{2+}. Reduction in current elicited from wildtype channel (black triangles) and mutant L670A/Y672A (blue circles). **b)** Remaining current after exposure, average from 3 experiments.

1. Gouet, P., Courcelle, E., Stuart, D. I. & Metoz, F. (1999). ESPript: analysis of multiple sequence alignments in PostScript. *Bioinformatics* **15**, 305-8.

ERRATUM

"Structural and biochemical characterization of the interaction of calmodulin with the EAG1 potassium channel cytoplasmic regions"

Maria João Marques de Carvalho

- In page 50, in the last paragraph the following sentence should be "The ten-fold higher affinity relative to the short BDN is achieved through an increase in the entropy and decrease in the enthalpy of the system (Table 4)."

- In page 52, in the last paragraph the ΔH values lack the minus. They are -7.71 ± 0.08 kcal/mol for the CAP-PAS-BDN and -7.47 ± 0.18 kcal/mol for PAS-BDN. The last sentence should be substituted by "However, this is accompanied by a lower entropy change (smaller ΔS) which results in a lower affinity."

- In page 56, Table 4, the K_D for the Ca^{2+}-N-lobe/long BDN interaction is 8.9 ± 0.4 μM, not 4.5 ± 1.5 μM. This value is correct in the text.

- In page 77, Figure 45 should be substituted by the one below. The ITC titration examples depicted in Figure 45a and b were, by mistake, duplicates of Figure 30a and b. The interpretation of the data is not altered by this mistake.

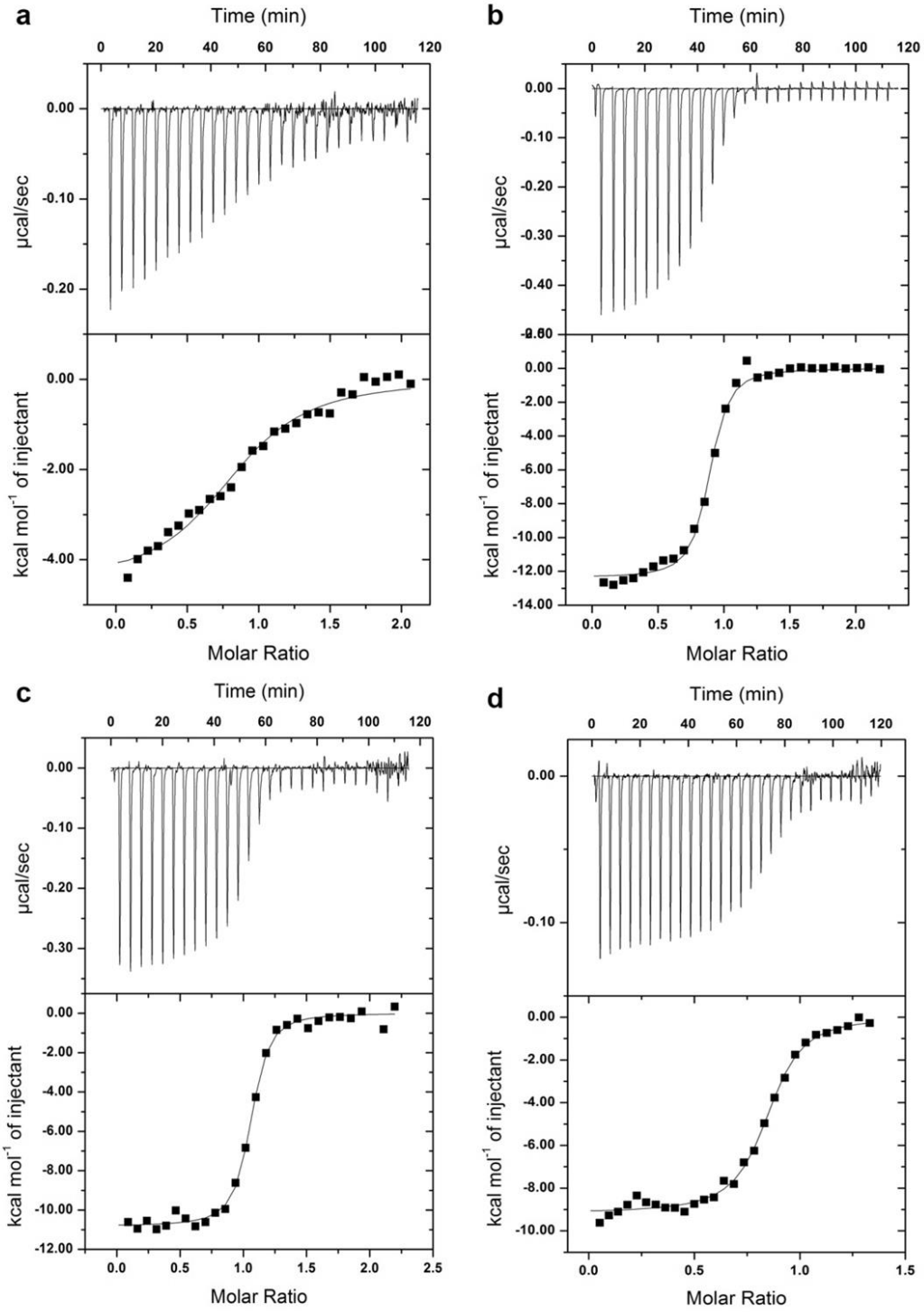

Figure 45 – a) ITC titration of 140 µM Ca^{2+}-N-lobe into 14 µM CNBhD-BDC1-BDC2. b) ITC titration of 100 µM Ca^{2+}-C-lobe into 10 µM CNBhD-BDC1-BDC2. c) ITC titration of 100 µM Ca^{2+}-CaM EF12 mutant into 100 µM CNBhD-BDC1-BDC2 (direct). d) ITC titration of 40 µM CNBhD-BDC1-BDC2 into 6 µM Ca^{2+}-CaM EF12 mutant (reverse).